

# **Context-Aware Dynamic Power Management for Self-Powered Body Sensor Networks**

---

A Dissertation

Presented to

the faculty of the School of Engineering and Applied Science

University of Virginia

---

in partial fulfillment  
of the requirements for the degree

Doctor of Philosophy

by

Dawei Fan

August 2018

# APPROVAL SHEET

This Dissertation  
is submitted in partial fulfillment of the requirements  
for the degree of  
Doctor of Philosophy

Author Signature: \_\_\_\_\_

This Dissertation has been read and approved by the examining committee:

Advisor: John C. Lach

Committee Member: Benton H. Calhoun

Committee Member: John C. Lach

Committee Member: Haiying Shen

Committee Member: Nicola Bezzo

Committee Member: Brad Campbell

Accepted for the School of Engineering and Applied Science:



Craig H. Benson, School of Engineering and Applied Science

August 2018

This page intentionally left blank

## Acknowledgment

First of all, I'd like to thank my advisor Prof. Lach who gave me the valuable opportunity to start my Ph.D. adventure. I appreciate working with Prof. Lach and joining the INERTIA group. During these years, I'm trained to be an independent researcher and learned much from him. He provided tremendous support for my research, helped me to find possible research directions from the projects and to organize and develop the research ideas. All of these are critical for me to complete the doctoral research and this dissertation.

I'd like to thank my committee members, Prof. Calhoun, Prof. Whitehouse, Prof. Shen, Prof Bezzo, and Prof Campbell who spent the time to help me to shape the research ideas and challenged me to think in depth about the motivation and impact of my research.

I'd like to thank Prof. Gong who gave me enormous help in my life and research. When he was a research scientist in our group, we worked closely on research projects such as the ASSIST project, the agitation project, and the ozone project. He also helped me to develop the idea of energy harvesting profiling and modeling. More importantly, I learned from him about general research skills like how to read papers, develop ideas, and plan publications.

I'd like to thank Prof. Weller who helped me with the optimization problem which is the key part of my dissertation. We discussed the optimal solution to the problem and the idea of using energy prediction to develop online scheduling algorithms. I enrolled in two courses including the probabilities and stochastic process and the advanced signal processing from him, which helped me a lot with my research and dissertation.

I also learned much from my group mates and really enjoyed working with them. Our INERTIA team is excellent and I love it. I'd like to thank them for the help provided in my research and dissertation. I'd like to give special thanks to Luis Lopez Ruiz who worked with me on most of

the projects since 2014. He is an expert on the hardware design and we worked together on the EHDC and SCDPM platforms. The hardware design and soldering of EHDC and part of the SCDPM are done by him. Without him, we cannot implement the energy profiling idea and validate my context-aware dynamic power management framework.

I'd like to thank Henry Bishop and Peng Wang who collaborated with me on the LITE project and they did a primary part of the project. The LITE project demonstrates the usage and impact of the EHDC platform in the IoT area.

Certainly, I'd like to thank my parents and my fiancée for their support and love for me to complete the Ph.D. journey.

Finally, I'd like to thank the funding from ASSIST project which supports my Ph.D. research. The funding is from the National Science Foundation under grant numbers IIS-1231712 and EEC-1160483.

## Abstract

Body sensor networks (BSNs) have shown significant potential in health applications by empowering researchers, scientists, doctors, caregivers, and patients to explore correlations between human-related sensor data and human health through continuous, vigilant, remote, and non-invasive data collection. To enable continuous vigilant monitoring for long-term logging of sensor data without human intervention, the operation time of BSNs is a significant concern. Harvesting energy from the body and the ambient environment has become a promising solution for realizing self-powered sensor systems capable of quasi-perpetual operation. However, the discontinuous and dynamic characteristics of energy harvesting in real-world scenarios – and their implications for the design and operation of self-powered sensor systems – are not yet well studied.

Conventional characterization of energy harvesters is done in a laboratory environment, without much consideration for such real-world dynamics. In order to better understand the nature of the energy sources like solar and thermoelectric and how the human behavior affects the energy harvesting, we designed a custom Energy Harvesting and Data Collection (EHDC) platform to explore energy harvesting dynamics by longtime profiling in the real world.

Since the energy sources are uncontrollable but often predictable, we proposed a context-aware hybrid model for the multimodal indoor and outdoor energy harvesting prediction. Here we term *context* to refer to energy harvesting related factors including environmental parameters like light intensity, temperature, weather forecast; and human behavior like motion, schedule, and location. By leveraging the knowledge of the current context and near future, the system could predict harvested energy more accurately and thus improve the efficiency of power consumption.

The core of this work is the design of the context-aware dynamic power management framework for self-powered body sensor networks. With the understanding of energy harvesting

dynamics, the framework is proposed to efficiently use the harvested power to optimize the data quality according to the environmental and behavioral context. The power management in an energy harvesting system is formalized as a convex optimization problem, and the optimal solution is derived. Online scheduling in the real world with energy prediction is discussed. A case study of Atrial Fibrillation detection is analyzed to demonstrate the application-specific utility/cost function which could better represent the demand of the application. Such application-specific cost analysis outperforms the methodologies that solely from the perspective of digital signal processing, or generally assume a linear cost function in related work which would be too simplified.

We validate this framework by designing a custom Self-powered and Context-aware Dynamic Power Management (SCDPM) platform. The platform is capable of vigilant health monitoring with ECG and motion data. It also collects environmental data which help to understand the context and make dynamic power management. The SCDPM is an ultralow power platform which performs better than state-of-the-art health monitoring platforms regarding system power consumption and the dynamic power management and adaptive sensing capabilities.

Overall, this work explores the energy harvesting dynamics to improve the design of self-power sensor systems and the proposed context-aware dynamic power management framework improves the self-powered BSN performance and operation time by taking advantage of context information.

## Contents

<b>LIST OF FIGURES .....</b>	<b>X</b>
<b>LIST OF TABLES .....</b>	<b>XVI</b>
<b>1 INTRODUCTION.....</b>	<b>1</b>
<b>1.1 Dissertation Outline .....</b>	<b>4</b>
<b>1.2 Dissertation Contributions .....</b>	<b>7</b>
<b>2 MOTIVATING SELF-POWERED BODY SENSOR NETWORKS .....</b>	<b>9</b>
<b>2.1 Body Sensor Networks.....</b>	<b>9</b>
<b>2.2 Energy Harvesting and Sources .....</b>	<b>11</b>
<b>2.3 Summary.....</b>	<b>12</b>
<b>3 ENERGY HARVESTING PROFILING .....</b>	<b>13</b>
<b>3.1 An Overview of Energy Harvesting Systems.....</b>	<b>14</b>
<b>3.2 Related Work .....</b>	<b>15</b>
<b>3.3 EHDC: Energy Harvesting and Data Collection Platform .....</b>	<b>16</b>
<b>3.4 Experiments and Results .....</b>	<b>20</b>
<b>3.5 Lighting Environment Simulation with EHDC.....</b>	<b>23</b>
3.5.1 Hardware Platform .....	24
3.5.2 Calibration of the Lighting System .....	26
3.5.3 Light Source Emulation and Mapping Functions .....	28
3.5.4 Simulations of Time-series Profiles .....	31
<b>3.6 Summary.....</b>	<b>33</b>
<b>4 ENERGY HARVESTING PREDICTION.....</b>	<b>34</b>
<b>4.1 Related Work .....</b>	<b>35</b>
4.1.1 Exponential Weighted Moving Average Based Models .....	36
4.1.2 Profile-Based Models .....	38
4.1.3 Empirical Models .....	38
4.1.4 Weather Forecast Based Models .....	39
4.1.5 Prediction Horizon.....	40

4.1.6	Hybrid Indoor and Outdoor Prediction For BSN .....	41
<b>4.2</b>	<b>A Hybrid Context-Aware Profile Based Model .....</b>	<b>42</b>
4.2.1	The Scope of Context .....	42
4.2.2	Profiles.....	43
4.2.3	Context-Aware Hybrid Models .....	44
<b>4.3</b>	<b>Summary.....</b>	<b>45</b>
<b>5</b>	<b>DYNAMIC POWER MANAGEMENT OPTIMIZATION .....</b>	<b>47</b>
<b>5.1</b>	<b>Context-Aware Dynamic Power Management Framework.....</b>	<b>49</b>
<b>5.2</b>	<b>A DPM Scheduling Model for Energy Harvesting Sensor System.....</b>	<b>51</b>
<b>5.3</b>	<b>Optimal Solution .....</b>	<b>53</b>
<b>5.4</b>	<b>DPM Model with Battery Capacity Limit .....</b>	<b>59</b>
<b>5.5</b>	<b>Online Scheduling with Energy Harvesting Prediction.....</b>	<b>67</b>
<b>5.6</b>	<b>A Case Study: Vigilant Atrial Fibrillation Monitoring .....</b>	<b>70</b>
5.6.1	Vigilant Monitoring and Atrial Fibrillation.....	70
5.6.2	Application-Driven Metrics for Vigilant Monitoring.....	72
5.6.3	Experiments and Results .....	74
5.6.4	Application-Specific Cost Function .....	79
<b>5.7</b>	<b>Summary.....</b>	<b>81</b>
<b>6</b>	<b>SELF-POWERED CONTEXT-AWARE DYNAMIC POWER MANAGEMENT PLATFORM.....</b>	<b>83</b>
<b>6.1</b>	<b>Hardware System Design .....</b>	<b>84</b>
6.1.1	Control and Data Transmission .....	86
6.1.2	Energy Harvesting .....	87
6.1.3	Sensing .....	91
6.1.4	Power Management .....	93
6.1.5	System Integration.....	94
<b>6.2</b>	<b>Embedded Software Development for SoC .....</b>	<b>97</b>
6.2.1	Software Platform Overview .....	98
6.2.2	Custom BLE Services Definition .....	99
6.2.3	Device Driver .....	100

6.2.4	Data Schemes for Use Cases .....	100
<b>6.3</b>	<b>Android Application Development.....</b>	<b>103</b>
6.3.1	User Interface .....	104
6.3.2	Communication .....	105
6.3.3	Context Manager .....	105
6.3.4	Energy Harvesting Prediction and DPM Scheduling .....	108
6.3.5	Local and Cloud Data Storage.....	108
<b>6.4</b>	<b>Power Consumption Modeling .....</b>	<b>109</b>
6.4.1	Current Consumption Profiling .....	110
6.4.2	Power Consumption Modeling .....	113
<b>6.5</b>	<b>Summary.....</b>	<b>116</b>
<b>7</b>	<b>VALIDATION OF CONTEXT-AWARE DYNAMIC POWER MANAGEMENT ON SCDPM .....</b>	<b>119</b>
<b>7.1</b>	<b>Data Collection Using SCDPM.....</b>	<b>119</b>
7.1.1	Profiles in Various Weather Conditions .....	121
7.1.2	Profiles in Indoor Environment .....	123
<b>7.2</b>	<b>ECG and Motion Details .....</b>	<b>125</b>
7.2.1	ECG Profile .....	125
7.2.2	Motion Profile .....	127
<b>7.3</b>	<b>Energy Prediction .....</b>	<b>128</b>
7.3.1	Weather Parameter .....	129
7.3.2	Location Profiles .....	130
7.3.3	Experiment and Results .....	131
<b>7.4</b>	<b>Dynamic Power Management on SCDPM.....</b>	<b>133</b>
7.4.1	The Offline Algorithm.....	133
7.4.2	The Online Algorithm .....	135
<b>7.5</b>	<b>Summary.....</b>	<b>137</b>
<b>8</b>	<b>CLOSING REMARKS.....</b>	<b>138</b>
<b>8.1</b>	<b>Contributions and Future Work .....</b>	<b>138</b>
<b>8.2</b>	<b>Publications .....</b>	<b>140</b>

<b>APPENDIX A. OTHER COMPLETED RESEARCH PROJECTS.....</b>	<b>142</b>
<b>A.1 Data Aggregator Design for Custom Ultra-Low Power Radio .....</b>	<b>142</b>
<b>A.2 Wearable Ozone Sensors Calibration in Dynamic Environments.....</b>	<b>143</b>
<b>A.3 Eating Gestures Detection by Tracking Finger Motion .....</b>	<b>143</b>
<b>A.4 Nighttime Agitation and Incontinence Monitoring.....</b>	<b>144</b>
<b>BIBLIOGRAPHY .....</b>	<b>145</b>

# List of Figures

Figure 2.1 Self-powered body sensor networks. The sensor nodes harvest energy from the environment and the human body, collect sensor data, and transmit data to a phone. The phone uploads the data to a cloud service for data storage and processing.....	10
Figure 3.1 Diagram of a typical energy harvesting system which consists of four modules: energy harvesting, energy conversion, energy storage, and energy consumption.....	14
Figure 3.2 The first version platform which includes standalone components on breadboards connecting to Shimmer nodes.....	18
Figure 3.3 Block diagram of the EHDC platform and the interface with the Raspberry Pi 0. ....	19
Figure 3.4 Software architecture for EHDC platform. ....	19
Figure 3.5 From left to right, the full EHDC platform for multi-source energy harvesting and the platform deployed on a human subject. ....	20
Figure 3.6 Energy harvesting profiles for four sessions. ....	23
Figure 3.7 System block diagram of the LITE Platform consisting of the EHDC board's hardware and software components, the physical LITE apparatus, PV cell (DUT), and lux sensors. ....	25
Figure 3.8 LITE platform implementation based on the block diagram.....	26
Figure 3.9 The relationship between light intensity and resistance control bits and gain. ....	27
Figure 3.10 Relative error between input (ideal) lux and output (generated) lux of the apparatus. The calibration equation turns an input lux stream into control bits, which in turn creates real light that should match in value to the input. ....	28

Figure 3.11 Lux-power curves are showing the relationships between light intensity and maximum power obtained from the data of four typical light sources. The LED is used to emulate the other four types of light sources and shown by the dashed lines and diamond symbols. ....	30
Figure 3.12 Time-series light profile simulation. The yellow dashed line represents the calculated power-equivalent LED lux sequence, and the orange line is the measured lux values which match the input well.....	32
Figure 3.13 Time-series power profile. The emulated curve matches the original power profile well except one point around the 7th minute.....	32
Figure 5.1 Abstract diagram of system-level dynamic power management.....	49
Figure 5.2 The workflow for the proposed context-aware dynamic power management framework. The sensor system communicates with a phone which runs the power management algorithm..	50
Figure 5.3 Simulation of DPM strategies on an energy profile. The cost of the proposed algorithm (offline solution) and the greedy algorithm is 1436.4, 1846.9 respectively. The stoplight algorithm encounters powering down. ....	59
Figure 5.4 Offline simulation of DPM strategies on an energy profile according to different capacity $C$ values in mJ.....	65
Figure 5.5 The cost of the scheduling of each capacity $C$ . The cost decreases along with the increase of the capacity $C$ until $C$ is large enough.....	65
Figure 5.6 The remained energy on the supercapacitor regarding different $C$ values (mJ).....	66
Figure 5.7 The cost versus the capacity $C$ from 0 to 5. The cost decreases as $C$ increases from 0 to 4.38mJ and remains the same after that. ....	66
Figure 5.8 Short-term and long-term prediction for online scheduling.....	67

Figure 5.9 Online energy consumption simulation in each prediction method comparing to the offline solution.....	69
Figure 5.10 The remained energy on the supercapacitor regarding different prediction methods.....	69
Figure 5.11 Compare of the cost from the greedy algorithm, offline, online with three different prediction accuracies. The online algorithm performs better the than greedy algorithm but worse than the optimal offline algorithm. The better prediction model has lower cost.....	70
Figure 5.12 ECG waveforms and detected QRS complexes in red circles with different sampling rates at 250Hz, 200Hz, 100Hz, 50Hz, 20Hz, and 10Hz. With the decrease of the sampling rate, the ECG signal becomes distorted, but the QRS complex detection works well until a minimum sampling rate of 20Hz.....	73
Figure 5.13 The receiver operating characteristic (ROC) curves of AFib detection under nine sampling rates. The curve is moving inward as the sampling rate decreases.....	75
Figure 5.14 The ROC area (AUC) and the maximum $F_2$ score of AFib detection under nine sampling rates. The value in general increases with the sampling rate.....	76
Figure 5.15 The receiver operating characteristic (ROC) curves of AFib detection under seven quantization depths. The curve is moving inward as the quantization depth decreases.....	77
Figure 5.16 The ROC area (AUC) and the maximum $F_2$ score of AFib detection under seven quantization depth. The value in general increases with the quantization depth.....	77
Figure 5.17 The ROC area (AUC) versus quantization depth and sampling rate.....	78
Figure 5.18 Design space considering the sampling rate and quantization depth. Power consumption is calculated using a model developed in Section 6.4 of our SCDPM platform. The	

red line is part of the convex hull of all the points, and it represents the optimal design decisions at specific power consumption level.....	79
Figure 5.19 Curve fitting of the cost function, which is power versus AUC. ....	80
Figure 6.1 Block diagram of the SCDPM platform including a main board, a sensing board, and an energy harvesting board. ....	85
Figure 6.2 Solar panel characterization. ....	87
Figure 6.3 TEG array. Hot side in the left picture attaching to people’s skin, and cold side with a heat sink to dissipate heat into the ambient air. ....	89
Figure 6.4 TEG characterization under a room temperature of 22°C.....	90
Figure 6.5 The main board.....	94
Figure 6.6 The energy harvesting board. ....	95
Figure 6.7 The sensing board.....	95
Figure 6.8 Physical integration with an armband. ....	96
Figure 6.9 Wearable system on the body. (ECG electrodes locations are not accurate) .....	97
Figure 6.10 Diagram of the DA14580 software architecture. ....	98
Figure 6.11 Screenshot of the Android application running. The user could configure the system parameters including data schemes, sampling rate, connection parameters, and power management option. The sensor data of ECG, acceleration, the voltage on the supercapacitor, temperature and light intensity are displayed in real-time.....	105
Figure 6.12 An example of the weather forecast data in JSON format. ....	106
Figure 6.13 Screenshot of the cloud application. The sensor data of ECG, acceleration, the voltage on the supercapacitor, temperature and light intensity are displayed in real-time. The viewer could change the time range, refresh rate, and zoom in/out. ....	109

Figure 6.14 Current consumption profiling using SmartSnippet. The blue curve shows the active mode without BLE transmission and the orange curve with BLE transmission. ....	111
Figure 6.15 Comparison of current consumption profiling by using SmartSnippet and an oscilloscope.....	112
Figure 6.16 Workload change during normal operations. There are roughly three levels of power consumption: sleep, active, and data transmission. ....	112
Figure 6.17 Workload change during operation. The curve was plotted using data collected from an oscilloscope.....	113
Figure 6.18 Power Consumption versus sampling rate. ....	116
Figure 7.1 A profile collected on a sunny day.....	121
Figure 7.2 A profile collected on a cloudy day.....	122
Figure 7.3 A profile collected on a rainy day. ....	123
Figure 7.4 A profile collected at home. ....	124
Figure 7.5 Supercapacitor voltage drop along time at different sampling rates. ....	124
Figure 7.6 10 seconds ECG signal at different sampling rates. ....	125
Figure 7.7 ECG waveform while running.....	126
Figure 7.8 Heart rate (BPM) before, during, and after running calculated from the collected ECG signal. ....	126
Figure 7.9 Acceleration during running.....	127
Figure 7.10 Acceleration during pulldown exercise. ....	128
Figure 7.11 Acceleration during shoulder press exercise. ....	128
Figure 7.12 Average power profile in the daytime. ....	129
Figure 7.13 Long-term prediction of light intensity using context information. ....	132

Figure 7.14 Short-term prediction of light intensity using exponential smoothing.....	133
Figure 7.15 Power management with different policies for the rainy day.....	134
Figure 7.16 Power management with different policies for the sunny day. ....	134
Figure 7.17 Power management with different policies for the cloudy day.....	135
Figure 7.18 The profile and dynamic power management. ....	137

# List of Tables

Table 3.1 Mapping RMSE and percentage error. ....	30
Table 4.1 Prediction horizon of different models. ....	41
Table 6.1 Skin temperature of ten different body locations.....	90
Table 6.2 Sensing modalities, IC, the interface with DA14580, and power consumption. The sampling rate is 100Hz.....	92
Table 6.3 Operation voltage range of the main components in the system. ....	93
Table 6.4 Custom service definition. ....	99
Table 6.5 Command pattern.....	100
Table 6.6 Sampling sequence of scheme 0. ....	101
Table 6.7 Sampling sequence of scheme 1. ....	102
Table 6.8 Sampling sequence of scheme 2. ....	102
Table 6.9 Sampling sequence of scheme 5. ....	103
Table 6.10 An overview of the Android application ....	104
Table 6.11 A weather forecast result example.....	107
Table 6.12 Power consumption of each component. ....	110
Table 6.13 Parameters measured or assigned. ....	115
Table 6.14 Comparison between EHDC and SCDPM. ....	116
Table 6.15 Comparison of low power, wearable, health monitoring systems including ECG... ..	118
Table 7.1 An overview of collected profiles.....	120
Table 7.2 Power consumption of each component. ....	130

Table 7.3 Indoor location profiles.....	131
Table 7.4 A schedule and weather forecast of a typical day.....	131
Table 7.5 DPM performance comparison over three profiles.....	135

# 1 Introduction

Body sensor networks (BSNs) have shown significance in healthcare domain by providing enormous help for researchers, scientists, doctors, caregivers, and patients to explore the implicit correlations between human-related sensor data and human health [1]–[4]. The correlations have been demonstrated to be beneficial for preventing, diagnosing, staging and tracking chronic diseases such as Alzheimer’s disease, dementia, and heart disease[5]–[11]. Therefore, BSN technology has the great potential to improve the quality of publics’ lives and to reduce medical costs.

To enable continuous monitoring for long-term logging of clinical data, the operation time of BSN is a significant concern [1]–[5]. Considering the wearing comfortability for human subjects, the form factors and weight of BSN nodes and the supporting batteries are usually small. Since in general the energy storage of a battery is related to its form size, tiny batteries provide insufficient amounts of energy to support long operating time of BSN nodes. The burden of frequent recharge or replacement of batteries for BSN impedes widespread adoption of BSN in clinical use[1][4].

The objective of this work is to solve these energy challenges encountered in BSN area which are critical for continuous health monitoring. Specifically, to address the research questions of:

1. How can we better understand the dynamics of available energy for BSN systems in the real world to enable vigilant health monitoring with self-powered BSN?

2. How can we optimize the power management in an energy harvesting system to achieve the optimal application-specific data quality?

**Energy profiling.** A critical challenge encountered when designing self-powered energy harvesting BSN applications is the discontinuity nature of energy sources[12]–[14]. The energy sources including solar and thermal are all intermittent and discontinuous. The dynamic characteristics of energy harvesting in real-world scenarios and their implications on the design of self-powered BSN are of profound importance, while not well studied yet. Conventional ways usually characterize energy harvesters or make simulations in the lab[12], [13], [15]–[26], without much consideration in real-world dynamics. An approach worth noting is that in solar energy harvesting area, researchers create profiles for months or even years to explore the relationship between solar energy harvesting and environmental dynamics[19]. However, in BSN area, besides environmental factors, human behavior has a significant influence on energy harvesting and should be taken into consideration. In this work, energy profiling and modeling for BSN regarding real-world environmental dynamics and human activities are discussed in Section 3 to address the first questions. An Energy Harvesting and Data Collection (EHDC) platform is designed to harvest solar and thermoelectric energy and collect data on environmental and human activities. With the EHDC platform, energy profiles are created to explore the energy availability and to understand the energy dynamics in the real world.

**A context-aware dynamic power management framework for prediction and power management.** With the understanding of the dynamics of energy harvesting using the proposed approach, the power management in an energy harvesting system is explored. In order to answer the second question, a novel context-aware dynamic power management (DPM) framework for an energy harvesting system is proposed. Here the context includes environmental factors like light

intensity, temperature; and human behavior like acceleration data, schedule, location, indoor/outdoor. With the knowledge of the current context and prediction of the near future, a BSN node could achieve a better performance of power management. Dynamic strategies could be utilized to optimize the data quality/fidelity which includes sensor sampling rate and precision, data delay, and data loss (power down or connection loss) based on the context. In Section 5, firstly, the DPM framework is presented and discussed. Second, the scheduling model regarding energy harvesting and consumption is proposed, and an optimal offline solution algorithm and the online version based on prediction are derived. Finally, a case study of Atrial Fibrillation (AFib) detection is discussed.

**Self-powered Context-aware Dynamic Power Management Platform (SC-DPM).** We validate the proposed framework by designing a custom Self-powered and Context-aware Dynamic Power Management (SCDPM) platform. The platform is capable of vigilant health monitoring with ECG and motion data. It also collects environmental data which help to understand the context and make dynamic power management. The SCDPM is an ultralow power platform which performs better than state-of-the-art health monitoring platforms regarding system power consumption and the dynamic power management and adaptive sensing capabilities. The details of platform design and energy consumption model are presented in Section 6.

The *thesis* of this dissertation is that energy profiling and context-aware dynamic power management can improve the performance of self-powered BSNs. Energy profiling regarding environmental and human factors could help provide a better understanding of energy harvesting dynamics for BSNs in the real-world conditions. Context-aware dynamic power management considering both energy harvesting dynamics and system power consumption could maximize application-specific data quality while preserving continuous self-powered operation.

## 1.1 Dissertation Outline

This dissertation consists of 8 Chapters which are organized as the follows. Chapter 2 introduces the background of this work including the emergence of Body Sensor Networks (BSNs) in health applications which empowers researchers, scientists, and doctors to explore correlations between human-related sensor data and human health through remote continuous data collection. To enable such long-term continuous monitoring, the operating time of body sensor networks is a significant concern and energy harvesting from ambient environment is a promising solution. The commonly used energy sources especially solar and thermoelectric sources are discussed.

Chapter 3 describes the design of our custom Energy Harvesting and Data Collection (EHDC) platform to harvest solar and thermoelectric energy and collect data on environmental and human activities. In 2015, we were interested in the energy harvesting dynamics in BSN in the real world and generated the idea of energy harvesting profiling. At first, we used the commercial Shimmer sensor nodes and related custom circuitry for the research, however, it had many limitations. Therefore, we designed the custom EHDC which better fits our demand. The platform was utilized to explore the energy harvesting dynamics in the real world as shown in Section 3.3 and Section 3.4. The EHDC platform could be considered as the beginning of this doctoral research. After the dissertation proposal, we generated the idea of utilizing the EHDC platform to create an apparatus to simulate and replay light profiles for validation of the solar-powered systems. This collaborative project is presented in Section 3.5.

We discuss the energy harvesting prediction in Chapter 4. Since the unique characteristics of energy harvesting for on body deployed BSNs that we observed from the real-world profiling, we found the previous work for energy prediction cannot perform well in BSN area. Therefore, inspired by the features of some prediction methodologies, we proposed a context-aware hybrid

model for both indoor and outdoor BSN energy harvesting prediction by leveraging as much as the context information for predicting both the environmental and human behavior. We term context to cover all information from the sensor system or the smartphone which is related to energy harvesting including environmental variables, online information, and human behaviors.

Chapter 5 is the most critical section to describe the primary contribution of the dissertation. A context-aware dynamic power management framework is proposed to optimize the data quality in an energy harvesting BSN. The power management is discussed from the perspective of nonlinear convex optimization. In Section 5.2, the optimization model of the power management in the energy harvesting system is formally constructed, and the optimal offline solution is derived in Section 5.3. We further consider the constraint of the supercapacitor capacity limit in Section 5.4 and add the constraints to the problem to derive the updated optimal solution. The offline solution is the theoretically optimal as strictly proved, however, in the real world, we cannot have the Oracle information of future harvested energy. Therefore, we leverage the energy prediction methodology to approximate the future energy harvesting behavior, and we prove that higher prediction accuracy brings better power management performance which could be close to the optimal offline solution. Finally, we study the Atrial Fibrillation (AFib) as a case study in Section 5.6 to explore the application-specific relationship between the power consumption and utility/cost, and we prove that in this application the proposed DPM algorithm works well. Besides, we demonstrate that in this scenario and many other applications, the utility/cost function is nonlinear and cannot be well modeled as a linear optimization problem as shown in many previous works. Simulations are executed to help demonstrate the validity of the proposed algorithms.

In Chapter 6 we presented another custom system, the Self-powered Context-aware Dynamic Power Management Platform (SCDPM). This platform is designed and has been evolved from late

2016 to 2018. Much effort was put into the hardware design, software design, and system test at different levels. The SCDPM is an ultralow power multimodal context-aware self-powered wearable sensor system for real-world vigilant cardiac and activity monitoring that achieves a positive energy balance from both solar and thermoelectric energy sources. The platform collects ECG, acceleration, and environmental parameters including light intensity and ambient air temperature. It wirelessly streams data to a smartphone through Bluetooth Low Energy (BLE) for data visualization and processing. Besides, the sensor data is interfaced to specific cloud service in real time for data storage, remote data access, and caregiver/clinician/researcher notification. The SCDPM is used to validate the proposed energy prediction and DPM algorithms. It receives commands from the phone in real-time for power management according to the DPM scheduling algorithm to dynamically adjust its operating parameters. The hardware system design is described in Section 6.1, and the software design including Android programming on the phone side and embedded C programming on the sensor node side is described in Section 6.2 and Section 6.3. In Section 6.4, the power consumption model of SCDPM is discussed. We compared SCDPM to our EHDC platform and other state-of-the-art platforms in Section 6.5.

Chapter 7 presents the results related to the SCDPM platform, prediction, and the DPM scheduling. The SCDPM was deployed in the real world and collected more than 50 hours of data from 12 sessions. Profiles from typical weather conditions including sunny, cloudy, and rainy were collected to understand how weather conditions affect the energy harvesting. The ECG and motion data are presented and analyzed to demonstrate the effectiveness of health monitoring. Finally, we tested the adaptive sampling and dynamic power management using a profile.

Chapter 8 finalizes the dissertation with the discussion of the contribution of this work and future work.

## 1.2 Dissertation Contributions

The primary impact of this work is the context-aware dynamic power management framework to leverage context information for energy harvesting prediction and to make dynamic power management to achieve the optimal data quality. The framework has a broader impact in areas of general sensor networks, Internet of Things (IoT), and Cyber-Physical Systems (CPS) to achieve better power management performance. The energy profiling work could equip BSN designers with a more in-depth understanding of energy dynamics in the real world to work towards self-powered BSN.

To be specific, the direct contributions of this dissertation include:

1. Energy profiling for BSN in the real world. The idea of understanding energy harvesting dynamics by profiling it in the real world in addition to the in-lab characterization is innovative at the time of publishing the papers. The Energy Harvesting and Data Collection (EHDC) platform for energy harvesting profiling and modeling was one of the first platforms that implement this idea. The EHDC platform itself could be considered a contribution as well, and the LITE project discussed in Section 3.5 is actually an example usage of EHDC. The software code for the EHDC is open sourced on [27] for people to use.
2. A context-aware hybrid energy prediction model for both indoor and outdoor environment energy harvesting. This is more like a framework than a model, and we use calendar events and weather forecast as the context information for the prediction. The scope of context and the way to utilize the context information could be extended.
3. A context-aware Dynamic Power Management (DPM) framework for energy harvesting BSNs. A formal model and analysis of the scheduling optimization problem in an energy

harvesting system are constructed, and the optimal solution is derived. A case study of AFib detection is intensely studied to prove the validity of the framework.

4. A Self-powered Context-aware DPM (SCDPM) platform for vigilant health monitoring including motion, ECG, and environmental data collection. The SCDPM is an ultralow power platform which performs better than state-of-the-art health monitoring platforms regarding system power consumption and the dynamic power management and adaptive sensing capabilities. The entire system comprises the work of hardware system design, embedded system programming for the sensor node, Android application design on the phone side, and power modeling. The code of the platform is open sourced [28].

# **2 Motivating Self-Powered Body Sensor Networks**

## **2.1 Body Sensor Networks**

Body sensor networks (BSNs) have shown significant potential in health applications by empowering researchers, scientists, and doctors to explore correlations between human-related sensor data and human health through remote continuous data collection. To enable such long-term continuous monitoring, the operating time of body sensor networks is a significant concern and energy harvesting from ambient environment is a promising solution. This dissertation research aims at addressing energy challenges encountered in self-powered BSN design, by exploring the real-world energy harvesting dynamics and improving the dynamic power management.

In a typical BSN as shown in Figure 2.1. One or multiple sensors are deployed in different locations on a human body, for instance, on wrists or chest. The collected sensor data are usually transferred to a data aggregator, like a smartphone, for data processing and visualization. The data could also be uploaded to a remote cloud server for data storage and processing. Doctors or researchers could remotely access the data, make analysis, and give a diagnosis or feedback to the user.

Considering the wearing comfortability for human subjects, the form factors and weight of sensor nodes and batteries are usually quite small, and the batteries are hard to support long operating time of the sensor nodes. The burden of frequent recharge or replacement of batteries could impede widespread adoption of BSN.

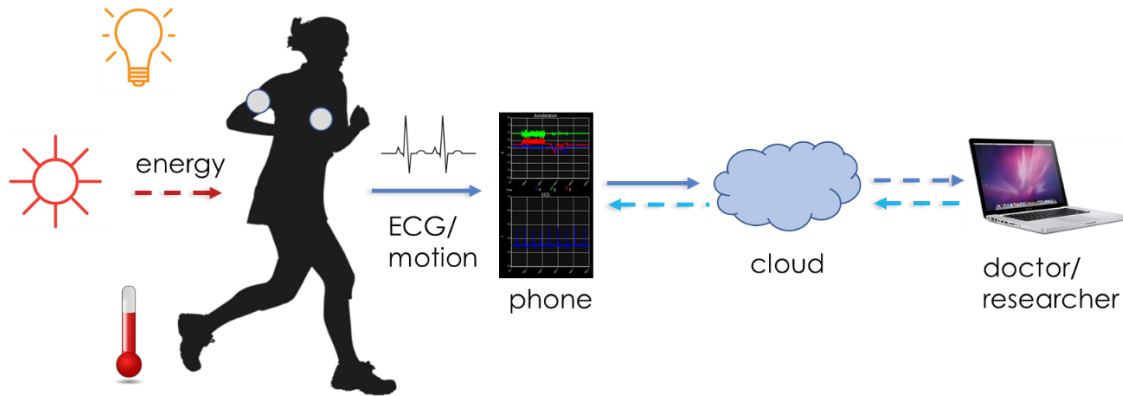


**Figure 2.1 Self-powered body sensor networks. The sensor nodes harvest energy from the environment and the human body, collect sensor data, and transmit data to a phone. The phone uploads the data to a cloud service for data storage and processing.**

In order to address this issue, two primary approaches have been explored: a) saving power consumption utilizing ultra-low power technologies for BSN and b) harvesting energy from the ambient environment to achieve the quasi-perpetual operating time. For the first approach, ultra-low power techniques have been studied including System on Chip (SoC) design[29]–[34], sensor design[35][36], wireless communication transceiver and protocols[37]–[42], and data transmission strategies[43]–[47]. In Appendix A.1, a case study of designing and implementing a data aggregation solution for custom ultra-low power radio is presented. The data aggregator is validated to be efficient for data aggregation, visualization, and cloud computing. Compared with commercial wireless communication protocols like Bluetooth[48] and ZigBee[49], the custom Ultrawide-band (UWB) radio[30][50] reduces much power consumption.

The second approach, harvesting energy from the ambient environment in real-world scenarios has been attracting researchers' interests recently, and it is the focus of this dissertation. Energy harvesting technologies have been leveraged by researchers in BSN area to develop self-powered sensor systems. Self-powered BSN capable of quasi-perpetual operation enables truly continuous monitoring of human subjects even beyond the clinic.

## **2.2 Energy Harvesting and Sources**

The energy sources from environment and human body include solar (indoor/outdoor)[34]–[47], thermoelectric[47]–[52], piezoelectric[53]–[59], RF[60]–[65], wind[66]–[69], and some others. Among them, solar and thermoelectric energy are good candidates for BSN applications considering the availability and the amount of harvested energy. For solar energy harvesting, indoor environments are more important since most deployments occur in hospitals, homes, gymnasiums, and offices. Compared with outdoor solar energy harvesting which has been studied for a long time[34][37][40][44], indoor solar energy harvesting is quite different. First, indoor light is usually incandescent light, fluorescent light, LED, rather than the sun[35]. The radiant spectrum of different light sources differs and affects the efficiency of solar cells. Second, the indoor light has a much lower illumination level which is usually less than 1000 lux, compared to outdoor sunlight around 10000~ 200000lux[35][36]. The power density of indoor solar is around  $1\mu\text{W}/\text{mm}^2$ [36]. Third, the indoor light is more controlled by people and has little dependence on weather or seasonal changes.

For thermal energy harvesting, since human beings are warm-blooded, they are the heat sources for objects attached to the skin. Therefore, thermoelectric generators (TEGs) can be applied to collect human body heat and generate electrical power. Regarding the comfortability for humans to wear TEG devices, it is popular to attach TEGs on the wrist or arm[51]. The power density of

TEG is  $250\mu\text{W}$  in daytime corresponding to  $20\mu\text{W}/\text{cm}^2$ [52]. Solar and thermal energy harvesting could be utilized separately or collaboratively to support BSN applications[47].

## **2.3 Summary**

In this chapter, we discussed the emergence of BSNs for health monitoring, and the energy harvesting technologies to enable batter-less self-powered BSNs. The energy sources are discussed, and solar and thermoelectric energy sources are the focus of this work. In the following sections, we will discuss the main contributions of this work exploring how to efficiently utilize the harvested energy through profiling, prediction leveraging context information, and dynamic power management.

# 3 Energy Harvesting Profiling

A critical challenge encountered when designing self-powered energy harvesting BSN applications is the discontinuity nature of energy sources[12][13][14]. The dynamic characteristics of energy harvesting in real-world scenarios and their implications on the design of self-powered BSN are of profound importance, while not well studied yet. Besides characterizing energy harvesters or making simulations in the lab, we designed a platform to harvest solar and thermoelectric energy and collect data on environmental and human activities. To explore the energy harvesting dynamics in the real world, we profile energy harvesting using our Energy Harvesting and Data Collection (EHDC) platform.

An overview of a typical energy harvesting system is introduced in Section 3.1. Related work of energy harvesting profiling is discussed in Section 3.2. The system design of EHDC is described in Section 3.3. Energy profiling results using the EHDC are presented in Section 3.3. Finally, in Section 3.4 a Lighting IoT Test Environment (LITE) platform based on the EHDC platform is designed to simulate and replay light profiles for self-powered system design.

The work presented in Section 3.1 ~ Section 3.3 was published in [52], and the work in Section 3.4 was published in [53].

### 3.1 An Overview of Energy Harvesting Systems

In a typical energy harvesting system, there are four modules: energy harvesting, energy conversion, energy storage and energy consumption, as shown in Figure 3.1.

The primary component of this system is the energy harvesting module since it transforms a form of renewable energy into electrical energy. Harvesters include solar panels, TEG, and other devices depending on the energy sources. Since the output voltage level of harvesters in BSN applications which commonly in the order of mV is insufficient to power electronics like sensors and microcontrollers, energy conversion module is required in most of energy harvesting systems. Ultra-low power boost converters managing  $\mu W$  to  $mW$  power are utilized for energy conversion to increase the voltage to a certain level. In addition, boost converters designed for energy harvesting application are usually capable of extracting the maximum power from harvesters through dynamic maximum power point tracking (MPPT). The efficiency of the boost converter is defined as  $\eta_c$  to model the intrinsic power loss through the boost converter. After converting the voltage to a certain level  $V_s$ , the energy is stored in a supercapacitor for dissipation. The energy feeds into regulators to provide specific voltages for electrical components. Regulators are utilized to provide one or more voltage levels for the loads with an efficiency  $\eta_r$ .

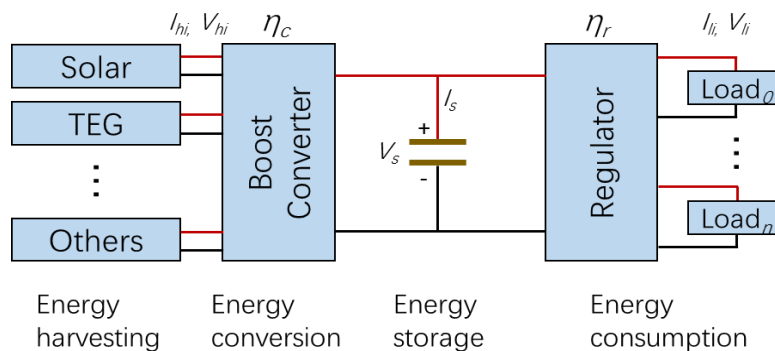


**Figure 3.1 Diagram of a typical energy harvesting system which consists of four modules: energy harvesting, energy conversion, energy storage, and energy consumption.**

## 3.2 Related Work

The intermittency and discontinuity nature of energy sources in the real world is a critical concern in self-powered BSN design [12]–[14]. The dynamic characteristics of energy harvesting in real-world scenarios and their implications on the design of self-powered BSN are of profound importance, while not well studied yet. Conventional ways usually characterize energy harvesters or make simulations in the lab[12], [13], [15]–[26], without much consideration in real-world dynamics.

Some research groups profile energy harvesting to explore the relationship between harvested energy and the environmental factors. For instance, in solar energy harvesting area, researchers create profiles for months or even years to explore the relation between solar energy harvesting and environmental dynamics[19]. However, in BSN area, besides environmental factors, human behavior has a significant influence on energy harvesting and should be taken into consideration.

Since human behavior profoundly impacts and dominates energy harvesting performance in body sensor networks, having a better understanding of how such behavior correlates with energy harvesting is fundamental to achieve self-powered sensor systems. One way to accomplish this understanding is by collecting energy profiles for heterogeneous energy sources available in the environment where self-powered sensors are deployed.

In [54], power profiles for indoor solar energy harvesting are presented. The profiles were elaborated with data collected over one year, and simulation for a specific load is designed to show the application of these profiles. The limitation of this work relies on the fact that the energy transducer was fixed next to a window, the interest for BSNs is to have profiles that consider human activity since the nodes are usually attached to people's bodies. Regarding thermoelectric energy harvesting profiling, the research conducted in this topic is significantly less than the case

of indoor solar. One of the few studies focusing on characterizing this type of energy harvesting for wearable devices is presented in [55]. This work shows the correlation of the power generated for one activity (cycling) over one hour and mentions the average amount of energy harvested while working in the office but it does not present a full profile for different activities over more extended periods of time. One of the aims of this work is to present an energy profile over several hours for different ordinary daily activities, both at work and at home.

The targets of energy profiling in this work include two aspects: a) explore the energy available and dynamics in the real world, and 2) establish relations between energy harvesting and environmental and human factors for energy modeling and prediction.

### **3.3 EHDC: Energy Harvesting and Data Collection Platform<sup>1</sup>**

The target of the EHDC platform is to collect energy harvesting profiles of BSN and explore the relationship between energy harvesting and the dynamics of human activity and the environment.

Following the described topology in Figure 3.1, for the specific case of energy harvesting module, we selected an amorphous solar cell AM-1417CA from Sanyo and Marlow SP5424-04AC thermoelectric generators (TEGs). A heatsink is attached to the cold side of each TEG to maximize the temperature difference across the TEGs. For the energy conversion module, we use BQ25504 from Texas Instruments for solar energy harvesting and LTC3108 for thermoelectric energy. BQ25504 has MPPT function and could be cold-started from 330mV. The LTC3108 can be operated from inputs as low as 20mV which is suitable for thermoelectrical energy harvesting. The

---

<sup>1</sup> In this project, Luis Lopez Ruiz worked on most of the design and implementation of the EHDC hardware platform. The author of the dissertation worked on the software design and implementation. The profiles were collected by Luis Lopez Ruiz and the author of this dissertation.

harvested energy is stored in a supercapacitor AVX BZ155B823ZNB with the capacitance of 82mF, and an LT3009 is used to regulate voltage.

In the platform, light intensity and temperature of the skin and ambient air are sensed as environmental factors which are related to solar and thermoelectric energy harvesting. To measure light illumination at which the solar cells are exposed, the NOA1212 from On Semiconductor is attached close to solar cells. The range of light intensity could be adjusted up to 100000 lux. In order to measure the temperature difference between two ends of a TEG pad, two MAX6605 temperature sensors from Maxim Integrated are used. One is attached to the skin under the armband to measure the temperature of the hot end, and the other is put close to the TEG heatsink to measure the cold end. In order to track human activity level, the ADXL326 accelerometer from Analog Devices is applied in the platform.

To measure the instantaneously usable power, we monitored the current delivered by the boost converter and its output voltage. A current shunt monitor INA285 from Texas Instruments is used to allow us to monitor minimal currents while also minimizing losses. A 16-channel analog to digital converter (ADC) AD7490 from Analog Devices is used to sample analog signals including signals from environmental sensors, the accelerometer, and current and voltage of energy harvesters.

In the first version, we used standalone electrical components on a breadboard connecting to Shimmer nodes as a data logger, as shown in Figure 3.2. Then we designed the EHDC hardware platform, a daughter board integrating all sensor and energy harvesting modules and connected it to a Raspberry Pi 0 board as a data logger and controller.

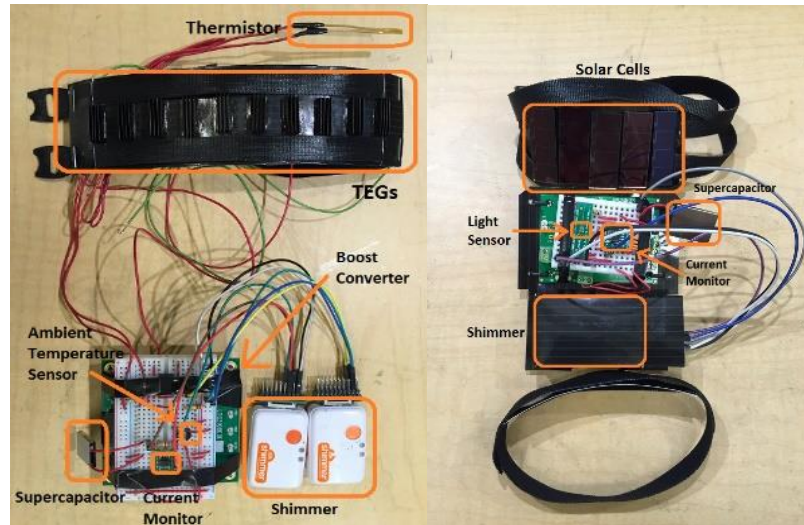


**Figure 3.2 The first version platform which includes standalone components on breadboards connecting to Shimmer nodes.**

The diagram of the EHDC platform is shown in Figure 3.3. The daughter board includes the sensing module, the energy harvesting module, and related circuitry. A variable load is included in the platform to simulate the load of a sensor node which is potential to test power management. The daughter board interfaces Raspberry Pi 0 with I<sup>2</sup>C, SPI, and GPIO ports. The Raspberry Pi 0 uses Linux as the operating system (OS), and we designed Java application for controlling, data logging, data compressing, and data storage, as shown in Figure 3.4. The collected sensor data was stored in a micro SD card and to reduce the power expended with each logging, and the data was compressed into binary files. Additional software was developed to enable uploading the sensor data to a custom cloud server for data visualization and storage in real time.

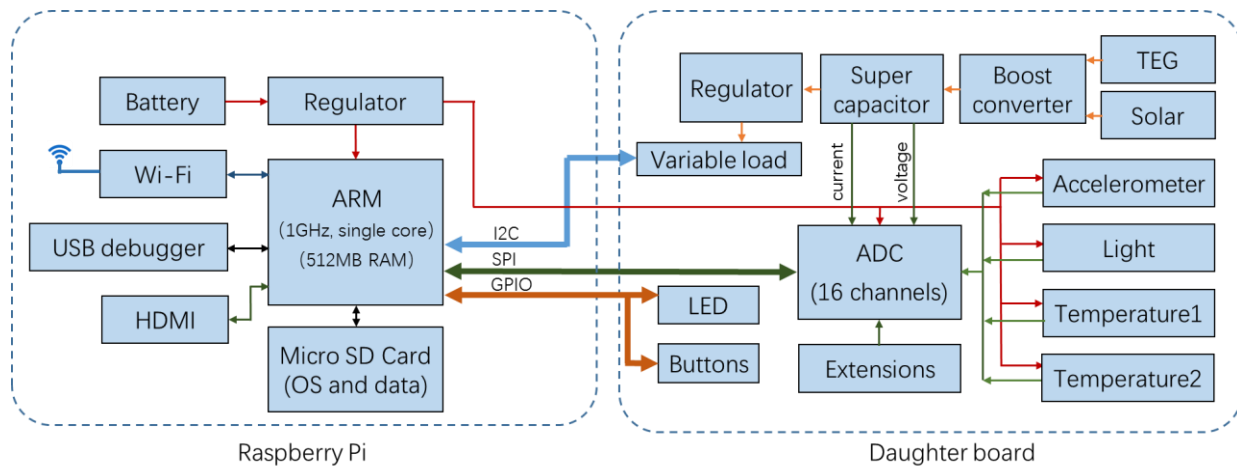


**Figure 3.3 Block diagram of the EHDC platform and the interface with the Raspberry Pi 0.**

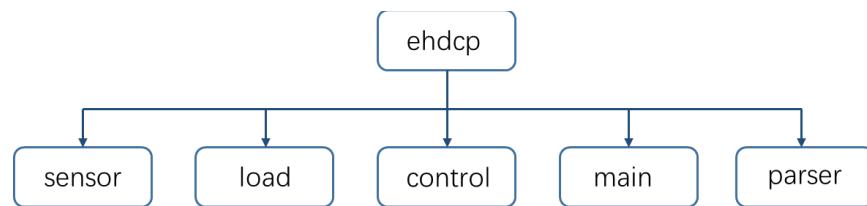


**Figure 3.4 Software architecture for EHDC platform.**

The EHDC platform and the deployment on a human subject are shown in Figure 3.5. The designed EHDC platform is capable of profiling multi-source energy harvesting with environmental and human factors, which could be utilized in general research in energy harvesting area. The EHDC could be easily extended to include other energy sources like piezoelectric energy. In our research, we use EHDC for energy profiling and then for modeling, as discussed in the following sections.

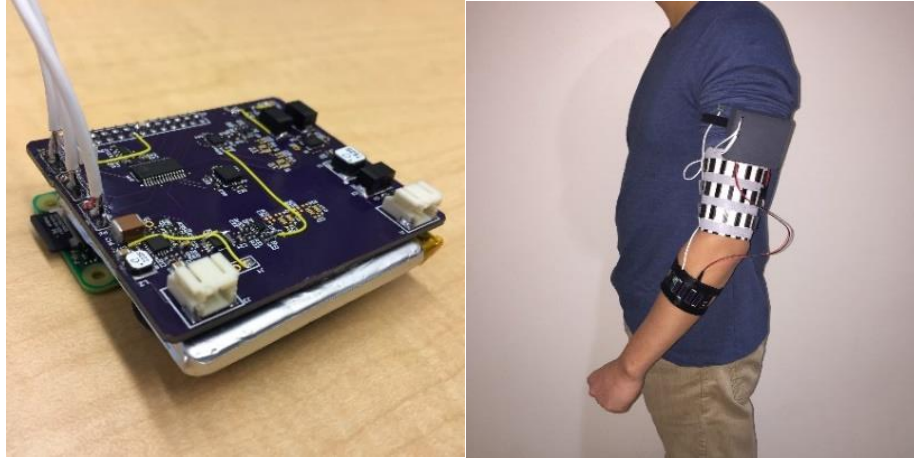


**Figure 3.5 From left to right, the full EHDC platform for multi-source energy harvesting and the platform deployed on a human subject.**

### **3.4 Experiments and Results**

We collected energy profiles with EHDC platform from two male subjects for several days. The subjects were wearing the platform for several hours each day to collect data in a mainly indoor environment in the office or at home. The activities include working at a desk, walking around, eating, cooking, and some others. More than 80% of them are indoor activities, and there are some outdoor activities like walking and driving.

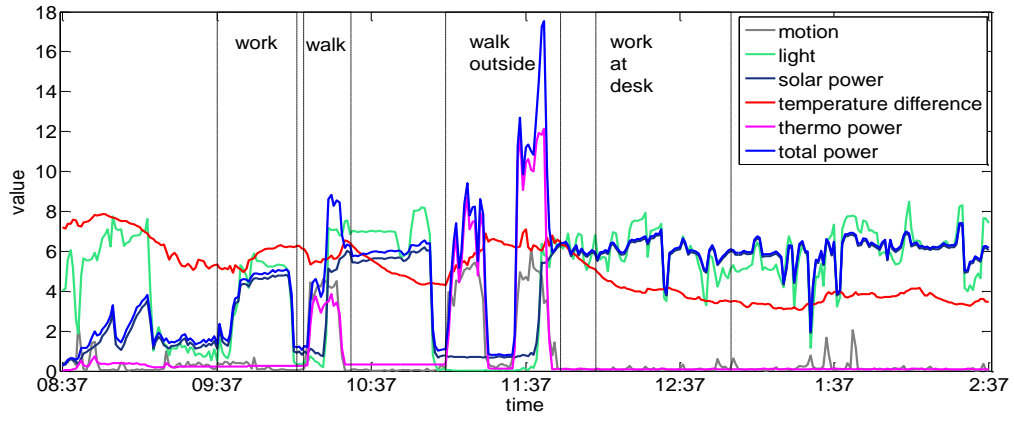
The energy profile includes motion (Teager calculator[56] is utilized to assess the motion level), light intensity, averaged solar power ( $\mu\text{W}$ ), the temperature difference between skin and ambient air ( $^{\circ}\text{C}$ ), averaged thermoelectric power ( $\mu\text{W}$ ), and total power ( $\mu\text{W}$ ). To fit all data series in a figure, the unit of light intensity is 100lux, and Teager energy is scaled. The four profiles are shown in Figure 3.6.

The first two energy profiles were collected mainly indoor at home and in office. The activities include indoor activities like working in the office, walking around, eating, and doing housework (sweeping mopping floor, cleaning, etc.) The average light intensity of two days was 469lux and

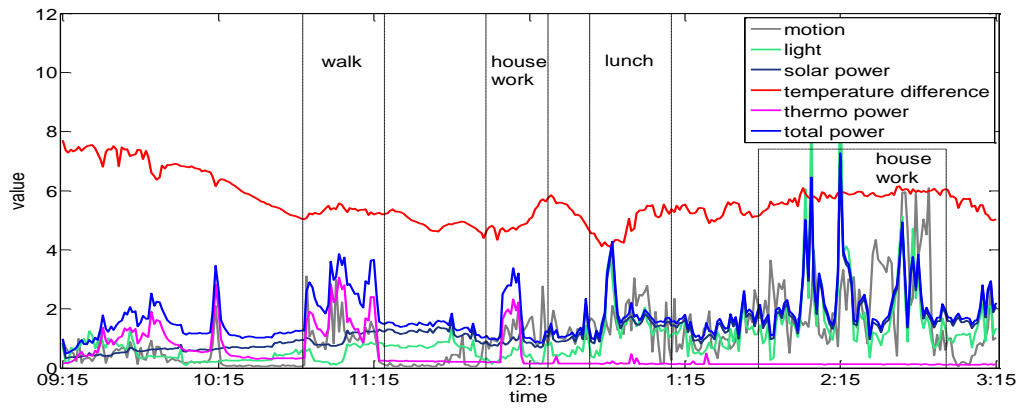
101lux, respectively. The air temperature was around 25°C, and the average temperature difference was 5~6°C for both days. The average power was 5.1uW and 1.7uW respectively.

The last two profiles were collected both indoor and outdoor. In figure (c), the profile was collected at night, and activities indoor cooking, working at a desk, walking around, and a short period of outdoor activities: walking outside and driving. The average indoor light intensity was 209.0lux, and around 0lux outdoor since it was midnight. The average temperature difference indoor was 1.1°C, and 6.1°C when walking outdoors. The average indoor power was 3.6μW, and average outdoor power was 41.7μW which consists mainly of thermal energy. Figure (d) displayed a profile created in the office. The activities include indoor walking, working at a desk, and outdoor walking. The average light intensity in the office is 537.1lux, and more than 10000lux outdoor. The average temperature difference was 5.0°C when the subject was walking indoor, and only 0.9°C when sitting at a desk. When walking outdoors, the average temperature difference was 9.7°C. The average indoor power was 7.1μW, and average outdoor power was 171.4μW.

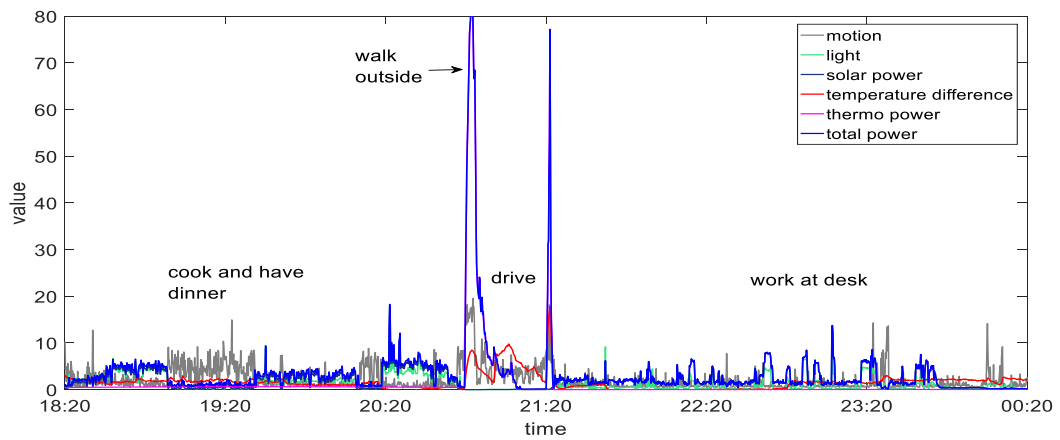
From the experiments, we find that in an indoor environment, most of the time solar power dominates the total power profile. In certain situations, such as walking the thermoelectric power dominates due to the arms movement. In an outdoor environment, since the ambient air temperature is low in winter, there is much more thermal energy harvested than indoor. The light intensity and harvesting power have a good linear relationship. On the other hand, the temperature difference and harvested thermoelectric power are not well linearly related. Instead, thermoelectric power is related to the motion for some time. Such a relationship indicates that human activity level which relates to airflow has a significant influence on thermoelectric energy harvesting.



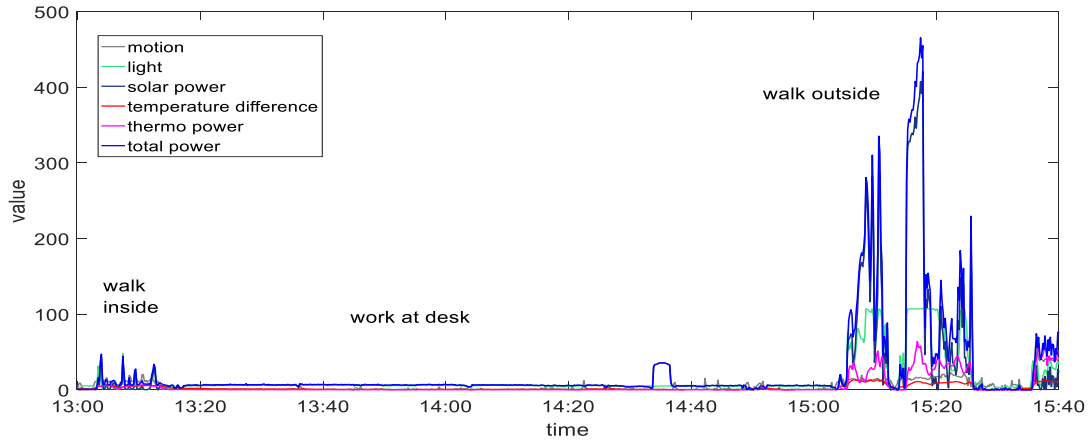
(a)



(b)



(c)



(d)

**Figure 3.6 Energy harvesting profiles for four sessions.**

### 3.5 Lighting Environment Simulation with EHDC<sup>2</sup>

In the last part of this chapter, we discuss the Lighting IoT Test Environment (LITE) platform based on the EHDC as a demonstration of the broader usage of EHDC in IoT. This work has been published in [53] and part of the content and results are from the paper.

The LITE platform is a tool that provides insight on solar powered energy harvesting systems operate in low lighting environments, and it can physically emulate a variety of indoor lighting sources with mapping technique. In Section 3.4 we discussed the energy harvesting profiling, and here we can simulate the time-series light profiles in the LITE platform. The LITE platform performs both light source emulation and time-series light profiles simulation on an isolated hardware system. The combination of these two capabilities enables realistic lighting profile re-creation. For hardware engineers and prototypers, the LITE platform can rapidly reveal the

---

<sup>2</sup> This project was done with Henry Bishop and Peng Wang. They worked on the physical apparatus implementation, experiments of light sources emulation, mapping functions for calibration and emulation, and some other experiments. The author of this dissertation worked mainly on the algorithm and software on the EHDC for implementing the calibration, emulation, and simulation. Also the author worked on some of the experiments, hardware test, and data collection of profiles.

effectiveness of a harvesting circuit or commercial off-the-shelf (COTS) systems to demonstrate a proof of concept. The light source emulation and time-series simulation capabilities are characterized with a worst case mean absolute percentage error (MAPE) of 3.2% and 0.5%, respectively. The LITE platform better equips engineers to design, debug, and deploy self-powered sensor systems by experimenting with how these self-powered systems work under real-world conditions.

### **3.5.1 Hardware Platform**

The LITE platform consists of three components: the physical apparatus where simulations and measurements take place, the custom LED lighting array and control hardware circuitry that provides lighting capabilities, and the EHDC platform as the control system. High accuracy and repeatability were requirements for the platform to provide exact and consistent light profile simulations. Figure 3.7 shows a system block diagram of the platform proposed in this paper.

Isolating the test space from external light is crucial for experimental control. A 1 x 1 x 1.2 cubic foot enclosure was designed to meet this requirement as shown in Figure 3.8. With the frame constructed from 8020 T-slotted aluminum beams, the left, right, and back side panels were covered in opaque, black acrylic sheets laser cut to size ensuring minimal leakage. The top and front of the platform were covered with thick fabric providing substantial light isolation as well as easy accessibility to the internals of the apparatus. A single piece of acrylic was used to support the LED lighting array and drivers. The acrylic sheet attached to the four vertical 8020 columns enabling the light source to be moved closer or further away from the system to test.

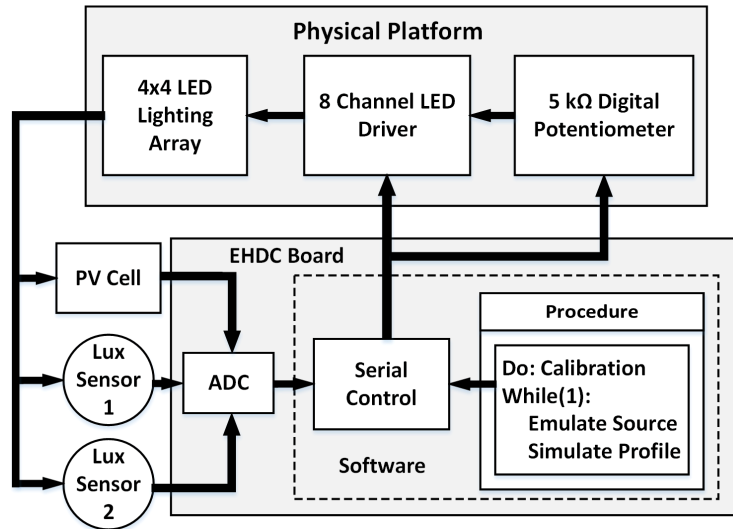


**Figure 3.7 System block diagram of the LITE Platform consisting of the EHDC board's hardware and software components, the physical LITE apparatus, PV cell (DUT), and lux sensors.**

The platform's lighting array consists of sixteen, 5000k cool white LEDs arranged in sets of two, which matches the number of current sinks provided by the driver. This lighting array was typically operated at a height over 16 cm to provide a relatively distributed amount of light across the area where the sensors and PV cell were positioned. The driver board comprises a TI TLC59108 LED driver and a Microchip MCP4261 digital potentiometer. The driver has eight constant current sink inputs requiring two LEDs per channel and communicates with the EHDC platform over an I<sup>2</sup>C interface. The digital potentiometer communicates with EHDC via an SPI interface. The driver uses two separate lighting control mechanisms: inverse linear control of current through the digital potentiometer and piecewise linear control of current via control bits internal to the driver.

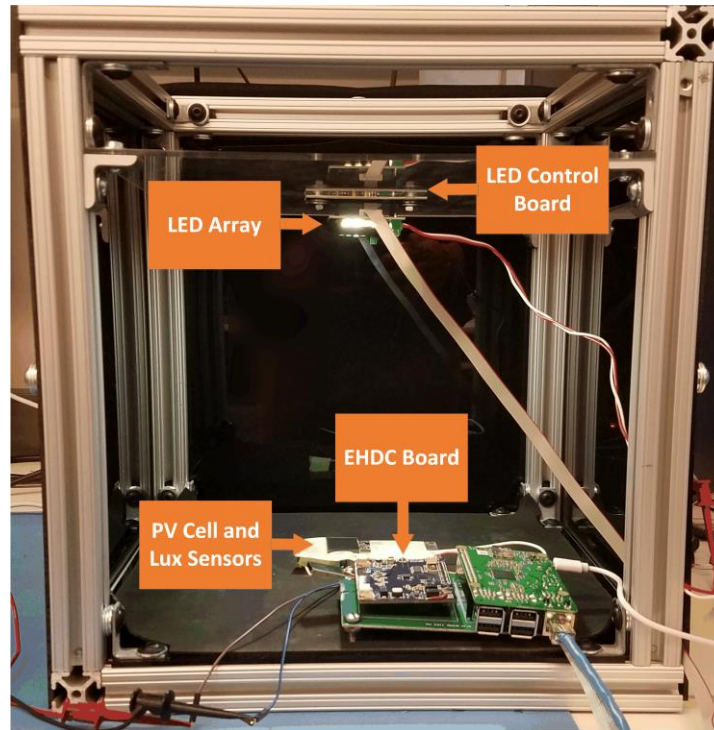


**Figure 3.8 LITE platform implementation based on the block diagram.**

An SLMD600H10L monocrystalline solar cell produced by IXYS is used with the light sensors on the EHDC. The sensors and the PV cells were placed as close to one another as possible during the experiments.

### **3.5.2 Calibration of the Lighting System**

Different from functions in energy profiling, the purpose of EHDC in LITE is to generate the specific lux values in the apparatus from an input. A calibration stage is required to create a regression-based profile that translates any desired input lux value to control bits for the driver board.

The platform takes an input of desired lux values and outputs generated light with an equivalent value to the input. Control application is used to translate lux into driver control bits. To achieve this, we calibrated the system by selecting five LED driver gain bits and sweeping all potentiometer control bits for each gain. The resulting lux values are recorded in five curves. This mapping from

control bits to generated lux is inverted such that the input is lux and output is control bits. Four of these calibration curves created for the LITE platform are shown in Figure 3.9. Out of these five inverted curves, a single piecewise mapping function is created. These steps allow the apparatus' input and output to be in lux. A limitation of this method is that recalibration is required if the platform setup is altered such as LED settings, distance, or other conditions.

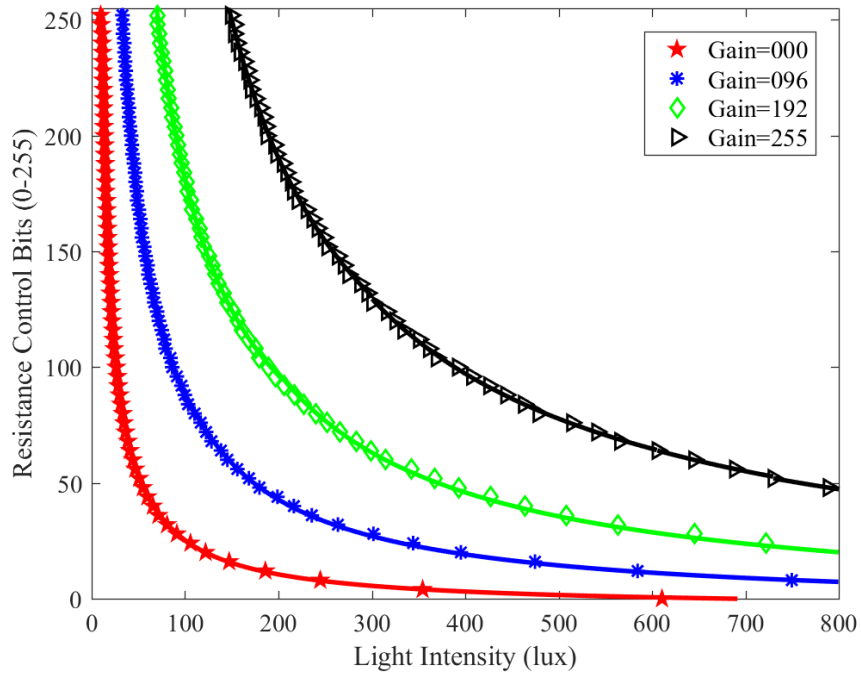


**Figure 3.9 The relationship between light intensity and resistance control bits and gain.**

The calibrated low light operating range is from 30 to 800 lux which is normal indoor lighting range. Eight LED driver gains are selected to increase the span of possible lux values. For every gain value, all potentiometer control bits from 0 to 255 are swept. After curve fitting the data and piecing together eight sections from each curve, a piecewise, inverse linear equation is generated. The root-mean-square error (RMSE) between user input lux values and generated lux values collected from the lux sensor is 12.32 lux. Figure 3.10 illustrates the relative error across lux values from the piecewise calibration equation.

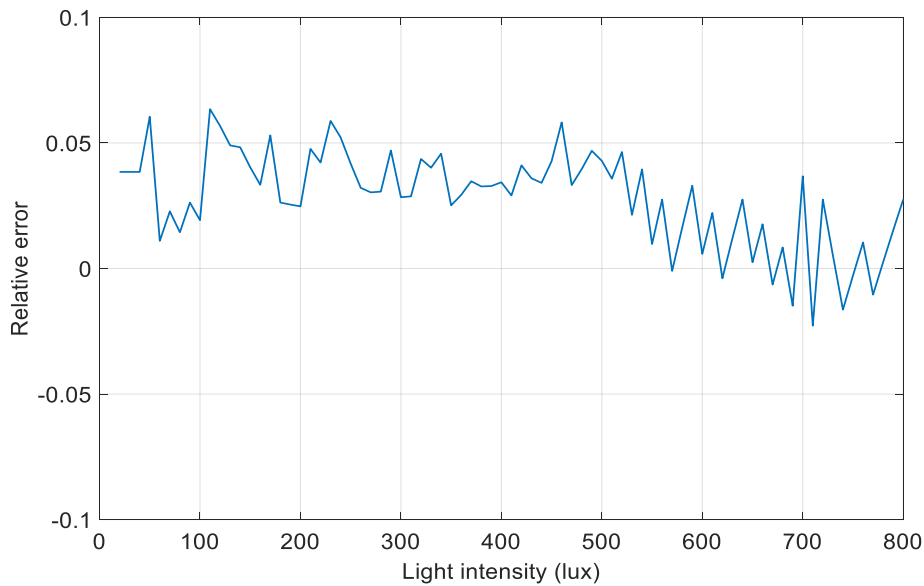


**Figure 3.10 Relative error between input (ideal) lux and output (generated) lux of the apparatus. The calibration equation turns an input lux stream into control bits, which in turn creates real light that should match in value to the input.**

### 3.5.3 Light Source Emulation and Mapping Functions

Each type of solar cells has its spectral sensitivity range. For instance, polycrystalline cells have a spectral sensitivity range of 500 nm to 1100 nm and are usually used in outdoor applications; monocrystalline cells have a spectral sensitivity range from 300 nm to 1100 nm which could be used in both indoor and outdoor environment; and amorphous cells have a range of 300 nm to 600 nm and are used in predominantly indoors[57].

On the other side, the different light sources also have different spectral, thus have a different effect on solar cells even with the same light intensity. Therefore, emulating different light sources could help to recreate the light scenarios accurately. The LITE platform uses the LED to emulate different light sources by employing specific mapping functions. There are two steps to accomplish this. Firstly, a relative set of equations describing the relationship between the light intensity of each light source and power for PV cells need to be made. Secondly, using those relationships a

mapping equation must be constructed to demonstrate how to convert any other light source to a specific light source, and in this project, it is the LED.

Concerning PV cell power, the EH systems typically utilize boost converters with maximum power point tracking (MPPT) function to extract the most power possible under the immediate conditions. This assumption is essential when considering mapping because changing the load will change the mapping equation. Bounding the scope to only consider nodes using MPP tracking (MPPT), far less information needs to be gathered from every light source.

This paper presents the mapping results for the following types of light sources in Figure 3.11: 5000k white LED, compact fluorescent lamp (CFL), fluorescent lamp, incandescent bulb, and the sun. The LED curve is omitted since it is used for emulating other sources. Even though the lux range in Figure 3.11 was capped at 800 lux, some measured lux points exceeded this value ensuring that each curve was accurate beyond the bounds of interest for this apparatus. The accuracy of the sensors and measurements limited the lower bound of the range to approximately 30 lux. All IV curves were created using software to sweep current and measure voltage with a Keithley 2400 source meter.

The verification result of the mapping functions is also illustrated in Figure 3.11 by the dashed lines which represent the emulated curves of the light source that the symbol is hovering over. The LED curve has been modified in such a way that it entirely acts as another source's curve. The mapping technique for this experiment was completed in three steps. Firstly, eight lux values associated with a particular source were chosen. Secondly, the MPPs associated with those lux values were derived and then used to solve for the equivalent LED lux that would produce that power. Thirdly, the LED lux values were applied to the platform's input generating the specific lux inside of the platform.

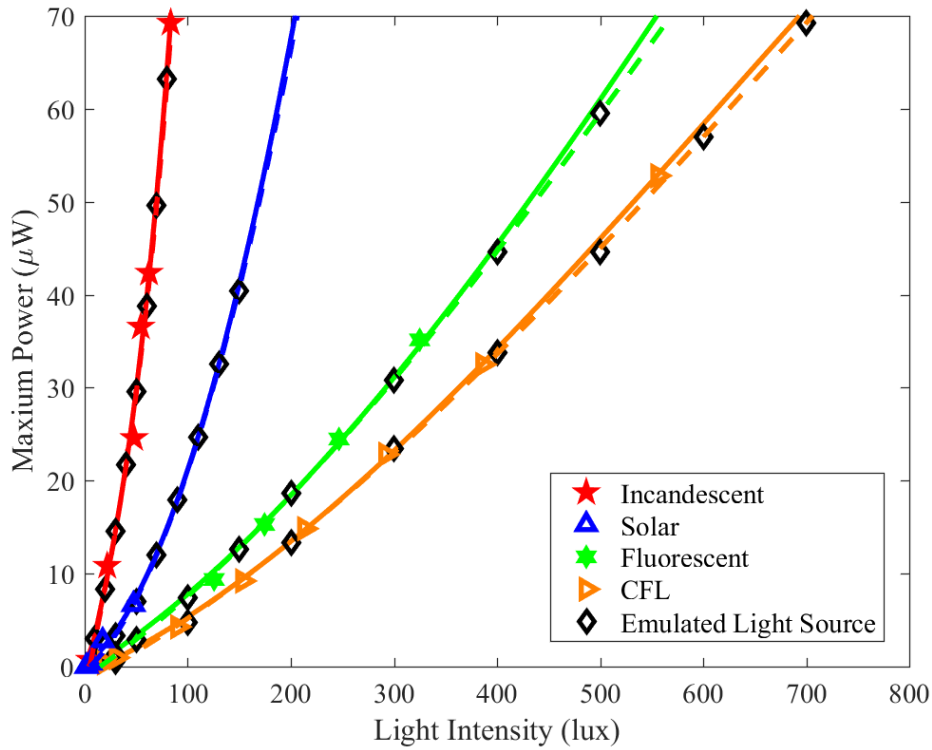


**Figure 3.11 Lux-power curves are showing the relationships between light intensity and maximum power obtained from the data of four typical light sources. The LED is used to emulate the other four types of light sources and shown by the dashed lines and diamond symbols.**

There is visibly little error between the original curve and its emulated counterpart. To demonstrate the actual error over each set, all four light sources' RMSE and MAPE values are given in Table 3.1. From this table, the data shows that the mapping functionality of the platform works very well over the given intensity range with the incandescent source having the highest accuracy.

**Table 3.1 Mapping RMSE and percentage error.**

	CFL	Fluorescent	Incandescent	Solar
<b>RMSE</b>	0.828 $\mu$ W	0.804 $\mu$ W	0.780 $\mu$ W	2.423 $\mu$ W
<b>Percentage Error</b>	3.2%	2.5%	1.4%	2.1%

### 3.5.4 Simulations of Time-series Profiles

The time-series simulation capability of the LITE platform requires discrete time, lux-based datasets to operate. The EHDC board collected multiple environmental profiles for a variety of lighting sources that the platform can emulate and lux sequences could be generated by the software application in EHDC. After calibration and light source emulation, the apparatus is capable of simulating time-series light profiles. The Java-based simulation program takes an array of lux values and a delay parameter as inputs. It then controls the LED array by sending control bits to the LED driver. In the experiment, 800ms was used as the delay parameter.

Figure 3.12 illustrated a 12 minutes lighting profile collected in a lab under the fluorescent light. The dashed curve represents the emulated power-equivalent input profile converting fluorescent lux to LED lux using the mapping equations. The RMSE is approximately four lux, and the MAPE is half a percent. The small error between the expected and measured light intensities effectively means the platform's performance does not vary over time. Figure 3.13 compares the time-series power profiles during this period. The emulation matches the original power profile well except one point around the 7th minute.

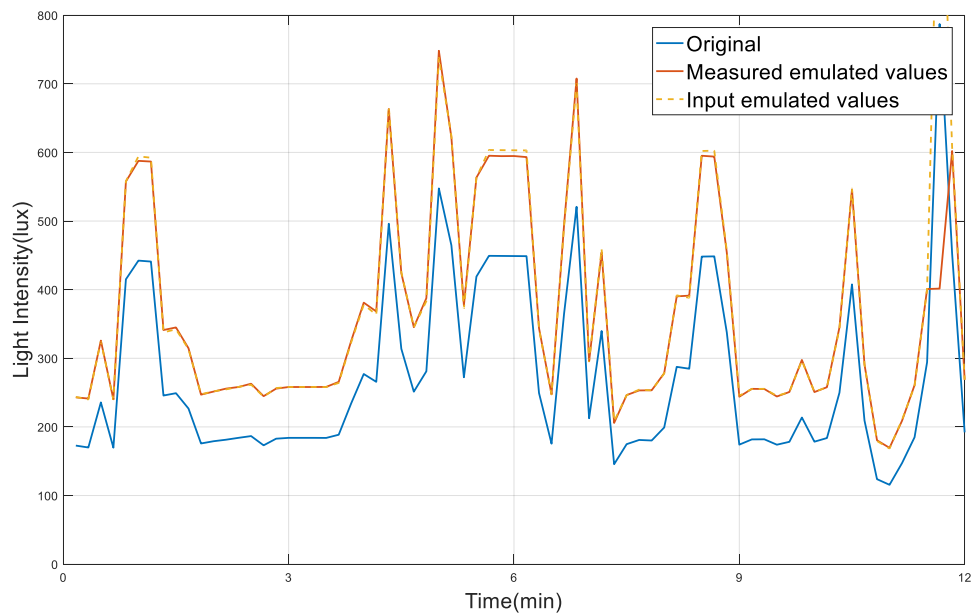


**Figure 3.12 Time-series light profile simulation. The yellow dashed line represents the calculated power-equivalent LED lux sequence, and the orange line is the measured lux values which match the input well.**

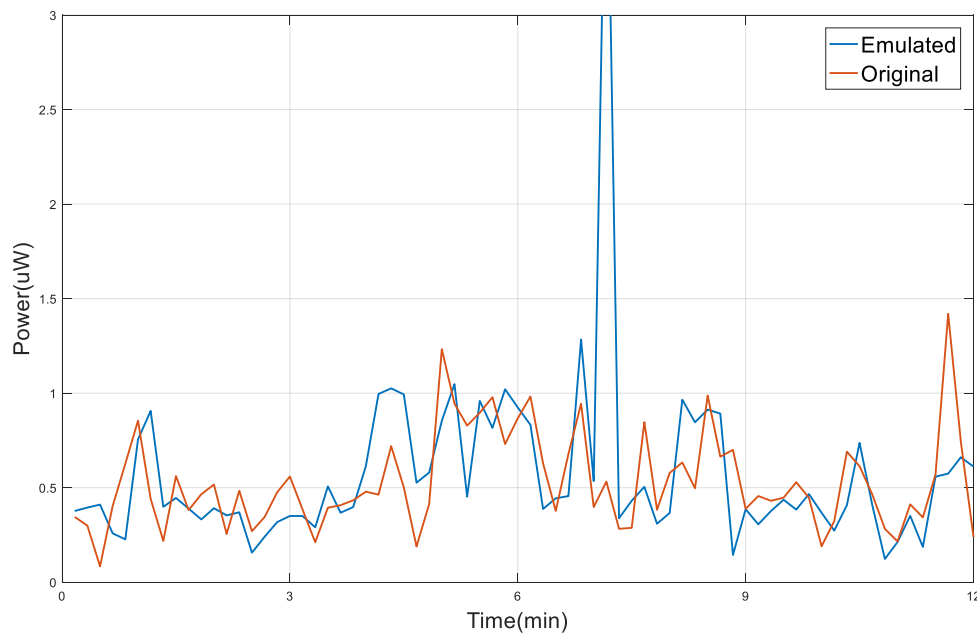


**Figure 3.13 Time-series power profile. The emulated curve matches the original power profile well except one point around the 7th minute.**

To conclude, the LITE platform helps designers to understand how a physical node operates in realistic energy harvesting conditions by providing a completely customizable, physically simulated lighting environment for testing these systems. Future work mainly includes expanding the emulation capabilities of the platform as well as improving the accuracy of the system.

### **3.6 Summary**

This chapter discusses the energy harvesting profiling for BSNs. An EHDC platform is designed for this purpose, and the profiles are presented. Finally, a LITE platform based on the EHDC is introduced for light environment simulation. The experiments and results demonstrated that:

- Energy profiling regarding the ambient environment and human factors could help understand the energy harvesting dynamics in the real world.
- The LITE simulation platform could help validate solar-powered designs using profiles in real-world scenarios.

# 4 Energy Harvesting Prediction

The discontinuous and dynamic characteristics of energy harvesting in real-world scenarios – and their implications on the design and operation of self-powered systems – are critical for self-powered BSN engineers. The frequently used energy sources including solar and thermal are all intermittent and discontinuous. The [58] discussed and classified energy sources in different types according to their controllability and predictability. Only a few energy sources like self-powered flashlights are entirely controlled by the user whenever needed. Most other sources like wind, solar, and thermal are usually uncontrollable. In other words, the user cannot fully control them to generate the required amount of energy at desired times. However, most of the uncontrolled energy sources could be modeled, and the expected behavior could be predicted in a given time horizon with limited error margin. There isn't a clear boundary between the definitions of unpredictable and predictable energy sources, but the performance of prediction model complexity, accuracy, and prediction time horizon make it impractical to predict some energy sources in the real world. In the scope of this work, we discuss the uncontrollable and predictable energy sources of solar and thermoelectric.

Predicting or forecasting the harvested energy in advance could help to improve the performance of the system power management. Better prediction accuracy usually brings more

performance improvement as discussed in related works [12]–[19] and this is also proved in Section 5.5.

Context information related to energy harvesting could be utilized for energy prediction. Environmental variables such as light intensity and temperature, are directly related to solar and thermoelectric energy harvesting. Human activity level, inferred from motion sensors, affects harvested energy especially in an indoor environment as well[59]. Information from a smartphone, including GPS, indoor/outdoor, schedule, weather forecast, and others also help to infer the context which benefits for energy harvesting prediction. For instance, if the GPS shows the subject is in a building on campus, and there is a class going on according to the subject’s schedule, then we could predict the harvested energy in an hour with almost constant indoor temperature, and an indoor illumination level.

In this chapter, we discuss the energy prediction models in related works in Section 4.1. The prediction horizon, application scenarios, and performance of these models are analyzed. Inspired by these models, a context-aware hybrid model for both indoor and outdoor BSN energy harvesting prediction is proposed in Section 4.2. The model is more like a framework to demonstrate the idea of integrating context information to improve the prediction performance. We use a real-world profile to evaluate its performance on our custom SCDPM platform, and the experiments and results will be discussed in Section 7.3.

## **4.1 Related Work**

The harvested energy from a system is a time-series data sequence thus the energy harvesting prediction belongs to the time-series prediction field. Therefore, the classic methods that have been well discussed for time-series prediction could be utilized for energy prediction. The prediction models for time-series forecasting could be found in this book [60].

From the point of view of energy sources, many types of research focus on the outdoor solar energy harvesting, and the wind energy harvesting ranked the second. The outdoor solar and wind have strong cyclicity which draws the attention of the researchers. There is not much research on thermoelectric energy prediction, and one of the few that discussed the factors that affect TEG is [55] with short-term profiling. Technically, the thermoelectric energy prediction is almost equal to predict the temperature difference between two sides of the TEGs, and it highly depends on the experimental conditions. The indoor solar energy is similar to TEG, which is affected by experimental conditions or human factors. We focus our discussion on the solar and thermoelectric energy sources but also study models for other energy sources in related works.

Instead of discussing prediction models according to different energy sources, we organize the discussion of models by their underlying methodology.

#### **4.1.1 Exponential Weighted Moving Average Based Models**

Many of the previous research on energy harvesting techniques are focused on outdoor solar energy harvesting [16] [58][61][62]. The outdoor solar energy has a very strong diurnal cyclicity which is different from other energy sources such as thermal electric, RF, and others. Besides, the solar energy also has seasonality in a longer time horizon. The temporal weather conditions also affect the short-term solar energy harvesting which is from minutes level to hours level. Other factors like the angle between the solar cell and the light and temperature are not discussed much.

Among the prediction models, the Exponential Weighted Moving Average (EWMA) is a fundamental and effective model which utilized the EWMA filter[63]. The model exploits both the diurnal cycles of the solar energy and seasonal variations. It maintains a summary of historical energy harvesting values in each time slot of a day, and usually, the slot length is chosen as 30 minutes and the total slots in a day are 48. The value of energy harvested in each slot is maintained

as a weighted average of the energy collected in the time slot at that time of all observed days. The exponential weights result in decaying weights for profiles in older days. The EWMA model performs well since it handles the diurnal and seasonal cycles of the solar energy expertly. However, the primary limitation is that it fails to consider the weather conditions which has a significant effect on the solar energy harvesting but does not have periodicity. For example, the light intensity in cloudy and rainy days (~1000lux) could be significantly lower than that in sunny days (~10,000lux). Therefore, when different weather conditions alternate the algorithm could produce a significant error.

Noticed this issue there have been many researchers working on adding the weather effect to the EWMA model, and the way they deal with weather conditions is different. A Weather Conditioned Moving Average (WCMA) prediction is proposed in [62]. The model keeps  $D$  previous days data rather than one-day data used in EWMA, and they added a parameter  $GAP$  to indicate the solar conditions in the present day relative to the average of previous days. Similarly, in [61] a Weather-Conditioned Selective Moving Average (WCSMA) is proposed by using the trend similarity of energy harvesting and the classification of sunny and cloudy days. Especially, three datasets of sunny, cloudy, and mixed days are kept, and current data from the beginning till now is compared with these profiles to calculate the similarities. A weight factor array based on the similarity is used to estimate the energy in the current time slot. In [16], a prediction model was designed based on the additive decomposition (SEPAD) model. In the model, they divided the solar energy into three parts reflecting the diurnal cycle, seasonal effect, and temporal weather change. EWMA is implemented for each part, and then all parts are combined for the final prediction.

### 4.1.2 Profile-Based Models

Technically the EWMA model could be considered as a profile-based model as well since it maintains one day profile. The weather-related models based on EWMA discussed above require more than one profile to consider the weather conditions. For example, the WCMA in [62] requires  $D$  past days, and the WCSMA in [61] keeps three types of profiles for sunny, cloudy, and mixed days.

The profile energy model (Pro-Energy) in [17] developed the idea of profile-based prediction further. Different from keeping  $D$  past days profiles as in [62], it maintains  $D$  selected “typical” profiles of different weather conditions. The profile set is updated dynamically to discard old profiles and remove profiles which are too similar. The energy harvesting data of the current day from the beginning till current time slot is compared with each stored profile to calculate a similarity factor. Then the most similar profile is selected to predict data in the next time slot in a similar way to EWMA. It is further improved to select the top  $K$  most similar profiles and use the weighted average of them to predict.

The number of profiles should be large enough to represent different types of weather conditions. Compared with [61] which keeps three profile sets, the Pro-Energy could handle weather conditions better and have a higher prediction accuracy. The model is capable of providing accurate predictions for short-term and medium-term forecasting horizons.

### 4.1.3 Empirical Models

As mentioned, the energy prediction can be treated as a time-series prediction problem and utilize various empirical models. Empirical models only rely upon the observed relationships among experimental data, and the relationship could be utilized for forecasting. The empirical models usually have very limited or no information about the underlying mechanism of the system. Thus

the model may or may not have real-world interpretation. Therefore, the empirical models usually cannot be used for long-term prediction which requires more knowledge of the underlying system mechanism.

The empirical models are usually employed for short-term prediction with pretty good accuracy. Also, they usually have low computation complexity and memory requirement, which fit for fast, accurate short-term prediction.

Three commonly used statistical models including linear regression model, moving average, and exponential smoothing are discussed in [13]. The three different models are used for short-term solar energy prediction in a horizon of seconds to minutes level. They used the deadline miss rate of the system to evaluate the performance of energy prediction and power management, and they conclude that linear regression and moving average worked better on the simulation data. The prediction horizon is not designed for medium-term and long-term prediction.

In [15], six empirical statistical models including uniform distribution, geometric distribution, transformed geometric distribution, Poisson distribution, transformed Poisson distribution and a Markovian model are tested for both outdoor and indoor environments, and their results show that no single model fits all the data sets. This work mainly shows the limitation of empirical models.

#### **4.1.4 Weather Forecast Based Models**

In addition to the models discussed before, an entirely different model worth noting is proposed in [64] leveraging the weather forecast information to deal with the temporal weather change in outdoor solar and wind energy harvesting. The authors termed past predicts the future (PPF) to refer to the previous models discussed in 4.1.1 ~ 4.1.3 and argued the PPF models have least accurate at the time-scales of 3 hours to several days due to the significant inter-day and intra-day variations. Therefore, instead of seeking information from the past, it utilized weather forecast to enhance the

prediction ability. The hours-level weather forecast usually contains more information than the past data thus improving the prediction accuracy.

The performance of their forecast-based prediction model was compared with the PPF models in two case studies and showed better results. One possible limitation of the model could be the overhead of accessing and processing the weather information, as pointed in [17]. However, as the ubiquitous computing technologies, internet coverage, and IoT devices have been developed rapidly, the cost of accessing and processing diminishes.

More importantly, this idea could be developed by extending the “context information” beyond the weather forecast to acquire more information related to energy harvesting and integrate it in the prediction model rather than solely based on the past data.

From the point of view of general time-series prediction, adding context variables related to the model extends the univariate prediction model to a multivariate prediction model. By carefully selecting the related variables, the performance of the multivariable model could be better by leveraging the context information.

#### **4.1.5 Prediction Horizon**

In addition to the prediction accuracy, the prediction horizon is another critical factor to consider. The prediction accuracy usually changes along the forecast horizon as shown in [64]. The definitions of the short-term, medium-term, and long-term are not unified in energy harvesting area. According to most of the related papers, here we clarify the short-term to be the seconds to several minutes, medium-term to be minutes to hours, and long-term to be several hours to days. Longer time horizon like months or years is usually not considered.

The models discussed before are summarized in Table 4.1. Statistical empirical models like regression, moving average, smoothing and others are best for short-term prediction by focusing

on the trend and relationship from the observed data samples. In BSN energy harvesting, such short-term predictions are even more critical since the energy harvesting is highly dependent on the human motion which is random and changes in a short time-scale. For example, consider a solar energy harvesting system on a wristband, when the person moves or rotates his arm, the harvested energy could change significantly. Such behavior is impractical to model, and empirical models are a good fit for it.

The EWMA-based including the weather conditioned models usually divided a day into 30 minutes and predicted well in such a medium-term time horizon. The profile-based models as in [17] have good accuracy in both the medium and long-term prediction. Weather forecast based model proposed in [64] depends on the weather forecast time scale which is usually an hour to days. They concluded that the weather forecast based model performs well from 3 hours to 72 hours in future and better than PPF models.

**Table 4.1 Prediction horizon of different models.**

Prediction horizon	Models
Short-term (seconds ~minutes)	Empirical models
Medium-term (minutes ~ hour)	EWMA-based, weather-forecast-based, profile-based
Long-term (hours ~ days)	Profile-based Weather-forecast-based

#### 4.1.6 Hybrid Indoor and Outdoor Prediction For BSN

From the application perspective, most of the previous work is for general Wireless Sensor Networks (WSNs) rather than BSN. It often assumes the harvesters and the sensing system are fixated in a specific location, and the solar energy is mainly decided by the time of a day, seasonal changes, and weather conditions. However, this assumption does not hold for the BSN area.

The solar energy harvesting in BSN area usually includes both indoor and outdoor environment. The indoor lighting level is more human controlled and affected by human motion. Compared with

outdoor, the lighting in the indoor environment like in an office, hospital, gymnasium, and classroom is almost stable regardless of time, except locations close to a window. However, the solar harvesters deployed on the human body are affected by human motion, and the harvested energy could fluctuate considerably. Prediction of indoor solar energy harvesting usually utilizes the general time-series prediction methods. The transition of indoor and outdoor is also complex to model and predict.

Besides, the dimensions of the harvesters and related circuits are limited compromising for wearability, and the harvested energy is much less than other WSN applications.

Due to the differences in BSN energy harvesting, the methodologies mentioned above cannot be directly employed. For instance, the EWMA including weather conditioned models would fail without distinguishing the indoor and outdoor environment. Therefore, inspired these models, we proposed a context-aware hybrid model for indoor and outdoor energy harvesting prediction.

## **4.2 A Hybrid Context-Aware Profile Based Model**

The context has different scopes in different areas, and in energy harvesting prediction area we limit the context to be the information collected by the sensor system or the smartphone which are related to energy harvesting prediction. We will discuss our custom Self-power Context-aware DPM (SCDPM) platform in Section 6, and the context discussion is based on the sensing capability of SCDPM.

### **4.2.1 The Scope of Context**

The target of employing context information is to leverage as much as possible the available knowledge of the current situation and thus to execute appropriate prediction models for accurate prediction. As discussed before, the solar energy harvesting in BSN area usually includes both indoor and outdoor environment which has distinct behavior. Therefore, an essential task is to try

to predict the indoor/outdoor environment. Here are the context information sources that we employ in the model.

**Weather Forecast Information.** In our work, since we are using a smartphone, the weather forecast could be acquired very conveniently. We can get the hourly weather information in real time from the internet. Therefore, the similarity is not required, and we can have a more accurate weather classification rather than just cloud or sunny days as discussed in [64].

**Calendar Events.** Calendar events  $C$  could be used to predict the user's behavior especially for predicting indoor or outdoor environment, and the specific indoor locations. Here we assume that we could directly extract the place name from an event description. For instance, "Gym", "UVA Hospital", "Rice Hall 304", "Home", etc. Extracting such information from a complex sentence may require natural language processing related methods, and they are out of the scope of this work. The light profiles for each place is maintained and could be employed to predict indoor energy harvesting.

**GPS.** The GPS denoted by  $G$  provides information of the place, and the moving speed of the user as well. The place information could be used with the calendar information to decide the indoor/outdoor situation and places.

#### 4.2.2 Profiles

Inspired by the EWMA and profile-based models, we also maintain a typical profile  $E_i^P$ . In addition, we keep the statistics on the lighting conditions and temperature of indoor locations. The statistics of the mean and variance of the light intensity and temperature are stored. Such information is maintained in a matrix of  $[L_1, L_2, \dots, L_M]$  for  $M$  indoor locations. Examples include gym, classroom, restaurant, home, etc. The location could be co-decided by GPS and calendar events.

In order to utilize the weather forecast, a parameter list is used to describe the relationship between each weather condition and the maximum light intensity (also the maximum solar energy). Such a parameter list  $[W_1, W_2, \dots, W_K]$  is in a range  $(0, 1]$ , 1 for sunny and smaller values for cloudy or rainy, foggy. The harvested solar energy under a specific weather condition is predicted by multiplying the  $W_i$  to the maximum harvested energy in a sunny day. Such a parameter list is calculated for our SCDPM platform as shown in Section 7.3.

The parameters for the indoor locations and weather sets could be updated, but we first ignore it and use stationary parameter data sets.

### 4.2.3 Context-Aware Hybrid Models

Hybrid models are used to predict the different time horizons and indoor/outdoor situations. Here the minimum time slot that we select is 30 seconds. The indoor energy harvesting prediction based on the  $[L_1, L_2, \dots, L_M]$ , and the outdoor solar energy harvesting relies on the weather forecast information. The context information including calendar events and GPS are employed to predict the location.

**Medium-term and long-term prediction.** We use the weather forecast and profiles for medium-term and long-term prediction with the range from 30 minutes to several hours. Longer time horizon more than a day is not considered. A time slot of 30 minutes as in EWMA-based and profile-based modes is selected for such horizon.

$$\hat{E}_t = \alpha E_{t-1} + (1 - \alpha) f(E_t^P, L_t, W_t, C, G) \quad (4.1)$$

If there isn't any context information to decide the indoor/outdoor situation, then the model is degraded to the EWMA based models as shown in (4.2). The profiles are used for medium-term and long-term prediction.

$$\hat{E}_t = \alpha E_{t-1} + (1 - \alpha) E_t^P \quad (4.2)$$

If there is context information at the  $t$ th time slot, the model could be improved without using  $E_t^P$ . If the current time slot is indoor and the location is  $m$ th in  $[L_1, L_2, \dots, L_M]$ , then:

$$\hat{E}_{Indoor} = g_{in}(L_m) \quad (4.3)$$

If the current time is outdoor with the weather condition  $k$  in  $[W_1, W_2, \dots, W_K]$ , then:

$$\hat{E}_{Outdoor} = g_{out}(W_k) \quad (4.4)$$

Therefore, based on the context information,

$$\begin{aligned} \hat{E}_t &= \alpha E_{t-1} + (1 - \alpha) E_t^P, \text{ if no context information, or} \\ \hat{E}_t &= \alpha E_{t-1} + (1 - \alpha) \hat{E}_{Indoor}, \text{ for an indoor situation, or} \\ \hat{E}_t &= \alpha E_{t-1} + (1 - \alpha) \hat{E}_{Outdoor}, \text{ for an outdoor situation} \end{aligned} \quad (4.5)$$

**Short-term prediction.** A time slot of 30 seconds is selected for short-term prediction inside the 30 minutes slots. As discussed in 4.1.3 and 4.1.5, we use exponential smoothing from the empirical models for short-term prediction with the range from 30 seconds to 30 minutes.

### 4.3 Summary

In this chapter, solar and thermoelectric energy harvesting prediction methods were studied and these methods cannot directly apply in self-powered BSN systems regarding human behavior effect and prediction horizon. Based on these previous work, a hybrid context-aware prediction model for both indoor and outdoor environment is proposed utilizing weather forecast information, calendar, and GPS to improve the performance of prediction accuracy and horizon.

The proposed model is more like a framework to demonstrate the idea of utilizing context information rather than a concrete model or algorithm. For instance, there are different ways to use GPS and calendar events, and we assume that the calendar events could directly provide the energy harvesting information. The scope of context could be extended as well.

Unlike outdoor solar energy harvesting research, there aren't any databases for the hybrid indoor and outdoor solar energy harvesting with our required information. Thus, the performance is hard to validate or compare, and it highly depends on the experiment platform and conditions. In order to try to prove the effectiveness of our proposed model, we test it on our custom SCDPM platform which will be discussed in Section 6. The experiments and results are presented in Section 7.3 as part of the validation of the SCDPM platform.

# 5 Dynamic Power Management Optimization

Dynamic Power Management (DPM) is a design and operating methodology for reconfiguring systems dynamically to provide specific services and performance with some of the components shutting down or in a low power state when inactive. DPM has been widely adopted in systems design [65]–[73], portable and embedded electrical design[74]–[77], high performance computing clusters[78]–[80], electrical vehicles[81], and wireless sensor networks[82]–[85]. There are two fundamental assumptions for the applicability of DPM: a) the workload of the system could fluctuate during operation time; and b) it is possible to observe and predict the workload change[65]. The system, which usually consists of heterogeneous power-manageable components, could then be managed to achieve a better power efficiency with specific DPM policies.

In the area of self-powered BSN, the fluctuation of available energy is a critical concern in addition to the workload change. As stated before, the harvested energy from solar, thermoelectric, and other sources in the real world is discontinuous, which is different from the stable power supply like batteries. Therefore, DPM in self-powered BSN should consider the dynamics of both energy harvesting and workload during operation time. On the workload side, the power consumption of most power manageable components at different operating conditions could be modeled. In the next section, such a power consumption model is discussed for the proposed

SCDPM platform. On the energy harvesting side, the harvested energy could be predicted. As discussed in the previous section, we developed the hybrid context-aware model for indoor and outdoor solar energy harvesting prediction.

In order to optimize the data quality in an energy harvesting sensor system, a context-aware dynamic power management framework is proposed. The fundamental idea is to take advantage of context information from the smartphone and the system nodes for energy harvesting prediction and power management. The context-based energy harvesting prediction was discussed in the last chapter.

In this section, firstly the proposed context-aware dynamic power management framework for an energy harvesting sensor system is presented in Section 5.1. The framework mainly includes a scheduling module and an energy harvesting predictor. In the following part, the power management is discussed from the perspective of nonlinear convex optimization. In Section 5.2, the optimization model of the power management in the energy harvesting system is formally constructed, and the optimal offline solution is derived. In Section 5.3, the constraint of the supercapacitor capacity is added to the problem, and the updated optimal solution is derived. Then the online scheduling problem is discussed in Section 5.4. Simulations of the power management using an energy profile collected in the real world are presented in each subsection.

The cost function of the optimization in the real world is difficult to find. In general, the cost function is related to the specific applications. To explore this issue, we studied the vigilant Atrial Fibrillation (AFib) monitoring as a case study. In this application, the AFib detection performance is the most concerned by the medical area. Therefore, the relationship between the power consumption and the AFib detection performance is explored. We proved that our cost function

could be extended and is practical and meaningful in the real medical applications and the proposed solution remains valid.

A preliminary result of this section (Section 5.2, 5.3, 5.6) was published in [86].

## 5.1 Context-Aware Dynamic Power Management Framework

The conceptual diagram of a general system level DPM scheduling is shown in Figure 5.1 which is adapted from [65]. The sensing modules work as an observer to collect information on the workload and harvested energy. The controller receives information, executes power management scheduling algorithms, and then sends commands to the system to dynamically reconfigure the system.

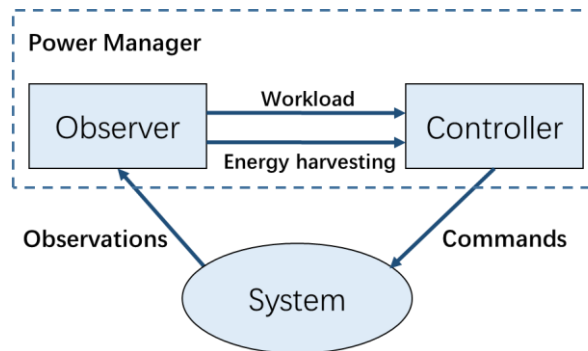


**Figure 5.1 Abstract diagram of system-level dynamic power management.**

The configuration parameters determine the system power consumption and data quality. The parameters mainly include the sampling rate, the number of enabled environmental sensors, data delay, radio power, and sleep mode configurations. By changing those parameters separately or collaboratively, the power consumption and data quality could be changed almost continuously. Since there is a tradeoff between the power consumption and data quality, the target of the dynamic power management is to optimize the data quality within a power budget and an operation time requirement.

A context-aware dynamic power management framework is proposed as illustrated in Figure 5.2 to achieve this goal. Consider a typical energy-harvesting body sensor system communicating with a phone. The sensor node collects sensor data and transmits it to the power manager which runs on the phone. The power manager includes an energy predictor and an online scheduler. The energy predictor receives sensor data and collects context data from the phone and combines them to make a prediction of harvested energy in future time slots. Then the prediction result is sent to the scheduler to make a decision of the optimal parameter set. The sensor node receives the updated parameter set and changes them accordingly.

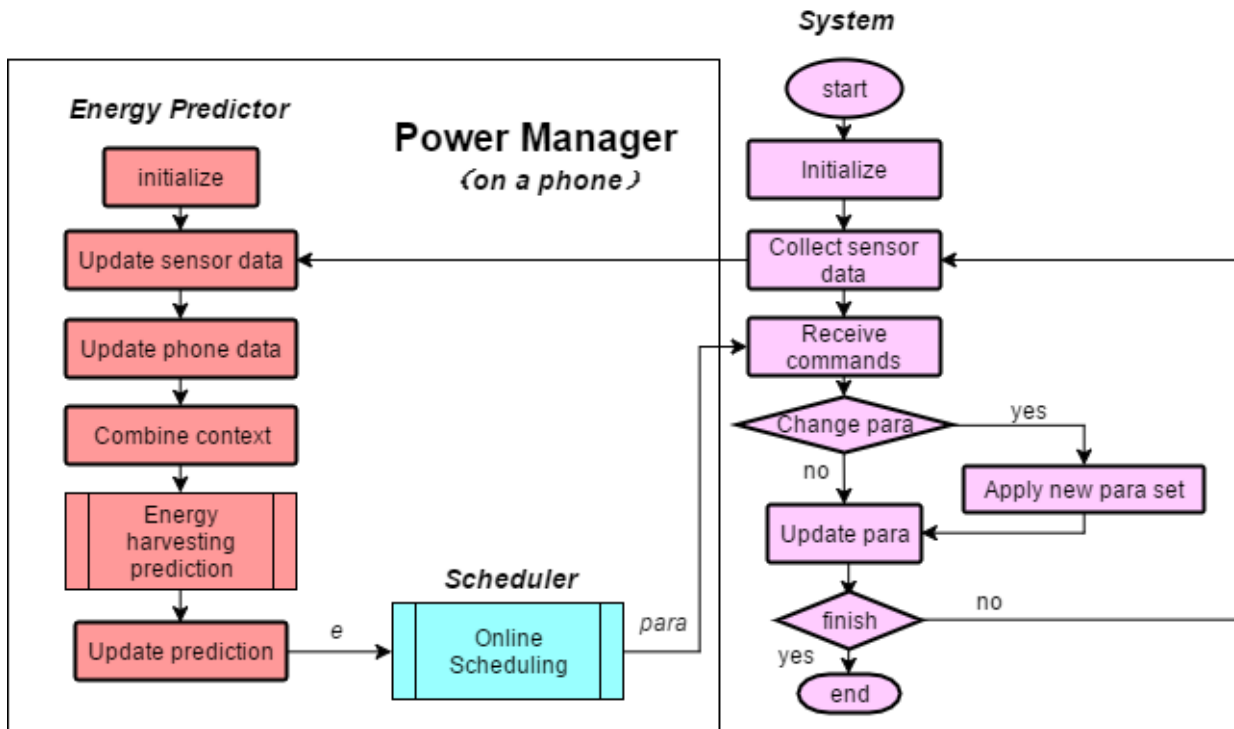


**Figure 5.2 The workflow for the proposed context-aware dynamic power management framework. The sensor system communicates with a phone which runs the power management algorithm.**

As shown in Figure 5.2, there are two modules in the power manager, an energy predictor, and a scheduler. For the energy predictor, the hybrid context-aware model is developed as discussed in the last chapter. For the scheduler, we will focus on it in this chapter. A formal analysis of the

model will be provided, and the optimal scheduling algorithm will be derived in the following sections.

## 5.2 A DPM Scheduling Model for Energy Harvesting Sensor System

The power management problem could be modeled as a mathematical optimization problem: deciding the energy consumption in each time interval to minimize the total cost or maximize the objective function. To compare the cost, we define a limited time range and minimize the overall cost function during this time. Consider an energy harvesting sensor system which is required to run from  $1$ st to  $N$ th discrete time unit. The harvested energy in each time slot is given as:

$$e = [e_1, e_2, \dots, e_N]^T \quad (5.1)$$

The initial energy in a battery or a supercapacitor is included in the  $e_1$ .

The variable  $x$  is the energy consumption during these time slots and we assume the power management is continuous.

$$x = [x_1, x_2, \dots, x_N]^T \quad (5.2)$$

A cost function is required to be defined regarding  $x$ . The object in general is to maximize the overall “data quality” of the sensor system during a predefined operating period. The data quality or the target is closely related to the system power consumption and they are usually positively correlated. In the Section 6.4, we will use our SCDPM system as an example to prove that the system power consumption is positively correlated to the sensors sampling rate in a duty-cycled system. In most cases, the data quality of a sensing system increases with a higher sampling rate of the sensors. Intuitively, when increasing the sampling rate or operating speed, the power consumption will be higher, and then we will have the more detailed information of the signal of interest and the data quality is better. When the system is down the signal is lost then the penalty should be significantly high.

In a comprehensive paper about power management in energy harvesting systems [58], the authors assumed a linear relationship between power consumption and utility with thresholds. Power consumption smaller than the low threshold will lead to zero utility, and more than the high threshold will not increase the utility. This linear model could represent some use cases. However, the relationship between the utility or cost and the power consumption could present nonlinearity even inside the two thresholds. For instance, when the power consumption is low, increasing a little will improve the data quality a lot. As the sampling rate and power consumption are increasing, the power increment will bring less data quality improvement. In the Section 5.6.4, we analyzed the AFib application in which the relationship between utility/cost and power consumption cannot be modeled with a linear function.

In reality, the cost function depends on the specific medical applications, and it is impractical to give a universal form. Considering the properties discussed above, here we consider a cost function form during the entire operation period as shown in (5.3). Such a form can represent the fundamental relationship between power consumption and the data quality for most applications. The basic idea of this form is that evenly data sampling is preferred than unevenly. The benefit of this form is that it is smooth and the derivative is concise. In Section 5.6, we will study the vigilant Atrial Fibrillation (AFib) monitoring as a case study and discuss the application specific cost function for this application in Section 5.6.4. We will prove that the optimal solution remains the same even the cost function is different from (5.3).

$$J = \sum_{i=1}^N \frac{1}{x_i} \quad (5.3)$$

The constraint is in each time slot the consumed power is no higher than available energy (remaining energy plus harvested energy in the current time slot). Assuming  $e_i$  is positive, which

means that energy could be always harvested in each slot even though it might be arbitrarily small.

The  $N$  inequalities are:

$$\begin{aligned}
 x_1 &\leq e_1 \\
 x_1 + x_2 &\leq e_1 + e_2 \\
 &\dots \\
 x_1 + x_2 + \dots + x_N &\leq e_1 + e_2 + \dots + e_N
 \end{aligned} \tag{5.4}$$

Define  $g_k(x)$  to represent the  $N$  inequalities:

$$g_k(x) = \sum_{i=1}^k x_i - \sum_{i=1}^k e_i \quad (k = 1, 2, \dots, N) \tag{5.5}$$

The formal optimization problem could be written as:

Minimize:

$$f(x) = \sum_{i=1}^N \frac{1}{x_i} \tag{5.6}$$

Subject to:

$$g_k(x) \leq 0 \quad (k = 1, 2, \dots, N) \tag{5.7}$$

$$x_i > 0, e_i > 0 \quad (i = 1, 2, \dots, N) \tag{5.8}$$

### 5.3 Optimal Solution

In this section, we first consider the optimal offline solution which assuming that we have all the information on harvested energy during each time slot. In other words, the  $e$  is given in advance.

The problem is an optimization problem with only inequalities [87]. All the constraint functions are linear, but the objective function is nonlinear:

For the constraint functions:

$$\alpha \sum_{i=1}^k x_i + \beta \sum_{i=1}^k y_i = \sum_{i=1}^k (\alpha x_i + \beta y_i) \quad (5.9)$$

For the objective function:

$$f(\alpha x + \beta y) = \sum_{i=1}^N \frac{1}{\alpha x_i + \beta y_i} \quad (5.10)$$

$$\alpha f(x) + \beta f(y) = \alpha \sum_{i=1}^N \frac{1}{x_i} + \beta \sum_{i=1}^N \frac{1}{y_i} = \sum_{i=1}^N \frac{\alpha y_i + \beta x_i}{x_i y_i} \quad (5.11)$$

There exist  $\alpha, \beta$  that:

$$f_k(\alpha x + \beta y) \neq \alpha f_k(x) + \beta f_k(y) \quad (5.12)$$

Therefore, the problem is nonlinear. Now consider if the problem is convex.

For the constraint functions:

$$\alpha \geq 0, \beta \geq 0, \alpha + \beta = 1 \quad (5.13)$$

$$g_k(\alpha x + \beta y) = \sum_{i=1}^k (\alpha x_i + \beta y_i) - \sum_{i=1}^k e_i \quad (5.14)$$

$$\begin{aligned} \alpha g_k(x) + \beta g_k(y) &= \alpha \sum_{i=1}^k x_i + \beta \sum_{i=1}^k y_i - \sum_{i=1}^k e_i = \sum_{i=1}^k (\alpha x_i + \beta y_i) - \sum_{i=1}^k e_i \\ &= g_k(\alpha x + \beta y) \end{aligned} \quad (5.15)$$

For the objective function:

$$\alpha \geq 0, \beta \geq 0, \alpha + \beta = 1 \quad (5.16)$$

$$f(\alpha x + \beta y) = \sum_{i=1}^N \frac{1}{\alpha x_i + \beta y_i} \quad (5.17)$$

$$\alpha f(x) + \beta f(y) = \alpha \sum_{i=1}^N \frac{1}{x_i} + \beta \sum_{i=1}^N \frac{1}{y_i} \quad (5.18)$$

$$f(\alpha x + \beta y) - (\alpha f(x) + \beta f(y)) \quad (5.19)$$

$$\begin{aligned} &= - \sum_{i=1}^N \frac{\alpha\beta x_i^2 + \alpha\beta x_i^2 + (\alpha^2 + \beta^2 - 1)x_i y_i}{(\alpha x_i + \beta y_i)x_i y_i} \\ &= - \sum_{i=1}^N \frac{\alpha\beta x_i^2 + \alpha\beta x_i^2 - 2\alpha\beta x_i y_i}{(\alpha x_i + \beta y_i)x_i y_i} \\ &= -\alpha\beta \sum_{i=1}^N \frac{(x_i - y_i)^2}{(\alpha x_i + \beta y_i)x_i y_i} \leq 0 \end{aligned}$$

Therefore, all constraint functions and the objective function are convex, and thus the problem is a convex optimization problem. For such optimization problems, a fundamental property is that all locally optimal points are globally optimal points [87].

Define the Lagrangian expression  $L(x, \lambda)$  with the Lagrange multiplier vector  $\lambda$ :

$$L(x, \lambda) = f(x) + \sum_{i=1}^N \lambda_i g_i(x), \quad \lambda_i \geq 0, \text{ for } i = 1, 2, \dots, N \quad (5.20)$$

Since the optimization problem is convex as proved before, the necessary Karush–Kuhn–Tucker (KKT) conditions are also sufficient for the points to be primal and dual optimal. The KKT conditions are listed as below:

$$g_i(x) \leq 0 \quad (5.21)$$

$$\lambda_i g_i(x) = 0 \quad (5.22)$$

$$\frac{\partial}{\partial x} L(x, \lambda) = 0 \quad (5.23)$$

Equation (5.23) indicates that:

$$\frac{1}{x_i^2} = \sum_{k=i}^N \lambda_k \quad (5.24)$$

$$\lambda_i = \frac{1}{x_i^2} - \frac{1}{x_{i+1}^2} \quad (i = 1, 2, \dots, N - 1) \quad (5.25)$$

$$\lambda_N = \frac{1}{x_N^2} \quad (5.26)$$

Since  $\lambda_i \geq 0$ :

$$x_i \leq x_{i+1} \quad (5.27)$$

$$\sum_{i=1}^N x_i = \sum_{i=1}^N e_i \quad (5.28)$$

$$\lambda_i \left( \sum_{i=1}^k x_i - \sum_{i=1}^k e_i \right) = 0 \quad (5.29)$$

The  $x$  is nondecreasing during all time intervals. There are two trivial solutions. If  $e$  is non-decreasing, then  $x_i = e_i$ . If  $e$  is non-increasing, then  $x_i = \text{average}(e)$ .

For general cases, we consider the sequence  $PE_k$ .

$$PE_k = \frac{\sum_{i=1}^k e_i}{k} \quad (1 \leq k \leq N) \quad (5.30)$$

Since  $x_i$  is non-decreasing, for the  $k$ th equation:

$$x_1 k \leq \sum_{i=1}^k x_i \leq \sum_{i=1}^k e_i \quad (5.31)$$

$$x_1 \leq PE_k \quad (1 \leq k \leq N) \quad (5.32)$$

Find:

$$k^* = \operatorname{argmin}_{1 \leq k \leq N} (PE_k) \quad (5.33)$$

Then:

$$x_1 \leq PE_{k^*} \quad (5.34)$$

Assign  $x_1 = PE_{k^*}$  and this is the optimal solution for  $x_1$ . Besides,

$$x_1, x_2, \dots, x_{k^*} = PE_{k^*} \quad (5.35)$$

The  $k^*$ th inequality is active and  $g_i(x) = 0$ .

If  $x_1$  is reduced to be  $x_{1'} = PE_{k^*} - \varepsilon > 0 (\varepsilon > 0)$ , then one or more  $x_k (1 < k \leq k^*)$  could be increased to reduce the cost. Suppose  $x_{b'} (1 < b \leq k^*)$  is increased to  $x_{b'} = PE_{k^*} + \varepsilon$ , then the total cost will be increased due to the change:

$$\begin{aligned} \Delta f(x) &= \left( \frac{1}{x_{b'}} + \frac{1}{x_{1'}} \right) - \left( \frac{1}{x_b} + \frac{1}{x_1} \right) = \frac{1}{PE_{k^*} - \varepsilon} + \frac{1}{PE_{k^*} + \varepsilon} - \frac{2}{PE_{k^*}} \\ &= \frac{2\varepsilon^2}{(PE_{k^*} - \varepsilon)(PE_{k^*} + \varepsilon)PE_{k^*}} > 0 \end{aligned} \quad (5.36)$$

Therefore,  $x_1, x_2, \dots, x_{k^*} = PE_{k^*}$  is the optimal solution for the first  $k^*$  elements. If  $k^* < N$ , then start from  $k^* + 1$  to continue to calculate until the end. In general, when start from *begin* ( $1 \leq \text{begin} \leq N$ ), let:

$$PE_k = \frac{\sum_{i=1}^k e_i - \sum_{i=1}^{\text{begin}-1} x_i}{k - \text{begin} + 1}, \quad (\text{begin} \leq k \leq N) \quad (5.37)$$

$$k^* = \operatorname{argmin}_{\text{begin} \leq k \leq N} (PE_k) \quad (5.38)$$

Then:

$$x_{\text{from}}, x_{\text{from}+1}, \dots, x_{k^*} = PE_{k^*} \quad (5.39)$$

The end case is:

$$x_N = \sum_{i=1}^N e_i - \sum_{i=1}^{N-1} x_i \quad (5.40)$$

The algorithm could be summarized in the following table. The worst-case complexity of the algorithm is  $O(N^2)$ .

---

**ALGORITHM 5.1**

---

1: **Input:**  $e = [e_1, e_2, \dots, e_N]^T$  for harvested energy in each time slot, and  $N$  for the number time slots  
2:  $J = \sum_{i=1}^N \frac{1}{x_i}$  as the cost function of data quality  
3: **Output:**  $x$ , energy consumption in each time slot to minimize the cost  
4:  $x = []$   
5: **while**  $1 \leq i \leq N$  **do**  
6:      $min = \text{infinity}$   
7:      $k^* = i$   
8:     **for** each  $j$  in  $\{i, i+1, \dots, N\}$  **do**  
9:          $min = \text{Min}(min, \frac{\sum_{k=1}^j e_k - \sum_{k=1}^{i-1} x_k}{j-i+1})$   
10:          $k^* = j$   
11:     **end for**  
12:     assign  $x_i, x_{i+1}, \dots, x_{k^*} = min$   
13: **end while**  
14: **return**  $x = [x_1, x_2, \dots, x_N]^T$

---

Here is a simulation of the offline algorithm illustrated in Figure 5.3. The energy profile for around 6 hours was collected by the EHDC platform. The proposed algorithm is compared with the stoplight algorithm and a greedy algorithm ( $x_i=e_i$ ). The cost of the proposed optimal solution and the greedy algorithm is 1846.9 and 1436.4, respectively. For the stoplight algorithm, the consumption depends only on current remained energy and predefined thresholds. The operating modes might oscillate even using hysteretic thresholds. In the simulation, three operation modes are used. Since the stoplight algorithm encounters powering down as shown in the figure, the total cost is infinity.

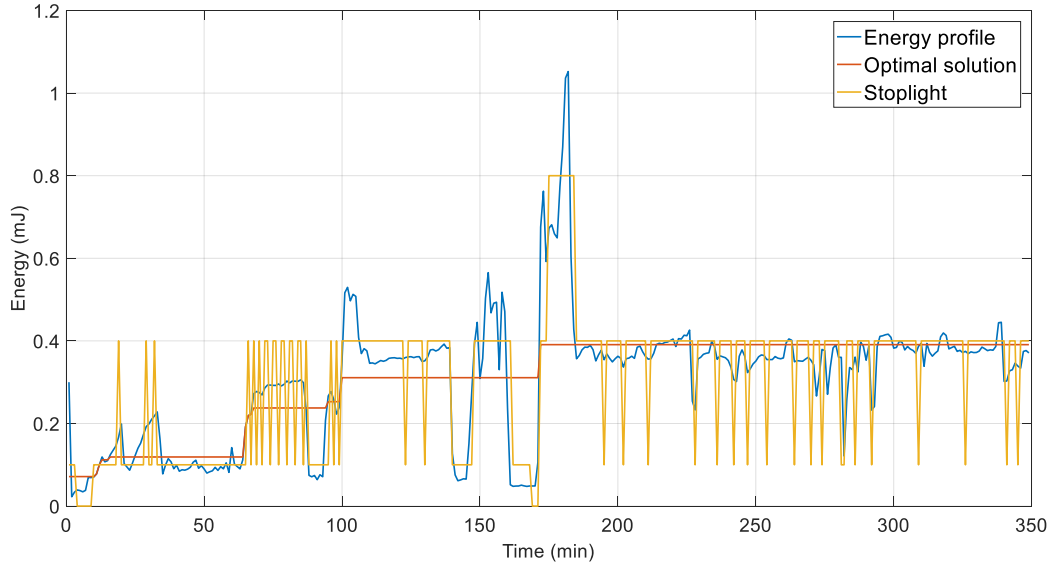


**Figure 5.3 Simulation of DPM strategies on an energy profile. The cost of the proposed algorithm (offline solution) and the greedy algorithm is 1436.4, 1846.9 respectively. The stoplight algorithm encounters powering down.**

## 5.4 DPM Model with Battery Capacity Limit

The battery of the energy harvesting systems is limited and, in some cases, the battery cannot store all harvested energy. For instance, in the outdoor environment when it is sunny, the solar energy is abundant, and the supercapacitor can be fully charged in a short time and cannot store additional energy.

Suppose the maximum capacity of a supercapacitor is  $C$  ( $C > 0$ ), the  $2N$  constraints are:

$$\sum_{i=1}^k x_i \leq \sum_{i=1}^k e_i \quad (k = 1, 2, \dots, N) \quad (5.41)$$

$$\sum_{i=1}^k x_i \geq \sum_{i=1}^k e_i - C \quad (k = 1, 2, \dots, N) \quad (5.42)$$

Similar to the previous solution, define:

$$h_k(x) = -C - \sum_{i=1}^k x_i + \sum_{i=1}^k e_i \quad (k = 1, 2, \dots, N) \quad (5.43)$$

Then the optimization model with a capacity limit could be expressed as the following.

Minimize:

$$f(x) = \sum_{i=1}^N \frac{1}{x_i} \quad (5.44)$$

Subject to:

$$g_k(x) \leq 0 \quad (k = 1, 2, \dots, N) \quad (5.45)$$

$$h_k(x) \leq 0 \quad (k = 1, 2, \dots, N) \quad (5.46)$$

$$x_i > 0, e_i > 0 \quad (i = 1, 2, \dots, N) \quad (5.47)$$

For the newly added  $N$  constraint functions:

$$\alpha \geq 0, \beta \geq 0, \alpha + \beta = 1 \quad (5.48)$$

$$h_k(\alpha x + \beta y) = -C - \sum_{i=1}^k (\alpha x_i + \beta y_i) + \sum_{i=1}^k e_i \quad (5.49)$$

$$\alpha h_k(x) + \beta h_k(y) = -C - \alpha \sum_{i=1}^k x_i - \beta \sum_{i=1}^k y_i + \sum_{i=1}^k e_i \quad (5.50)$$

$$= -C - \sum_{i=1}^k (\alpha x_i + \beta y_i) + \sum_{i=1}^k e_i = h_k(\alpha x + \beta y)$$

Therefore, it is still a convex optimization problem. Define the Lagrangian expression as:

$$L(x, \lambda, \mu) = f(x) + \lambda g(x) + \mu h(x) \quad (5.51)$$

$$L(x, \lambda, \mu) = f(x) + \sum_{i=1}^N \lambda_i g_i(x) + \sum_{i=1}^N \mu_i h_i(x), \quad \lambda_i \geq 0, \mu_i \geq 0, \text{ for } i \quad (5.52)$$

$$= 1, 2, \dots, N$$

The KKT conditions are:

$$g_i(x) \leq 0 \quad (5.53)$$

$$\lambda_i g_i(x) = 0 \quad (5.54)$$

$$h_i(x) \leq 0 \quad (5.55)$$

$$\mu_i h_i(x) = 0 \quad (5.56)$$

$$\frac{\partial}{\partial x} L(x, \lambda, \mu) = 0 \quad (5.57)$$

That is:

$$\lambda_i - \mu_i = \frac{1}{x_i^2} - \frac{1}{x_{i+1}^2} \quad (i = 1, 2, \dots, N - 1) \quad (5.58)$$

$$\lambda_N - \mu_N = \frac{1}{x_N^2} \quad (i = N) \quad (5.59)$$

$$\lambda_i \left( \sum_{i=1}^k x_i - \sum_{i=1}^k e_i \right) = 0 \quad (5.60)$$

$$\mu_i \left( -C - \sum_{i=1}^k x_i + \sum_{i=1}^k e_i \right) = 0 \quad (5.61)$$

For the capacity limit  $C$ , if  $C$  is large enough, then  $(-C - \sum_{i=1}^k x_i + \sum_{i=1}^k e_i) > 0$  for all  $N$  inequalities, and all  $\mu_i$  should be zero and the solution is the same with the previous no-capacity-limit scenario. If  $C=0$ , the solution is trivial:  $x_i = e_i$  as the greedy algorithm. When given the  $e$ , the cost should be nonincreasing along with  $C$ .

Since  $\lambda_N - \mu_N = \frac{1}{x_N^2}$ ,  $\lambda_N > 0$ . Then  $\sum_{i=1}^k x_i - \sum_{i=1}^k e_i = 0$ , which means all the energy should be consumed at the last time interval. If  $x_i \neq x_{i+1}$ , then either  $\sum_{i=1}^k x_i - \sum_{i=1}^k e_i = 0$  or  $-C - \sum_{i=1}^k x_i + \sum_{i=1}^k e_i = 0$ , which means the battery should be either empty or full.

Compared with the no-capacity-limit solution, here we consider the two sequences.

$$PE_k = \frac{\sum_{i=1}^k e_i}{k} \quad (1 \leq k \leq N) \quad (5.62)$$

$$PF_k = \frac{\sum_{i=1}^k e_i - C}{k} \quad (1 \leq k \leq N) \quad (5.63)$$

The  $PE_k$  sequence relates to points that satisfy  $g_i(x) = 0$  and  $PF_k$  relates to  $h_i(x) = 0$ . Starting from previous non-capacity-limit scenario to calculate  $k^*$  from equation (12) and assign  $x_1, x_2, \dots, x_{k^*} = PE_{k^*}$ . When adding the capacity constraint, if the battery doesn't saturate before  $k^*$ , then the solution remains unchanged. If the battery saturates or overflows before the  $k^*$ th point and assume the battery saturates or overflows at the  $j$ th point ( $j < k^*$ ) for the first time, then  $x_{j+1}$  will be less than  $PE_k$  since there isn't enough remaining from the previous time slot due to the capacity limit. Let  $x_{j+1} = PE_{k^*} - \varepsilon$ , then the  $x_j$  could be relaxed to  $x_j = PE_{k^*} + \varepsilon$ , and the total cost increases.

To deal with the capacity limit constraint, we consider the points that satisfy  $h_i(x) = 0$  in addition to points that satisfy  $g_i(x) = 0$  in the previous solution. Specifically,

1) Search the next minimum  $PE_i$ . If the supercapacitor full doesn't happen before  $i$ , then repeat 1) to search forward.

2) If supercapacitor full happens before  $i$  ( $PE_i < \max_{1 \leq p \leq i}(PF_p)$ ), then search backward from  $i$  to find the maximum  $PF_j$ . If supercapacitor empty doesn't happen before  $j$  then repeat 1) from  $(j+1)$ , else execute 3).

3) If supercapacitor empty happens before  $j$  ( $PF_j > \min_{1 \leq p \leq j}(PE_p)$ ), then search backward from  $j$  to find the minimum  $PE_l$ . If supercapacitor full doesn't happen before  $l$  then repeat 1) from  $(l+1)$ , else repeat 2).

Repeat until the entire array is processed. Note that  $i = 1$  satisfies both 2) and 3) since  $PE_1 \leq PF_1$ , so the solution exists.

There are two cases when condition 2) or 3) is satisfied. First, the supercapacitor is empty at the  $k$ th point:

$$x_{from \sim k} = PE_k \quad (5.64)$$

$$PE_k = \min_{from \leq i \leq k}(PE_i) \quad (5.65)$$

$$PE_k \geq \max_{from \leq i \leq k}(PF_i) \quad (5.66)$$

Moreover, the second, the supercapacitor is full at the  $k$ th point:

$$x_{from \sim k} = PF_k \quad (5.67)$$

$$PF_k = \max_{from \leq i \leq k}(PF_i) \quad (5.68)$$

$$PF_k \leq \min_{from \leq i \leq k}(PE_i) \quad (5.69)$$

For the first case:

Since  $PE_k = \min_{1 \leq i \leq k}(PE_i)$ , so:

$$\sum_{i=1}^j x_j = jPE_k \leq jPE_j = j \frac{\sum_{i=1}^j e_i}{j} = \sum_{i=1}^j e_i \quad (5.70)$$

Since  $PE_k \geq \max_{1 \leq i \leq k}(PF_i)$ ,

$$\sum_{i=1}^j x_i = jPE_k \geq jPF_i = j \frac{\sum_{i=1}^j e_i - C}{j} = \sum_{i=1}^j e_i - C \quad (5.71)$$

All inequalities are satisfied and the second case is similar to prove. The algorithm is summarized in the following table.

---

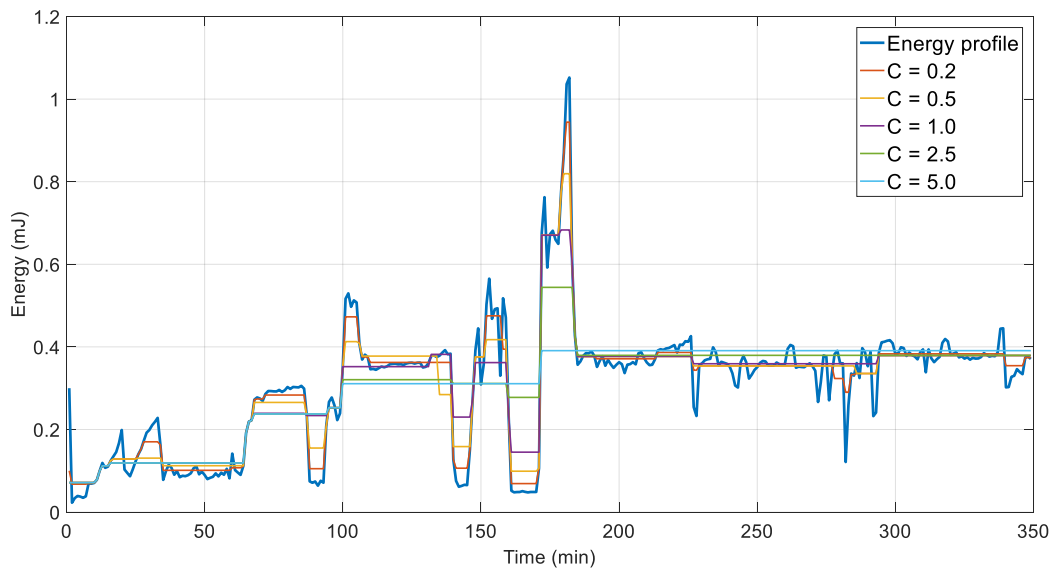
**ALGORITHM 5.2:**

---

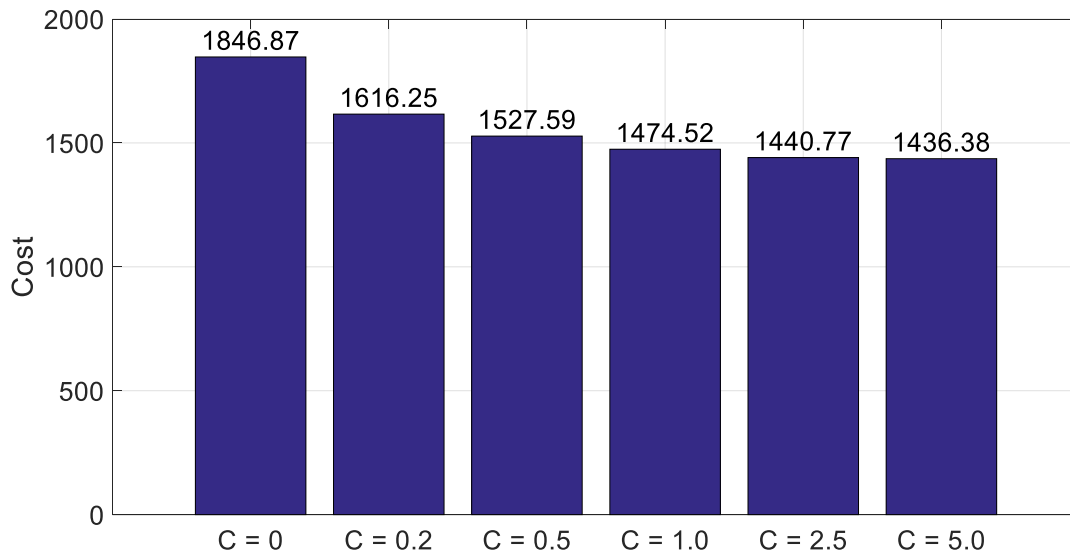
- 1: **Input:**  $e = [e_1, e_2, \dots, e_N]^T$  for harvested energy in each time slot,  $N$  for the number time slots, and  $C$  for the capacity of the battery
  - 2:  $J = \sum_{i=1}^N \frac{1}{x_i}$  as the cost function of data quality
  - 3: **Output:**  $x$ , energy consumption in each time slot to minimize the cost
  - 4:  $x = []$
  - 5:  $start = 1$
  - 6: **while**  $start \leq N$  **do**
  - 7:  $j = \operatorname{argmin}_k \left( \frac{\sum_{i=1}^j e_i - \sum_{i=1}^{start-1} x_i}{j - start + 1} \right)$
  - 8:  $PE_l = \frac{\sum_{i=1}^l e_i - \sum_{i=1}^{start-1} x_i}{l - start + 1} \quad (start \leq l \leq j)$
  - 9:  $PF_l = \frac{\sum_{i=1}^l e_i - \sum_{i=1}^{start-1} x_i - C}{l - start + 1} \quad (start \leq l \leq j)$
  - 10:  $end = \max(k)$  s.t.:
  - 11:  $g_k(x) = 0$  (1) or  $h_k(x) = 0$  (2)
  - 12: assign  $x_{start}, x_{start+1}, \dots, x_{end} = PE_k$  for (1) or
  - 13: assign  $x_{start}, x_{start+1}, \dots, x_{end} = PF_k$  for (2)
  - 14:  $start = end + 1$
  - 15: **end while**
  - 16: **return**  $x = [x_1, x_2, \dots, x_N]^T$
- 

Note that it is required to compare  $PE_{end}$  and  $PE_{end+1}$  to decide empty ( $PE_{end} < PE_{end+1}$ ) or full status ( $PE_{end} > PE_{end+1}$ ) at the  $end$ th point in addition to check (5.65)(5.66)(5.68)(5.69). Besides, when  $end = N$ , the supercapacitor should be empty, as proved before.

Here are simulations of calculated  $x$  regarding different  $C$  values (the unit is mJ in the simulations) using the same energy profile as in Section 5.3. Figure 5.4 illustrates the consumed energy in each time interval at different capacity values. With smaller  $C$  values, the  $x$  is closer to  $e$  since the supercapacitor cannot store much energy, so it tends to use up available energy in the current time interval. When  $C$  is large enough, the optimal solution is the same as the no-capacity-limit scenario, as shown by the cyan curve of  $C = 5.0$  in Figure 5.4. The cost of each case is shown in Figure 5.5.



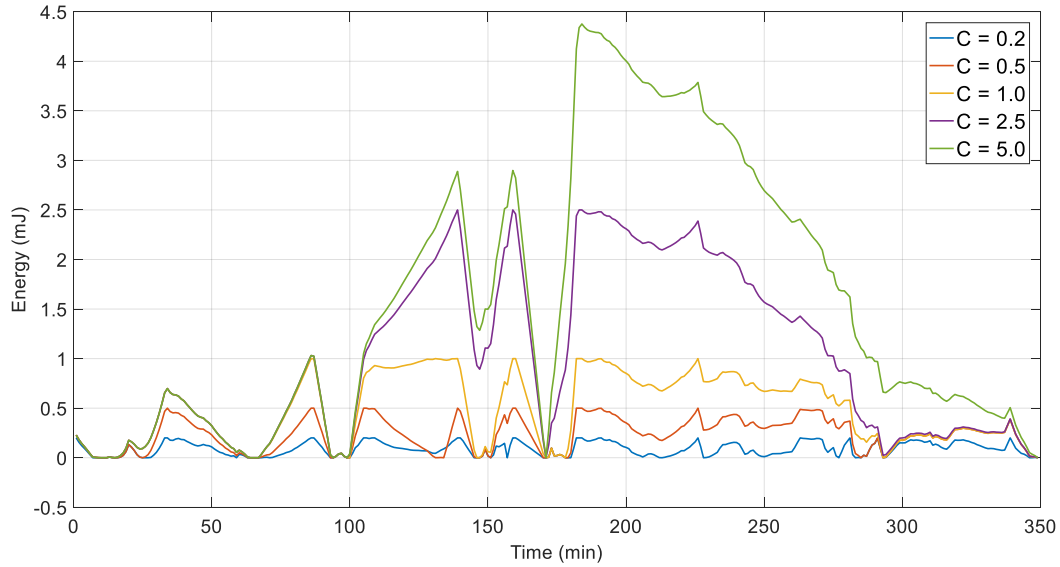
**Figure 5.4 Offline simulation of DPM strategies on an energy profile according to different capacity  $C$  values in mJ.**



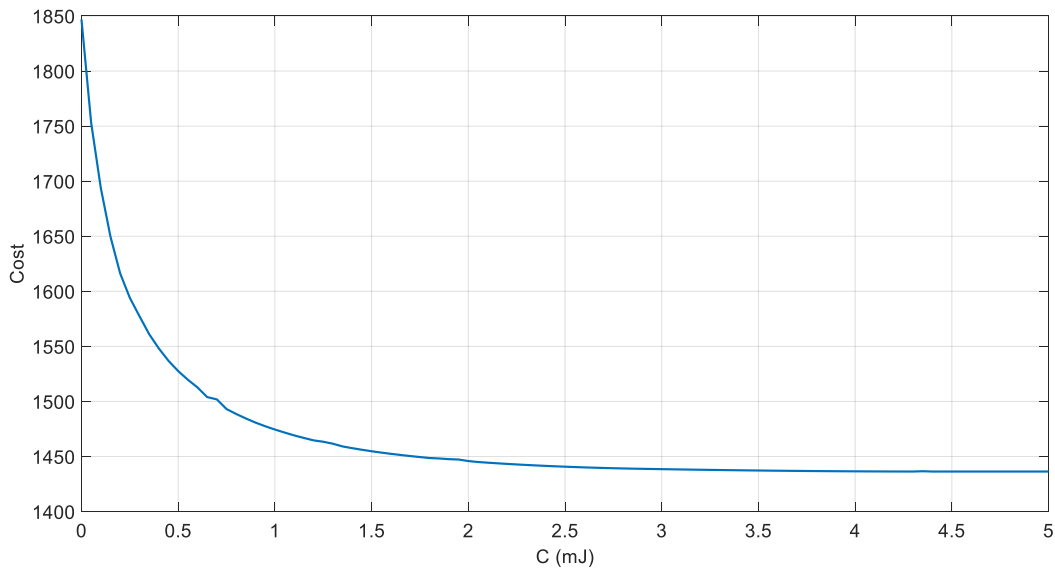
**Figure 5.5 The cost of the scheduling of each capacity  $C$ . The cost decreases along with the increase of the capacity  $C$  until  $C$  is large enough.**

Figure 5.6 illustrates the remained energy on the supercapacitor in each time slot. As the capacity  $C$  increases, more energy could be stored for future use. The maximum remained energy in this range is 4.38mJ, so when  $C$  is higher than it, the  $x$  and cost don't change.

In Figure 5.7, the capacity  $C$  is swept from 0 to 5 to calculate the cost for each  $C$ . The cost decreases as  $C$  increases from 0 to 4.38mJ and remains the same after that.



**Figure 5.6** The remained energy on the supercapacitor regarding different  $C$  values (mJ).



**Figure 5.7** The cost versus the capacity  $C$  from 0 to 5. The cost decreases as  $C$  increases from 0 to 4.38mJ and remains the same after that.

## 5.5 Online Scheduling with Energy Harvesting Prediction

The previously discussed solution with all  $e$  in advance could be called the "offline solution" or the "Oracle solution". In practice, future energy harvesting information is unavailable, and only the past  $e_i$  values are available. If there is no prediction, the trivial solution is to use up energy in each time slot, which is apparently not optimal. With a prediction model, short-term and long-term energy can be evaluated as shown in Figure 5.8 and the predicted energy values  $\hat{e}_i$  can be used for online scheduling algorithm similar to the offline algorithm.

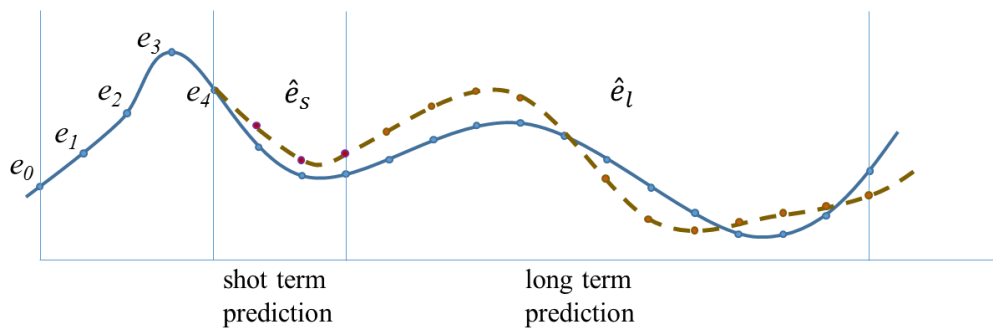


**Figure 5.8 Short-term and long-term prediction for online scheduling.**

Better energy prediction models with higher accuracy could improve the performance of the online scheduling to be closer to the optimal offline solution, and on the other hand, no prediction or poor prediction will perform inappropriate scheduling. For instance, predicting too conservatively leads to less energy consumption in the current time slot which is supposed to spend more to achieve better data quality. While predicting too radically leads to more energy consumption than it should be and will perhaps lead to system powering down.

To demonstrate that the accuracy of prediction models affects the power management performance, here is a simulation to compare the performance of different grades of predictions. Here we do not assume specific prediction methodologies and only model the short-term and long-term error range. Since short-term energy harvesting is more accessible to forecast than long-term,

the short-term error range  $err_s$  is assumed to be smaller than the long-term  $err_l$ . In each step, we "predict" future energy  $\hat{e}_l$  by adding a random noise with uniform distribution in the specific range ( $err_s$  or  $err_l$ ) to the real  $e_l$ . Then we update the algorithm to calculate the optimal solution with Algorithm 5.3 which is modified from Algorithm 5.2. In this online algorithm, in each step only one  $x_i$  for the current time slot is calculated which is different from the offline algorithms.

---

**ALGORITHM 5.3:**

---

- 1: **Input:**  $\hat{e} = [e_m, e_{m+1}, \dots, e_N]^T$  for future  $N - m + 1$  harvested energy in each time slot,  $r$  for remained energy from previous time slot,  $N$  for the number time slots, and  $C$  for the capacity of the battery
  - 2:  $J = \sum_{i=1}^N \frac{1}{x_i}$  as the cost function of data quality
  - 3: **Output:**  $x_m$ , energy consumption in the current time slot to minimize the cost
  - 4:  $j = \operatorname{argmin}(\frac{r + \sum_{i=m}^j e_i}{j - m + 1})$
  - 5:  $PE_l = \frac{r + \sum_{i=k}^l e_i}{l - m + 1} (m \leq l \leq j)$
  - 6:  $PF_l = \frac{r + \sum_{i=k}^l e_i - C}{l - m + 1} (m \leq l \leq j)$
  - 7:  $end = \max(k)$  s.t.:
  - 8:  $g_k(x) = 0$  (1) or  $h_k(x) = 0$  (2)
  - 9: assign  $x_m = PE_k$  for (1) or assign  $x_m = PF_k$  for (2)
  - 10: **return**  $x_m$
- 

The simulation result is shown below. The error range parameters ( $err_s, err_l$ ) for three prediction plots are (0.15, 0.60), (0.60, 2.00), (1.00, 3.50), respectively from the best to the worst. Figure 5.9 illustrates the energy consumption in each prediction method comparing to the offline solution, and Figure 5.10 shows the remained energy in each time slot. The cost of the offline, best prediction, medium prediction, worst prediction, and the greedy algorithm is 1438.54, 1440.51, 1467.66, 1590.67, 1846.87, respectively, as shown in Figure 5.11. Better prediction methods with higher accuracy will have better scheduling performance with lower cost.

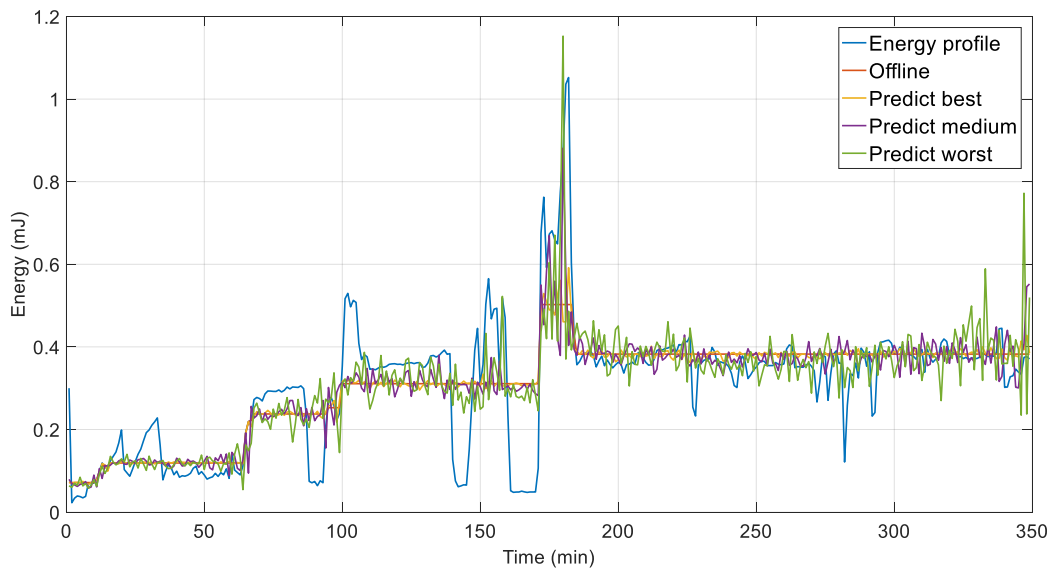


**Figure 5.9 Online energy consumption simulation in each prediction method comparing to the offline solution.**

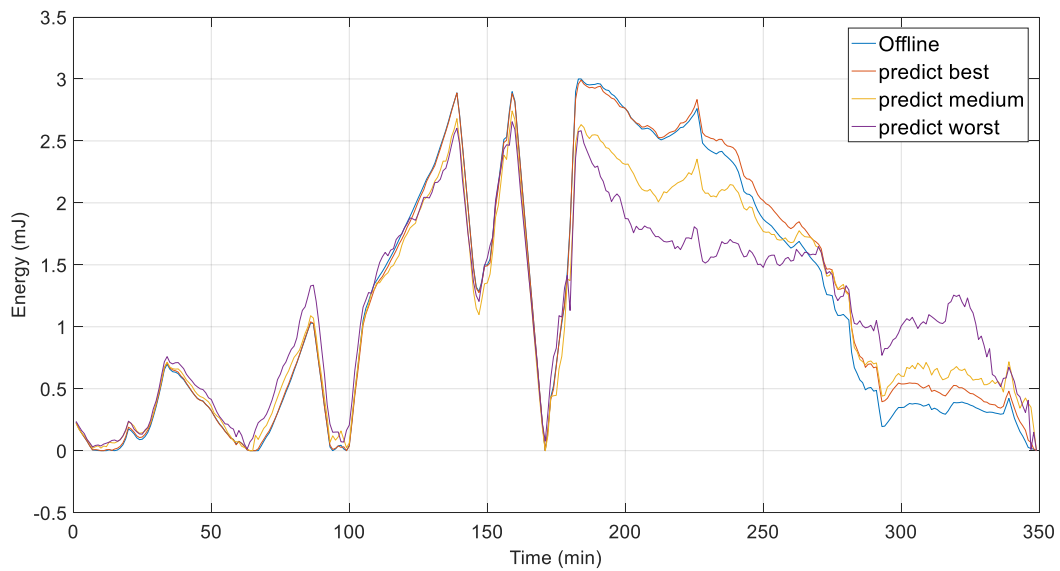


**Figure 5.10 The remained energy on the supercapacitor regarding different prediction methods.**

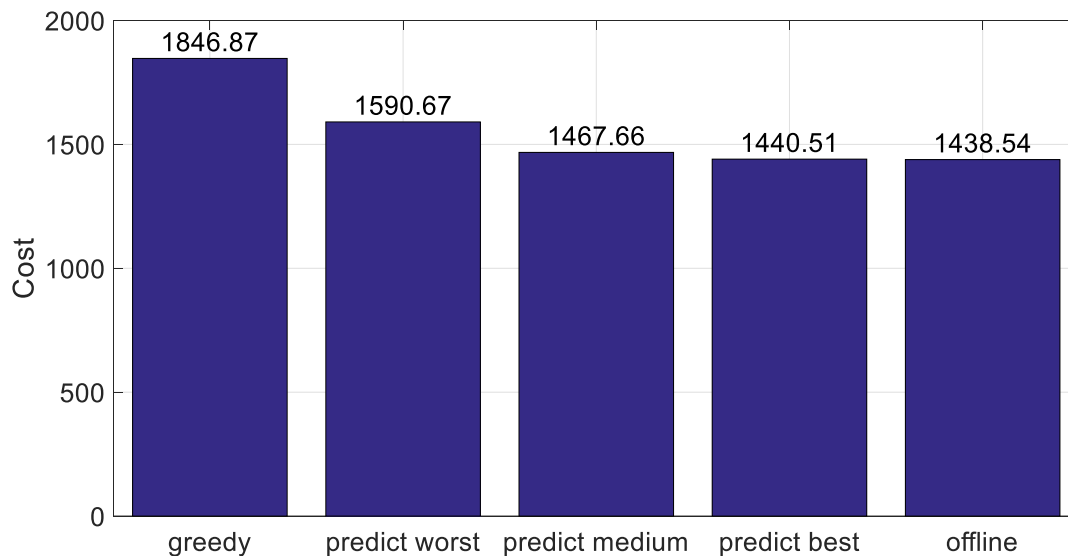


**Figure 5.11 Compare of the cost from the greedy algorithm, offline, online with three different prediction accuracies. The online algorithm performs better than greedy algorithm but worse than the optimal offline algorithm. The better prediction model has lower cost.**

## **5.6 A Case Study: Vigilant Atrial Fibrillation Monitoring**

In Section 5.2 ~ 5.5, we discussed the power management as a convex optimization problem and derived the optimal solution in offline and online scenarios. In this part, we study the vigilant Atrial Fibrillation (AFib) monitoring as a case study to further discuss the relationship between the application-specific data quality and system power consumption.

### **5.6.1 Vigilant Monitoring and Atrial Fibrillation**

In the context of sensor systems, the term “vigilant” has a specific meaning – a vigilant monitoring system is one that operates in a mode such that no critical events are missed. Events may be missed due to noise or user error, but not due to operational mode. It is important to note the difference between vigilant sensing and continuous sensing, as a continuous sensing system may not include all of the necessary sensors or operates at the minimum sampling frequency or quantization bit

depth to ensure that all critical events will be detected. Conversely, not all vigilant systems perform continuous sensing, as critical events may only happen during certain times, activities, and the system needs not operate otherwise. A precise definition of a critical event must be made before designing a vigilant monitoring system, and is inherently application dependent. For the use case application explored in this work, a critical event is AFib episodes as detected through ECG monitoring using a state-of-the-art AFib classification algorithm.

AFib is an abnormal heart rhythm, which is usually associated with heart diseases like a cardiac failure. Studies show that AF is related to stroke and frequently occurs in elderly persons[88]. The early detection and diagnose of AF could help to prevent heart failure and stroke. Therefore vigilant monitoring is necessary to capture transient periods of AF.

There are two main categories of AF detection approaches: using R-R intervals or QRS waveforms. In a comparative study of AF detection [89], different algorithm performances were compared, and the R-R interval-based approach provided better performance. Also, the QRS waveform could be distorted when the sampling rate is low; therefore, we focus on the R-R interval-based AFib detection in this work.

The R-R interval variations are analyzed in different ways for AFib detection. In [90], a normalized R-R interval variation threshold is set to classify AFib events. Some use both the R-R interval and its change for detection[91]. In [92], the Kolmogorov-Smirnov test is used to detect AFib episodes. In this paper, we use the method in [90] for its simplicity and high performance. There are five steps in this algorithm: a) determine the R-R intervals; b) normalize the R-R intervals as a feature normalization; c) compute the statistics of the normalized intervals; d) initially classify the AFib episodes using a settable threshold; e) smooth the classification results to reduce spurious errors and improve the overall performance.

For R-R interval calculation, there are algorithms including curve-length-transform in [93], wavelet-transform in [94], and some others. The curve length transform algorithm could deal with baseline changes using a dynamic threshold, and we use it in our experiment for AFib detection.

### **5.6.2 Application-Driven Metrics for Vigilant Monitoring**

The vigilant BSNs requires an application-driven approach to determine the relationship between power consumption and the ability to detect critical events. Previous works discuss signal quality versus power consumption, but many of these approaches come from a signal processing perspective using metrics such as Signal-to-Noise Ratio (SNR) and Mean Squared Error (MSE), which may or may not be tied to application-level information metrics, such as event detection vigilance.

A typical example is measuring the time interval between successive heart beats – R-R interval – which is frequently used in cardiac monitoring applications[93] including the AFib detection. The R-R interval is usually extracted from digital ECG signals. Figure 5.12 shows a 10-second window of ECG waveform from the database at a sampling rate of 250Hz, and the other five subplots are the downsampled version of the original signal at 200Hz, 100Hz, 50Hz, 20Hz, and 10Hz. The detected peaks using the curve length transform algorithm [93] are marked in red circles in each row. Along the downsampling, the signal quality of the ECG signal degrades, but the QRS complex detection can still be adequately performed down to 20Hz. Therefore, the R-R interval measuring performance cannot be precisely evaluated by the ECG signal quality.

In the following, we analyze the relationship between AFib detection performance and ECG sampling rate and quantization depth. The sampling rate is directly related to the power consumption of a sensing system as proved in Section 6.4. The quantization depth of a sample decides the data rate of the system which also affects the total power consumption.

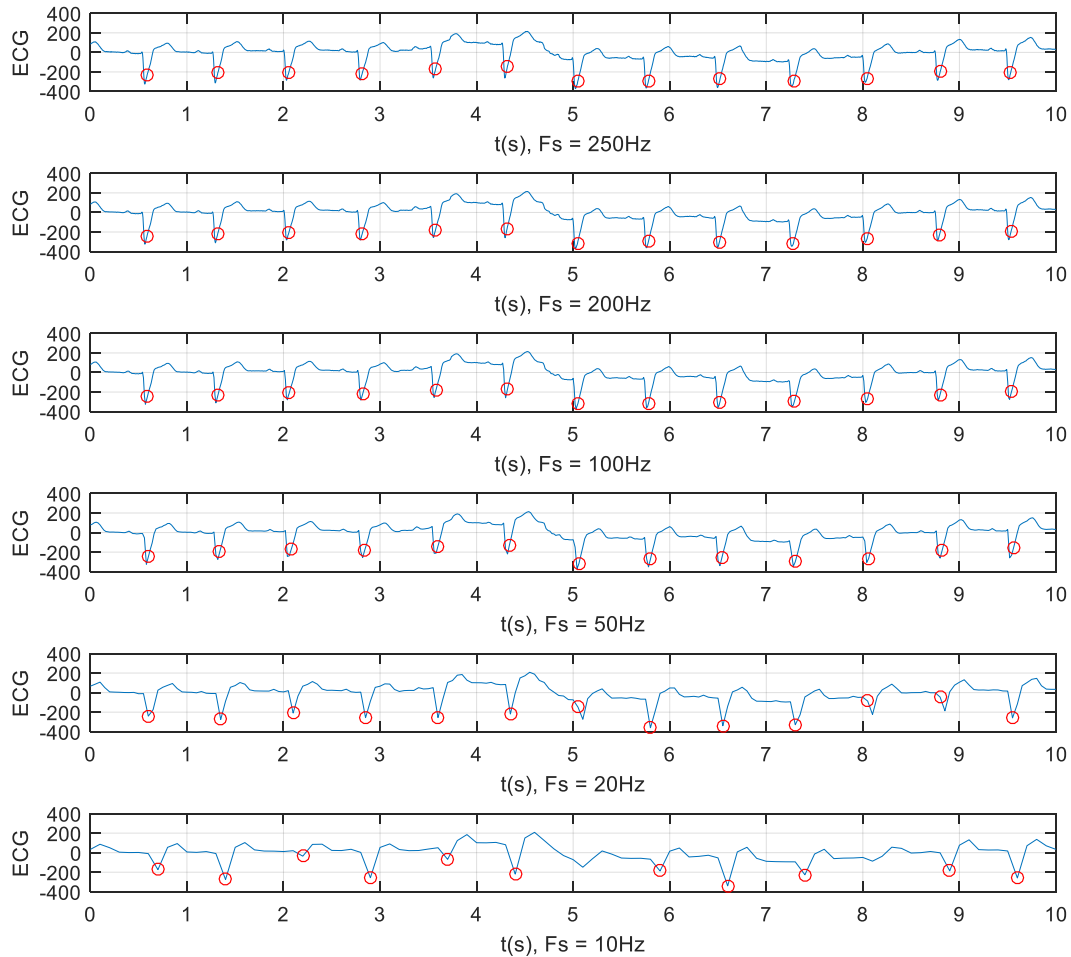


**Figure 5.12 ECG waveforms and detected QRS complexes in red circles with different sampling rates at 250Hz, 200Hz, 100Hz, 50Hz, 20Hz, and 10Hz. With the decrease of the sampling rate, the ECG signal becomes distorted, but the QRS complex detection works well until a minimum sampling rate of 20Hz.**

Since the AFib detection is binary classification task to distinguish regular heartbeats and abnormal AFib episodes, the metrics of classification performance are discussed. The assessment of the performance of a classifier is a complex topic, and there are various measures including accuracy, precision, recall, F score, receiver operating characteristic ROC, and many others [95]. Though these measures are commonly used in the machine learning area, the effectiveness of the

measures remains debatable. The discussion of the effectiveness of measures is out the scope of this work, and we selected the most frequently used metrics of the ROC curve and the F score. In addition, we used the metrics to evaluate how different data qualities affect the performance of the same classifier rather than assessing the performance of different classifiers.

The ROC curve is constructed by adjusting parameters used to classify the two categories and plotting the true positive rate (sensitivity) and false positive rate (1-specificity) [95] [96]. The area under the ROC curve (AUC) is usually used for performance comparison. The F score is a measure of the accuracy of a test considering both the precision and recall [95] as shown in (5.72). The  $F_1$  score is the harmonic average of the precision and recall as shown in (5.73). In AFib detection and many other medical applications, false negatives (failing to detect critical events) are much worse than false positives. In other words, more emphasis should be put on the false negatives and the recall should be weighted higher. In such case the  $F_2$  score is preferred as shown in (5.74).

$$F_{\beta} = \frac{(1 + \beta^2)precision \cdot recall}{\beta^2 \cdot precision + recall} \quad (5.72)$$

$$F_1 = \frac{2 \cdot precision \cdot recall}{precision + recall} \quad (5.73)$$

$$F_2 = \frac{5 \cdot precision \cdot recall}{4 \cdot precision + recall} \quad (5.74)$$

### 5.6.3 Experiments and Results

In the experiment, the original ECG data was retrieved from the MIT-BIH AF database [97], number 05121. The total recording length is 10.23 hours, which contains 26 AF and premature junctional episodes that comprise 6.51 hours out of the total length. The raw signal was sampled at 250Hz with 12-bit resolution over a range of  $\pm 10$ mV. The recording bandwidth of the ECG recorders is from 0.1Hz to 40Hz. The WFDB MATLAB Toolbox [98][99] was used for reading

the ECG signal and annotations. The curve-length-transform based R-R interval calculation algorithm was reimplemented from [93] to tune the parameters for dealing with low sampling frequency scenarios.

The original ECG signals are resampled or truncated to emulate different sampling rates and quantization depths. Then the AFib detection performance based on the R-R interval calculation algorithm is compared in each case to determine the impact of the signal quality in the application performance.

The ROC curves of AFib detection under nine sampling rates from 250Hz to 10Hz are illustrated in Figure 5.13. In general, the curve moves inward (performance decreases) as the sampling rate decreases. The AUC and the maximum  $F_2$  score of AFib detection under nine sampling rates are illustrated in Figure 5.14. The values in general increase with the sampling rate.

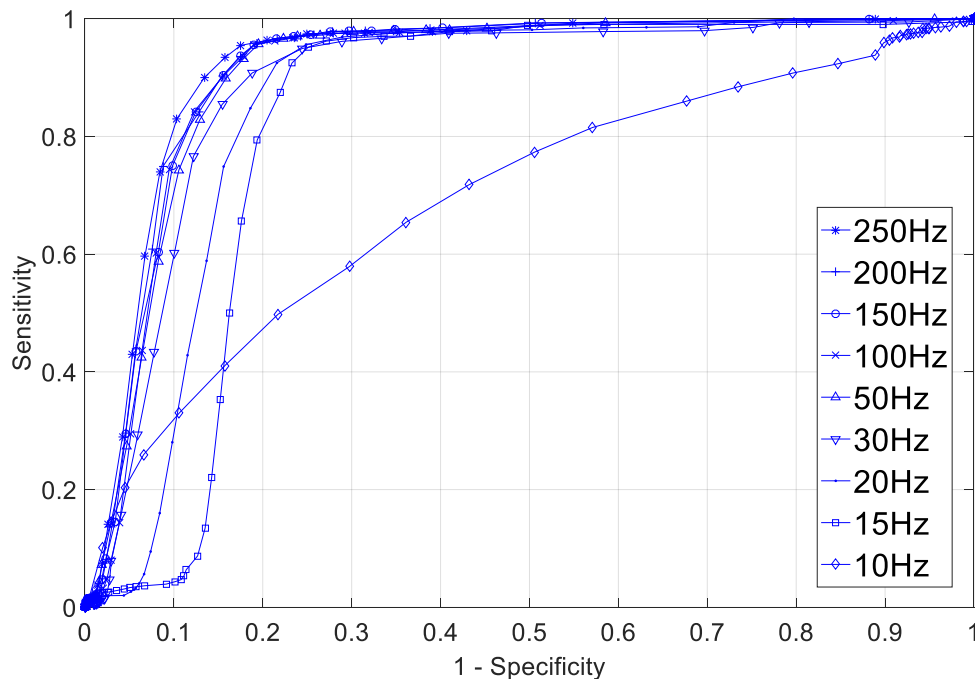


**Figure 5.13 The receiver operating characteristic (ROC) curves of AFib detection under nine sampling rates. The curve is moving inward as the sampling rate decreases.**

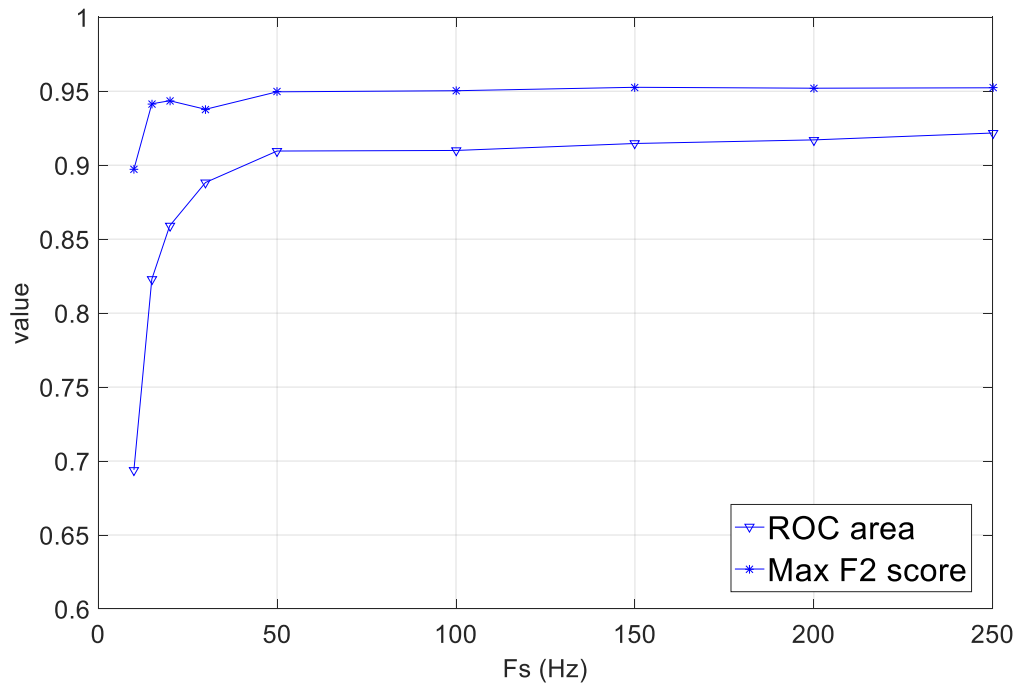


**Figure 5.14 The ROC area (AUC) and the maximum  $F_2$  score of AFib detection under nine sampling rates. The value in general increases with the sampling rate.**

Similarly, the ROC, AUC, and the  $F_2$  were analyzed over quantization depths from the original 12 bits to 6 bits as illustrated in Figure 5.15 and Figure 5.16.

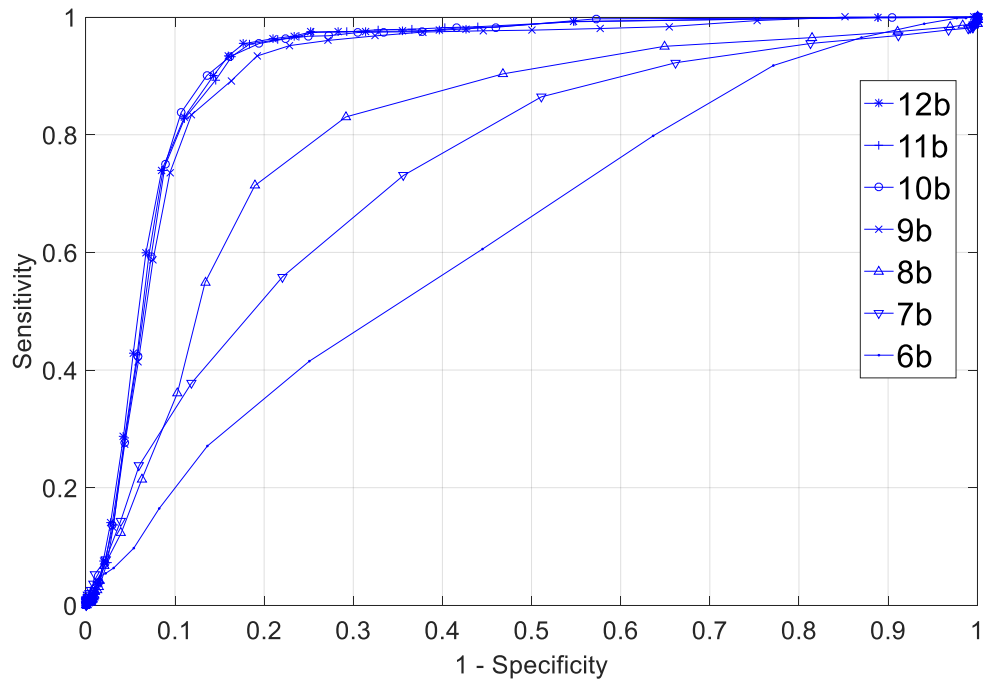


**Figure 5.15** The receiver operating characteristic (ROC) curves of AFib detection under seven quantization depths. The curve is moving inward as the quantization depth decreases.

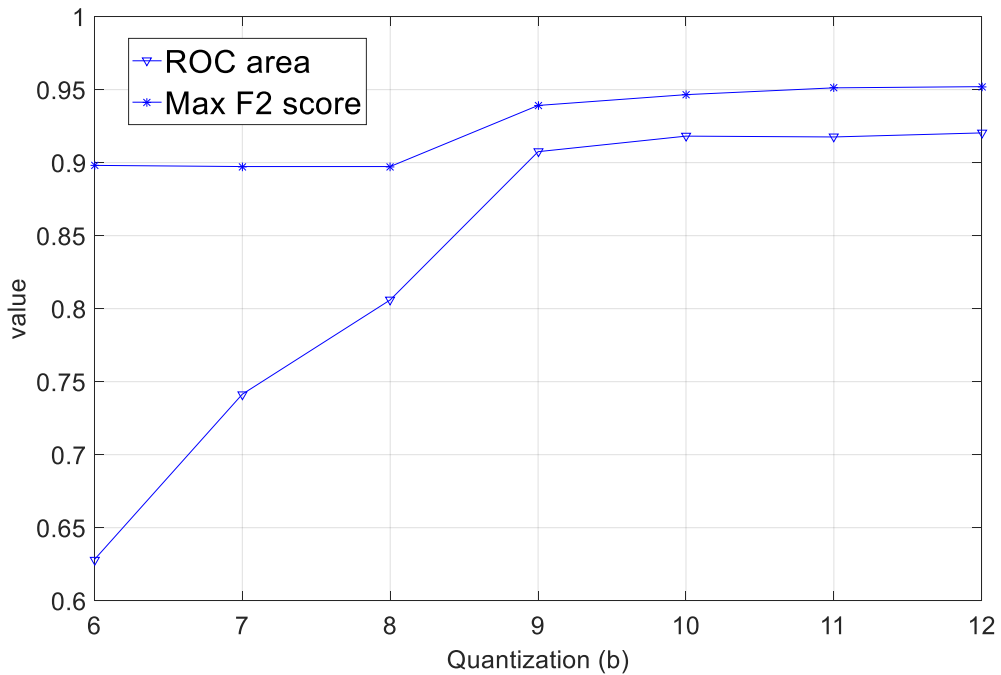


**Figure 5.16** The ROC area (AUC) and the maximum  $F_2$  score of AFib detection under seven quantization depth. The value in general increases with the quantization depth.

Finally, we combine the sampling rate and quantization depth and discuss the relationship between the AUC and the overall system power consumption. The 3D plot of AUC related to the sampling rate and quantization depth is illustrated in Figure 5.17. In general, the AUC representing the performance increases with the quantization depth and sampling rate, but there are abnormalities when the quantization depth is low as shown in Figure 5.17. The main reason is that the initial classification result is smoothed using a majority vote as discussed in Section 5.6.1. At the low quantization bits, the R-R intervals calculation performs poorly, but the smoothing may increase the performance irrelevant to the sampling rate. However, quantization depth lower than 8 bits is impractical due to the low signal quality and usually are not considered in real-world monitoring.

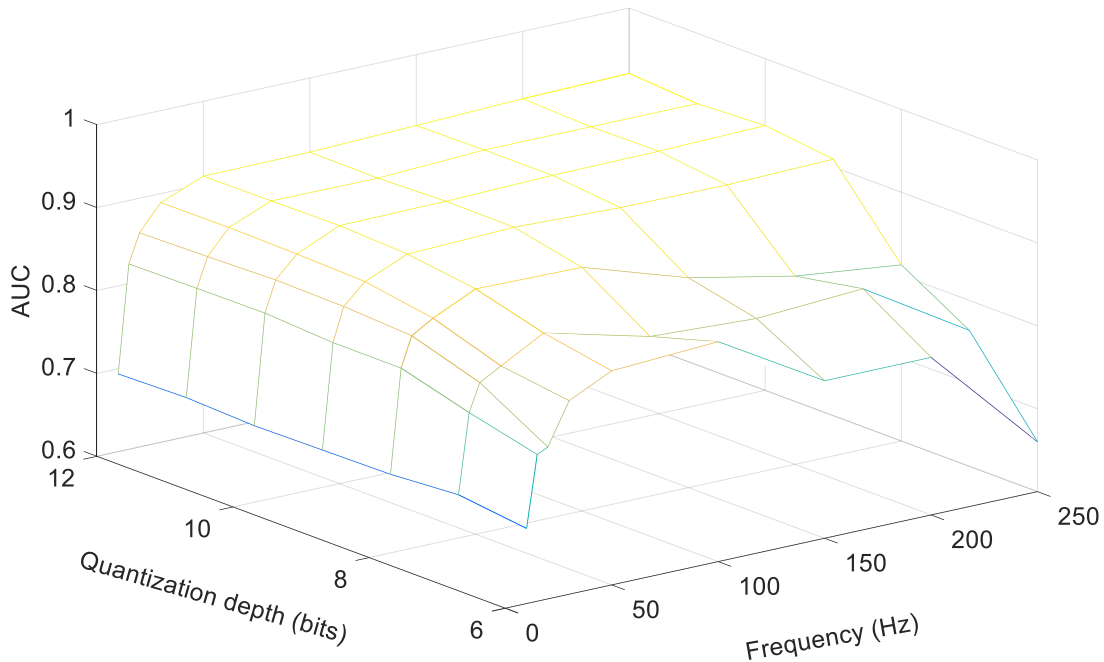


**Figure 5.17 The ROC area (AUC) versus quantization depth and sampling rate.**

The power consumption of the sensor system is mainly decided by the sampling rate and quantization depth. Employing the power consumption model by equation (6.3) and (6.9) in Section 6.4, the design space of combinations of the sampling rate and quantization depth is

illustrated by the blue markers in Figure 5.18. The red line is part of the convex hull of all the points, and it represents the optimal design decisions at specific power consumption level.

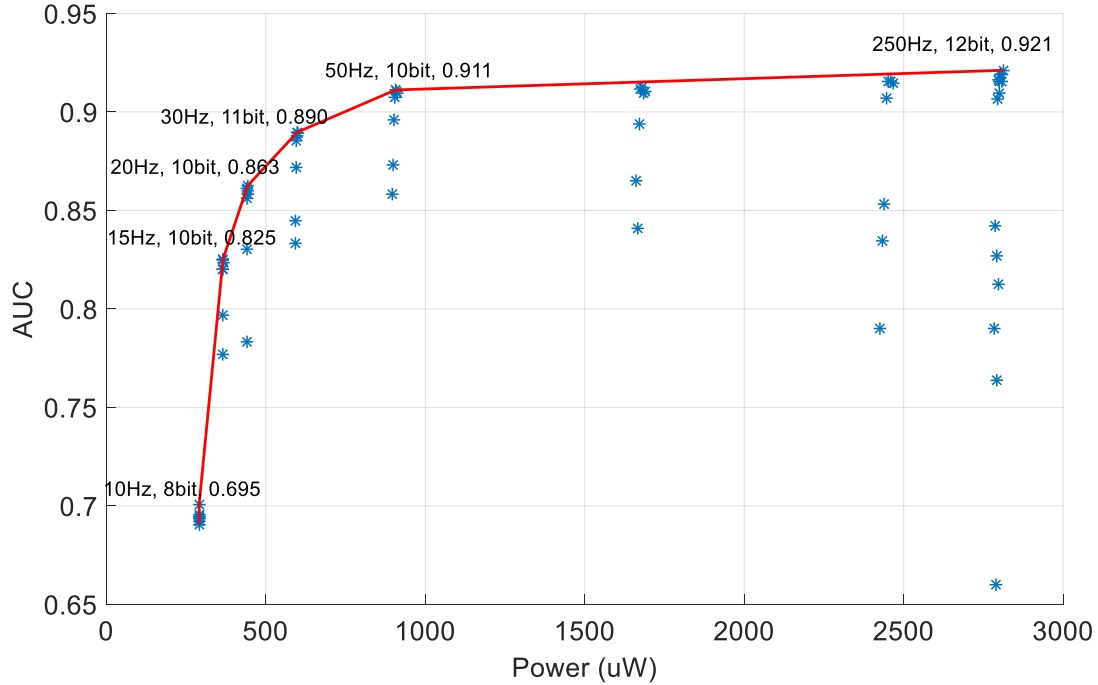


**Figure 5.18 Design space considering the sampling rate and quantization depth. Power consumption is calculated using a model developed in Section 6.4 of our SCDPM platform. The red line is part of the convex hull of all the points, and it represents the optimal design decisions at specific power consumption level.**

### 5.6.4 Application-Specific Cost Function

In Section 5.2 we used a simple form cost function (5.3) to derive the optimal solution. In this part, we will derive the application-specific cost function with cur fitting and prove that the optimal solution remains the same.

Since AUC represents the AFib detection performance,  $1-AUC$  could be used as the cost function. Using the previous dataset of the power consumption and AUC, a curve is fitted with the form of (5.75). The Root Mean Squared Error (RMSE) of the curve fitting is 0.0023 which is very small. The parameters  $a = 14.64$  and  $b = -3287.4$ , and they satisfy (5.76).

$$f(x) = \sum_{i=1}^N \frac{x_i}{ax_i + b} \quad (5.75)$$

$$a > 0, b < 0, ax_i + b > 0 \text{ for all } x_i \quad (5.76)$$

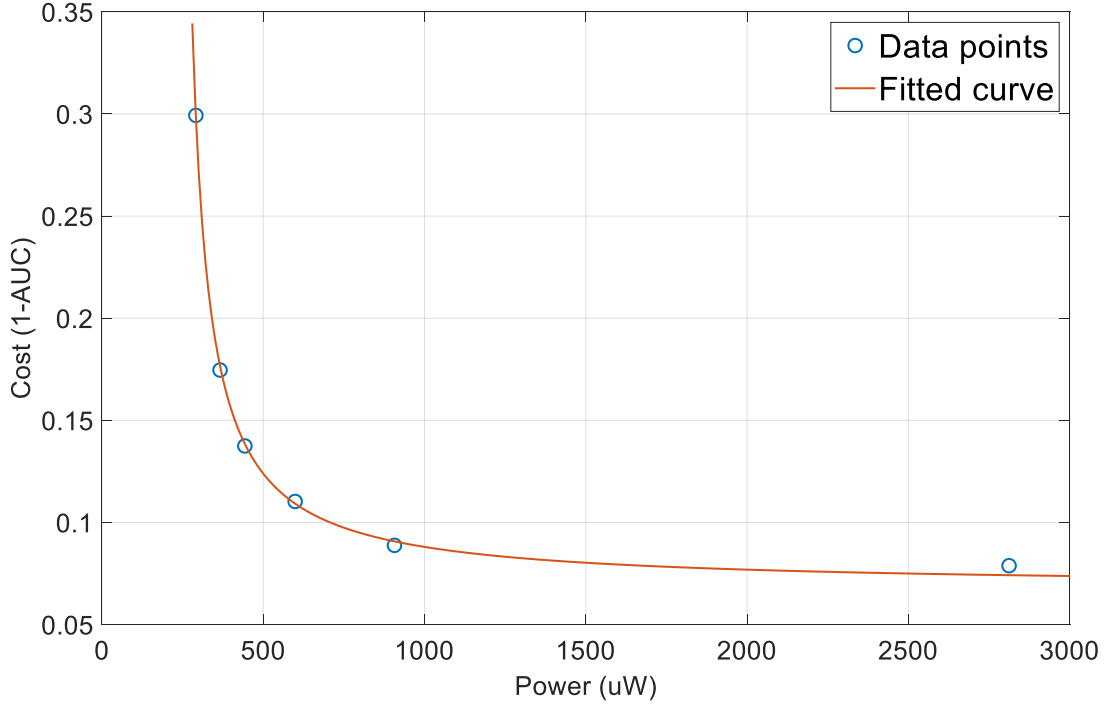


**Figure 5.19** Curve fitting of the cost function, which is power versus AUC.

The cost function (5.75) is different from (5.3), but the optimal solution remains the same. With (5.75), the (5.25) is changed to:

$$\frac{-b}{(ax_i + b)^2} = \sum_{k=i}^N \lambda_k \geq 0 \quad (5.77)$$

$$\lambda_i = -b \left( \frac{1}{(ax_i + b)^2} - \frac{1}{(ax_{i+1} + b)^2} \right) > 0 (i = 1, 2, \dots, N - 1) \quad (5.78)$$

$$\lambda_N = \frac{-b}{(ax_N + b)^2} > 0 \quad (5.79)$$

For (5.78):

$$\lambda_i = -b \left( \frac{1}{(ax_i + b)^2} - \frac{1}{(ax_{i+1} + b)^2} \right) > 0 \quad (b < 0) \Rightarrow \quad (5.80)$$

$$\frac{1}{(ax_i + b)^2} - \frac{1}{(ax_{i+1} + b)^2} > 0 \quad (ax_i + b > 0) \Rightarrow$$

$$ax_i + b < ax_{i+1} + b \quad (a > 0) \Rightarrow x_i \leq x_{i+1}$$

Therefore, the inequality (5.27) still holds.

For (5.36) in the discussion of the optimal solution:

$$\begin{aligned} \Delta f(x) &= \left( \frac{x_{b'}}{ax_{b'} + b} + \frac{x_{1'}}{ax_{1'} + b} \right) - \left( \frac{x_b}{ax_b + b} + \frac{x_1}{ax_1 + b} \right) \\ &= \frac{PE_{k^*} - \varepsilon}{aPE_{k^*} + b - a\varepsilon} + \frac{PE_{k^*} + \varepsilon}{aPE_{k^*} + b + a\varepsilon} - \frac{2PE_{k^*}}{aPE_{k^*} + b} \\ &= \frac{-2ab\varepsilon^2}{(aPE_{k^*} + b - a\varepsilon)(aPE_{k^*} + b + a\varepsilon)(aPE_{k^*} + b)} > 0 \end{aligned} \quad (5.81)$$

Other parts in the solution are only related to the constraints rather than the cost function.

Therefore, the solution does not change. The problem with the supercapacitor capacity limit is similar to prove.

To sum up, with the application specific cost function (5.75), we could still utilize the algorithms discussed in Section 5.3~5.5 to execute the DPM scheduling.

## 5.7 Summary

This chapter demonstrated that the proposed convex optimization model could be utilized to solve the power management in energy harvesting systems. The proposed solution can improve the system power management performance.

The ‘‘Oracle’’ solution is the optimal solution assuming the harvested energy in each slot is given in advance. This optimal solution is the theoretical solution while impractical in the real-world applications. Therefore, the online version of the scheduling algorithm is discussed

assuming energy harvesting prediction methods are employed. With the better accuracy of the future energy prediction, the performance of the online algorithm is closer to the offline version.

In the last part, we analyzed the vigilant AFib detection as a case study to discuss the relationship between power consumption and the detection performance. An application-specific cost function is derived, and we proved that the cost function is not limited to the pure form as illustrated in (5.3) but rather working for many convex functions. In fact, any cost functions which are both nonincreasing and convex will have the same solution. Our optimal solution only relies on the constraints which include the energy harvesting data and the battery capacity. And it is irrelevant to the specific form of the cost function. Compared with the off-the-shelf convex optimization solvers which depend on the cost function forms, our algorithm has better speed and less complexity.

Future work could explore more medical applications to extend the scope of the proposed DPM model. Another direction of the future work is to validate the algorithm on the real-world deployments.

# **6 Self-powered Context-aware Dynamic Power Management Platform**

In this chapter, the Self-powered Context-aware Dynamic Power Management Platform (SCDPM) design is described. The SCDPM is a multimodal context-aware self-powered wearable sensor system for real-world vigilant cardiac and activity monitoring that achieves a positive energy balance from both solar and thermoelectric energy sources. The platform collects ECG, acceleration, and environmental parameters including light intensity and ambient air temperature. It wirelessly streams data to a smartphone through Bluetooth Low Energy (BLE) for data visualization and processing. Besides, the sensor data is interfaced to specific cloud service in real time for data storage, remote data access, and caregiver/clinician/researcher notification.

A target of the SCDPM is to execute real-world self-powered health monitoring with the capability of ECG, motion, and environmental sensing. This function will be validated in Section 7, and the collected profiles will be presented and analyzed.

The SCDPM is also used to validate the proposed energy prediction and DPM algorithms. It receives commands from the phone in real-time for power management according to the DPM

scheduling algorithm to dynamically adjust its operating parameters. The DPM algorithm runs on the phone side since the phone has stronger computing capability and more power budget.

The hardware system design is described in Section 6.1, and the software design including Android programming on the phone side and embedded C programming on the sensor node side is described in Section 6.2 and Section 6.3. In Section 6.4, the power consumption model of SCDPM is discussed.

## **6.1 Hardware System Design<sup>3</sup>**

The SCDPM platform is a custom component-off-the-shelf (COTS) based sensor system designed to perform long-term vigilant cardiac and activity monitoring and environmental sensing that continuously samples and wirelessly streams sensor data to a smartphone through BLE. It has three printed circuit boards (PCBs) including the main board for control and data transmission, a sensing board for ambient temperature and light intensity sensing, and an energy harvesting board, as shown in the block diagram in Figure 6.1. The distributed architecture gives the system certain extendibility to interface with different harvesters and more sensors if the target application is changed.

---

<sup>3</sup> For the hardware system design of SCDPM, Luiz Lopez Ruiz worked on the main board, and the author of this dissertation worked on the energy harvesting board and the sensing board.

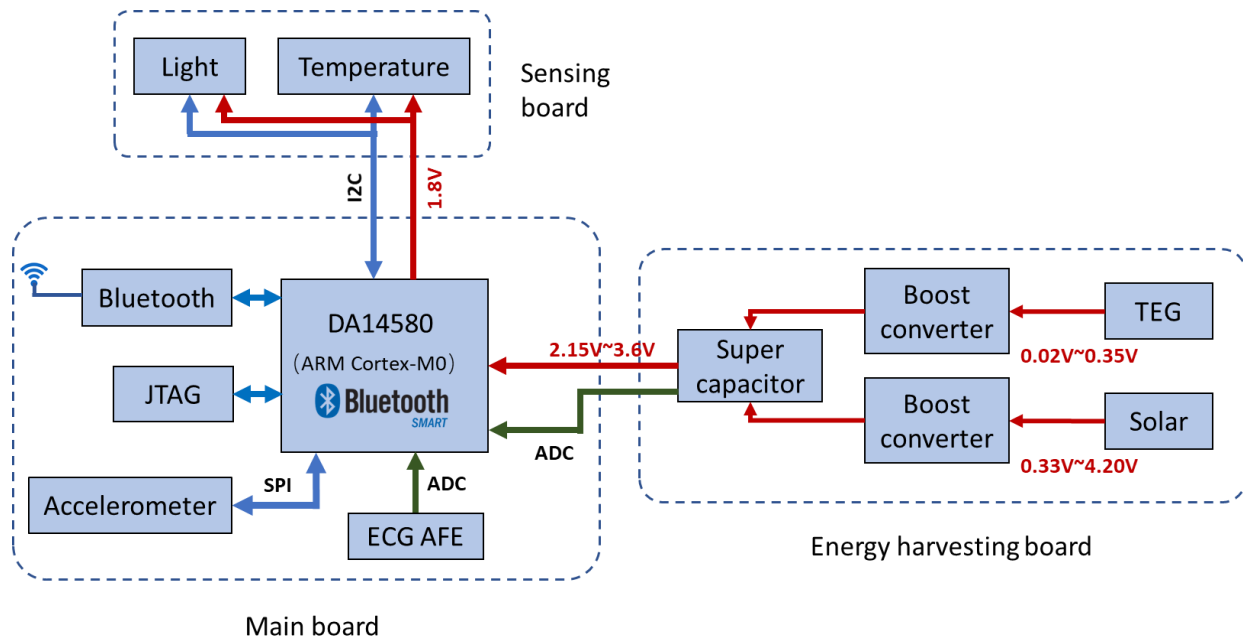


**Figure 6.1 Block diagram of the SCDPM platform including a main board, a sensing board, and an energy harvesting board.**

The main board which performs the system control and data transmission function is based on a DA14580 ARM Cortex-M0 SoC from Dialog Semiconductor. The DA14580 is responsible for controlling and wireless BLE data transmission. The main board also consists of an accelerometer for motion tracking and a discrete analog-front-end (AFE) and an ECG electrodes connector for ECG monitoring.

The energy harvesting board performs multimodal energy harvesting from solar and thermoelectric energy sources and energy storage. It integrates boost converters, a supercapacitor, and connectors for solar cells and thermoelectric generators (TEGs).

The sensing board consists of a light sensor and ambient air temperature sensor. Both sensors communicate with the main board through an I<sup>2</sup>C interface.

The form factors of the PCBs are optimized to be compact to improve the wearability of the platform. Both the main board and the energy harvesting board are around 1.30in by 0.99in, and

the sensing board is 0.26in by 0.31in. The detailed design of each block is described in the following subsections.

### **6.1.1 Control and Data Transmission**

The Control and Data Transmission block is the core of the platform which controls the system workflow and communicates with smartphones through wireless protocols. The controller is required to execute computation tasks, to interface with various sensors, to manage the system memory and power consumption, and to have ultralow power consumption. Bluetooth Low Energy (BLE) is employed to achieve low power data transmission. BLE consumes much less power, 0.01mW ~ 10mW, compared with Bluetooth 1mW ~100mW[Bluetooth specs]. The data rate of BLE is less than Bluetooth. However, it is sufficient for health applications.

The ultra-low power processor DA14580 from Dialog Semiconductor is used in this project to meet the above requirements. The chip integrates a 16 MHz 32-bit ARM Cortex-M0 core and a dedicated Bluetooth 4.2 compliant radio transceiver and baseband core. The BLE transmitter has a configurable output power of 0 dBm or -20 dBm, and the receiver sensitivity is -93dBm. The onboard memory resources are limited, mainly including 32kB One-Time-Programmable (OTP) memory for custom application code, 42kB System SRAM, 8kB Retention SRAM, and 84kB ROM for the BLE protocol stack and the boot code sequence for start-up. For the peripherals, the chip incorporates 32 General Purpose I/O (GPIO) channels, an SPI bus, and four 10-bit analog-to-digital converter (ADC) channels.

A highlight feature of the DA14580 is its various power modes. Besides the active mode, there are two sleep modes including the extended sleep mode and the deep sleep mode. In the deep sleep mode, only the Retention SRAM is switched on, and in the extended sleep mode, both Retention and System SRAM are switched on. Current consumption is significantly reduced to around 1.4uA

for extended sleep mode and 0.8uA for deep sleep mode which brings opportunity for dynamic power management. Since the BLE connection interval is less than 2 seconds for most of the scenarios in our applications, extended sleep mode is employed according to the Dialog user manual. The “sleep mode” is used to refer to “extended sleep mode” hereafter.

### 6.1.2 Energy Harvesting

The Energy Harvesting block supplies power to the entire system by extracting the available power from the solar cells and TEGs and stores surplus energy into a supercapacitor. The block includes the energy harvesting board, solar cells, and TEG arrays.

In the project, flexible solar cells from PowerFilm Solar are selected in consideration of the system wearability. Two LL200-3-37 and two MP3-37 cells are serialized with a combined surface area of 27.0 in<sup>2</sup> and surrounded to a running armband to optimize the wearability. The characterization P-V curves of the combined solar cells under typical indoor and outdoor illumination levels is presented in Figure 6.2. All P-V curves were generated using a program to sweep current and measure voltage with a Keithley 2400 source meter. The Maximum Power Point (MPP) of the solar cells is usually 80% of their open circuit voltage as shown in the figure.

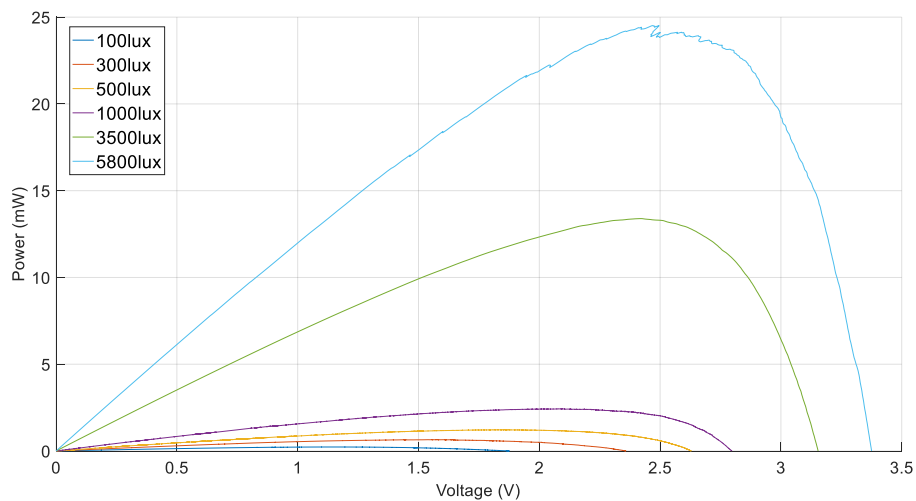


**Figure 6.2 Solar panel characterization.**

An ultra-low power with high-efficiency DC-DC boost charger BQ25505 from Texas Instruments is selected to utilize the solar power. It is responsible for tracking the MPP dynamically and extracting the maximum power available from the solar cells then distribute the energy to the system load and energy storage. When there is surplus harvested energy, it is stored on the supercapacitor, and when the input is insufficient or unavailable, the supercapacitor will power the system instead. The boost charger has various thresholds which can be configured using a resistor network for battery undervoltage protection, overvoltage protection, and normal operating range. The standard operating range of the battery is configured to be 2.2V ~ 3.6V since 2.2V is the minimum voltage for BQ25505 and 3.6V is the maximum voltage for the system load (DA14580). The cold-start voltage of the boost charger is 330mV, and the maximum operating voltage is 5100mV. The output voltage for powering the system load is configured to be 3.6V, and the charger efficiency is 79.0% ~ 95.0% when the input is from 330mV ~ 4200mV. The charger efficiency increases with the input voltage.

For thermoelectric energy harvesting, the thermoelectric generator SP5424-AC from Marlow Industries Inc is selected. Small TEG pads considering the wearability for integration on a running armband, are preferred and could be connected in an array to increase the power. The dimension of each TEG is 0.26in by 0.52in. Ten TEGs are connected in series, and two such groups are connected in parallel to constitute a 4 by 5 TEG array as shown in Figure 6.3. The TEG array is fixated on a thin flexible plastic board to avoid breaking wires when it is stretched. The connection style of TEGs should consider both the current and voltage from the TEGs.

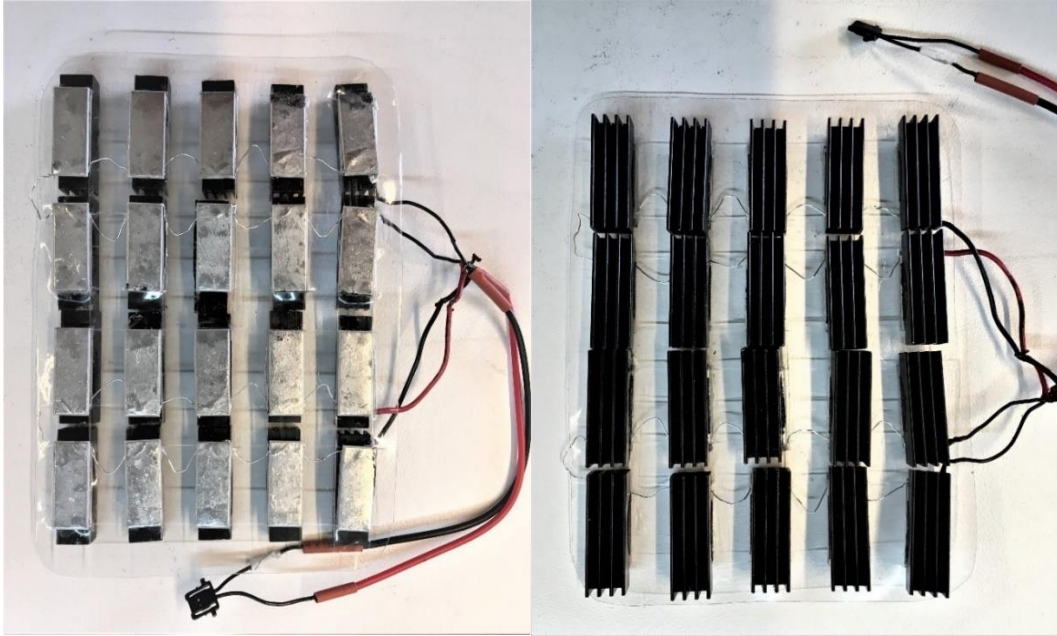


**Figure 6.3 TEG array. Hot side in the left picture attaching to people's skin, and cold side with a heat sink to dissipate heat into the ambient air.**

The characterization of the created TEG array is shown in Figure 6.4. In the experiment, the TEG array was put on a hot plate with the room temperature of 22°C. The temperature of the hot plate was adjusted from 27°C to 45°C. All P-V curves were generated using a program to sweep current and measure voltage with a Keithley 2400 source meter. The MPP of the TEG is usually 50% of their open circuit voltage as shown in the figure. Compared with solar cells, TEGs have less power and less open circuit voltage.

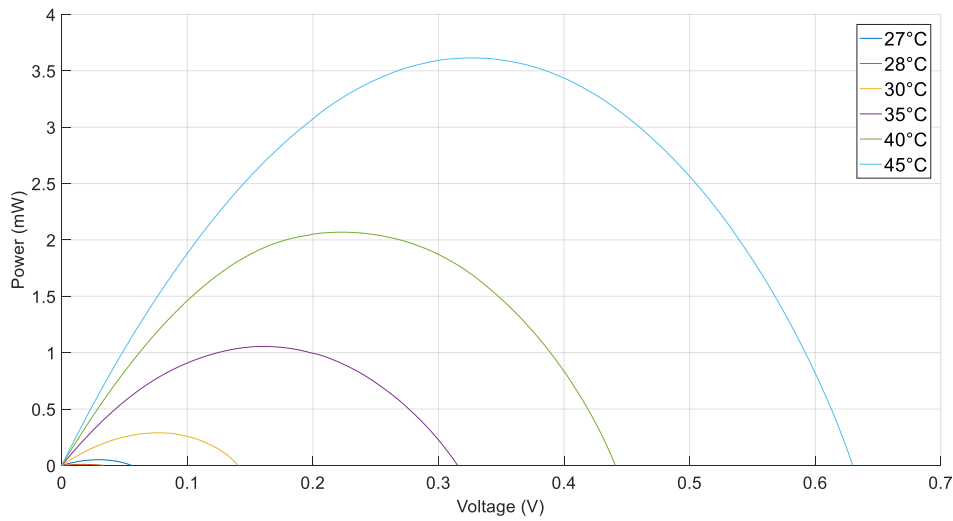


**Figure 6.4 TEG characterization under a room temperature of 22°C.**

When using TEG on the human body, the hot side usually attaches the skin, and the cold side with heat sink exposes to the ambient air. The location of skin for TEG and the airflow should be considered to optimize the TEG power. The skin temperature varies at different locations as shown in [100], where the human body skin temperature is investigated, and the experiments were conducted with 26 people. The average temperature from ten locations at the neutral sensation is summarized (in descending order) in Table 6.1. The forehead has the highest average temperature, followed by belly, chest, and other locations. Hand and foot have the lowest temperature.

**Table 6.1 Skin temperature of ten different body locations.**

Location	Temperature (°C)
Forehead	35.47
Belly	35.34
Chest	33.98
<i>Upper arm</i>	32.09
Thigh	31.97
Anterior calf	31.43
Wrist	30.57
Posterior calf	30.15
Hand	29.89
Foot	29.30

In addition to the static temperature of the location, airflow around the specific location when people are doing normal activities should be considered as well. For instance, the hand and arm have more airflow than the chest and belly when people are walking, running, or waving hands. Besides, the wearability is also an essential factor to consider where to put the TEGs. For instance, it is inconvenient to put TEGs on forehead or chest or belly. Consider all these tradeoffs; we choose to put the TEG on the upper arm by integrating the TEGs on to a running armband.

The voltage from the TEG array under normal conditions is less than 400mV, which requires ultralow voltage boost converters. The LTC3108 from Linear Technology is selected for its extremely low input from 20mV, and the input range is 20mV to 500mV. When using a 1:100 ratio transformer in our design, the efficiency increases from 35% to 40% when the input voltage increases from 20mV to 50mV and the efficiency decreases from 40 % to 5% when the input increases continually to 500mV. Similar to the BQ25505, the LTC3108 could store the surplus energy on a supercapacitor extract energy from it to power the system when there isn't enough input voltage.

A 1F supercapacitor is connected to the solar and TEG energy harvesting circuitries together to store the harvested energy. As mentioned before, the working range of the supercapacitor is from 2.2V to 3.6V.

### **6.1.3 Sensing**

The sensing modalities include motion, ECG, light, temperature, and the voltage on the supercapacitor. A summary of the sensors is listed in Table 6.2. The accelerometer and ECG circuits are located on the main board. The SPI bus is used to communicate with the accelerometer, and an ADC channel is used to digitize the ECG signal. The light and temperature sensors are located on a separate sensor board interfacing the main board through a Flexible Flat Cable (FFC)

using the I<sup>2</sup>C bus. An internal ADC channel VBAT\_3V of the DA14580 is used to measure the voltage on the supercapacitor.

**Table 6.2 Sensing modalities, IC, the interface with DA14580, and power consumption. The sampling rate is 100Hz.**

Sensor	IC	Interface	Power
Accelerometer	ADXL362	SPI	4.6uW
ECG	custom circuit	ADC	67.0uW
Light	MAX44009	I <sup>2</sup> C	1.2uW
Temperature	PCT2202	I <sup>2</sup> C	54.0uW
Voltage	-	ADC	-

The ADC of the DA14580 has 10-bit resolution, and the range could be programmed to be either 0 ~1.2V or 0 ~ 3.6V. There are four general ADC channels and six internal channels for measuring input power supply and reference voltages.

Custom analog low pass filters constitute the ECG AFE. The AFE consists of discrete LPV521 operational amplifiers from Texas Instruments. The quiescent current of these amplifiers is 400nA, and the supply voltage ranges from 1.6V to 5.5V. Standard 3M patch electrodes are used to attach on the human skin, and three button leads are attached to an interface with the AFE circuit.

A 3-axis digital output MEMS accelerometer ADXL362 from Analog Devices is selected to track the motion. The ADXL has at most 12-bit data width, while in the project 8-bit data width is configured for saving power. The measurement range is configured to be from -2g to 2g which is sufficient for human motion tracking. The operating range is from 1.8V to 3.3V, and it consumes less than 5μW of power at a 100 Hz output data rate in normal operation mode. The device incorporates a standard Serial Peripheral Interface (SPI) that communicates with the controller.

The ultralow power digital light sensor MAX44009 from Maxim Integrated is selected to measure the light intensity in both indoor and outdoor environment. It has an ultra-wide 22-bit dynamic range from 0.045lux to 188000lux, and the consumes 0.65uA with the supply voltage

range of 1.7V to 3.6V. The digital data output format consists of a 4-bit exponent and an 8-bit mantissa, and the device communicates with the controller through the I<sup>2</sup>C bus. The resolution of the lux values scales with the absolute measurement.

The PCT2202 temperature sensor from NXP company is used to measure the ambient air temperature for predicting thermoelectric energy harvesting. The PCT2202 is an ultralow power sensor which consumes 30uA active current and 1uA shut-down current. The accuracy is 0.5°C from 0°C to 85°C, and the resolution is 12-bit or 0.0625°C. The device also interfaces the controller with the I<sup>2</sup>C bus.

### 6.1.4 Power Management

The system has various supply voltage inputs and requirements summarized in Table 6.3, and the power flow is illustrated in Figure 6.1 by the red arrows. The supply voltage generated from the energy harvesting board is converted to be in the range of 2.15V to 3.6V. The main board including the SoC, accelerometer, and the ECG AFE is directly powered by this dynamic voltage input which almost meets the device requirements. A low-dropout linear regulator TPS78318 from Texas Instruments is used to regulate the 2.15V~3.6V to 1.8V for the sensing board.

**Table 6.3 Operation voltage range of the main components in the system.**

Component	IC	Operation Voltage Range	Operation Voltage in SCDPM
SoC	DA14580	0.9V~2V(boost) 2.15V~3.6V <sup>1</sup> (buck)	2.15V~3.6V
Accelerometer	ADXL362	1.6V~3.5V	2.15V~3.6V
ECG AFE	custom circuit	1.6V~5.5V	2.15V~3.6V
Light sensor	MAX44009	1.7V~3.6V	1.8V
Temperature sensor	PCT2202	1.65V~1.95V	1.8V
TEGs	SP5424-AC	-	0~0.35V
Solar cells	LL200-3-37 MP3-37	-	0~4.2V

Note 1: According to the experiment, the operation voltage range is wider than the datasheet.

The SoC DA14580 has both boost and buck mode concerning the provided voltage as shown in the table. In the experiment, we found that the power consumption of the chip in the buck mode is significantly less than the boost mode mainly due to the low efficiency of the DC-DC boost conversion. Therefore buck mode is configured, and the input voltage is thus decided to be 2.15V~3.6V. Along the increasing of the input voltage, the efficiency is reduced from 88% to 80%.

### 6.1.5 System Integration

The electrical and physical integration of the SCDPM platform is described in this part. Figure 6.5, Figure 6.6, and Figure 6.7 display the 3D board view in Altium Designer on the left side and the real PCBs on the right side. There are some jumper wires on the main board due to a few changes after manufacturing the board.

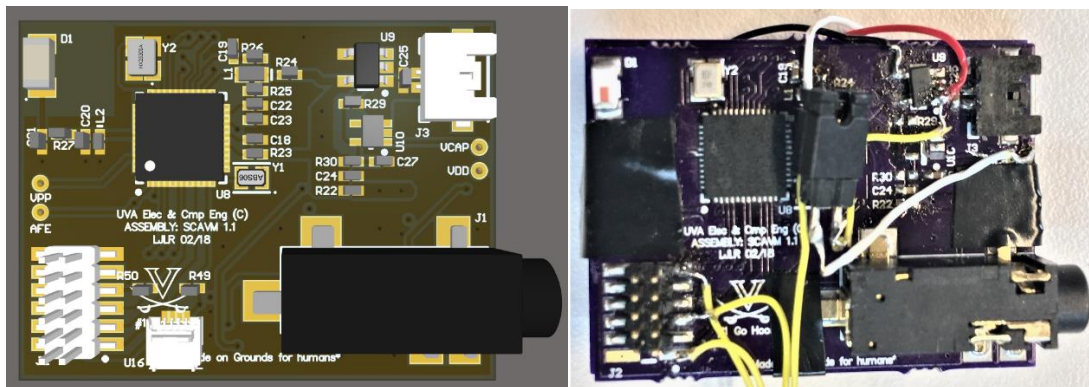


**Figure 6.5 The main board.**

The main board connects to an ECG cable using a 3.5mm Jack connector on the right bottom side. The JTAG connector on the left bottom side is used for programming and debugging with a computer. The main board is connected to the sensing board through an FFC connector on the middle bottom side and connected to the energy harvesting board through a 2-wire cable on the top right.

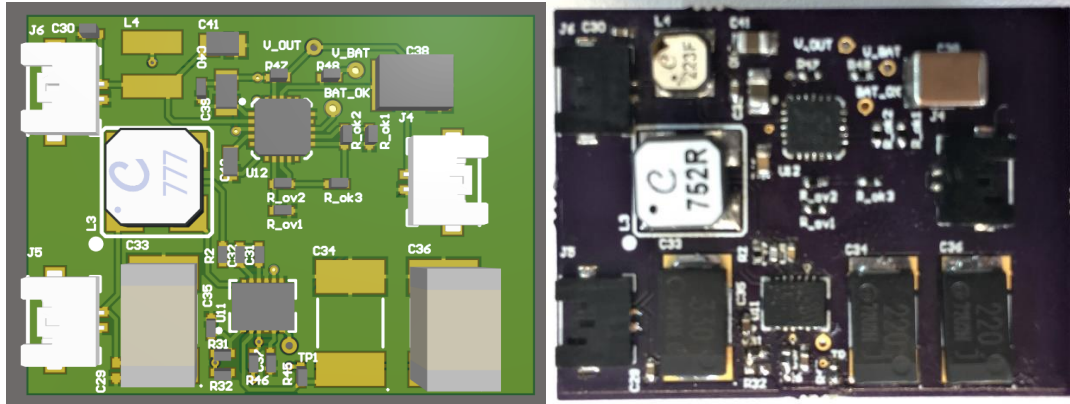


**Figure 6.6 The energy harvesting board.**

The energy harvesting board is connected to the solar cells using the top left connector and connected to the TEG array using the bottom left connector. It connects to the main board using the connector on the right side. The supercapacitor is attached to the bottom side of the energy harvesting board.

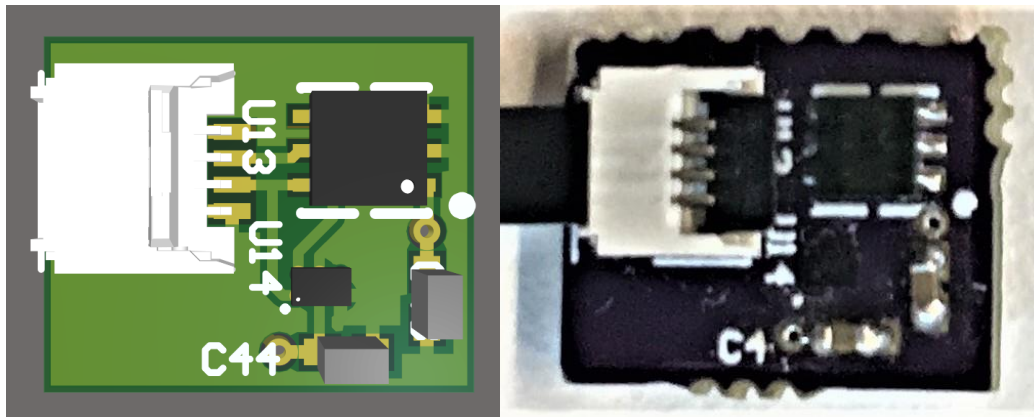


**Figure 6.7 The sensing board.**

The entire system is integrated into a running armband as shown in Figure 6.8. The solar cells are attached to the outside surface of the armband covering around 60% of the surface area. The TEG array traverses the outside surface of the armband, such that the hot side is attached to the human skin and the cold side with the heat sink is exposed into the air for heat dissipation. The sensing board is attached right above the solar cells for environmental sensing, as shown in the left figure. The main board and the energy harvesting board are put inside the armband.



**Figure 6.8 Physical integration with an armband.**

Figure 6.9 shows that a human subject is wearing the SCDPM platform on the left upper arm. The solar cells face outward from the body to receive more light and avoid being covered by the body trunk. The TEG array faces almost inward. The three ECG electrodes are attached to the chest under the shirt to collect the ECG signal. The total weight of the system including the armband is around 50g. The platform has been tested on the human body for more than 50 hours, and it is comfortable to wear as an ordinary running armband.

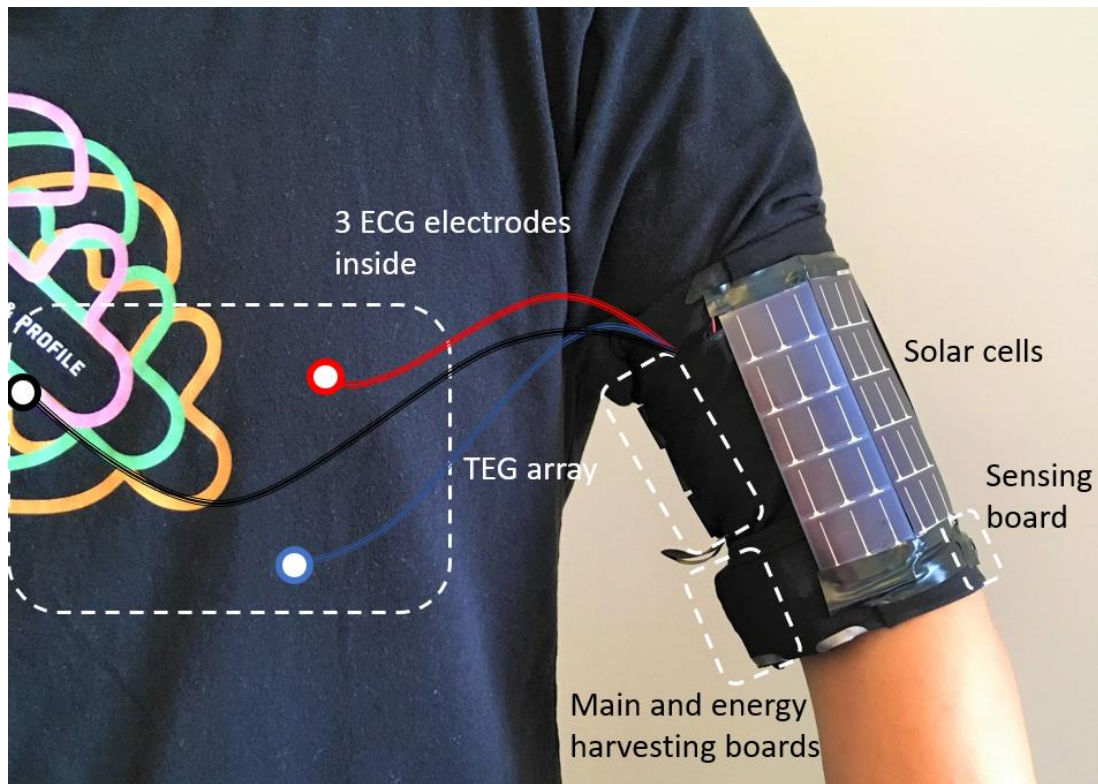


**Figure 6.9** Wearable system on the body. (ECG electrodes locations are not accurate)

## 6.2 Embedded Software Development for SoC

The primary target of the application on the SoC side is to collect sensor data and communicate with the phone through BLE. The application interfaces with each sensor for configuration and data sampling, and the sensor data is transmitted to the phone. The central part of the programming is the BLE related implementation including custom profiles definition based on Generic Attributes (GATT) and related event handlers.

The Dialog SoC is based on the ARM M0 core, and the development is in C programming environment. In this project, we use the ARM Keil  $\mu$ Vision IDE/Debugger with ARM C/C++ Compiler, and Segger ARM JTAG software stack. The DA1458x Software Development Kit (SDK) in its latest v5.0.4 release is employed in the project. The SDK contains an embedded

Operating System (OS), complete BLE stack, and various services and Application Programming Interfaces (APIs).

### 6.2.1 Software Platform Overview

The overall software architecture for the DA14580 SoC is illustrated in the diagram in Figure 6.10 which is based on their software user guide. From a high-level perspective, the architecture could be divided into three primary layers: the OS, the BLE stack, and the application.

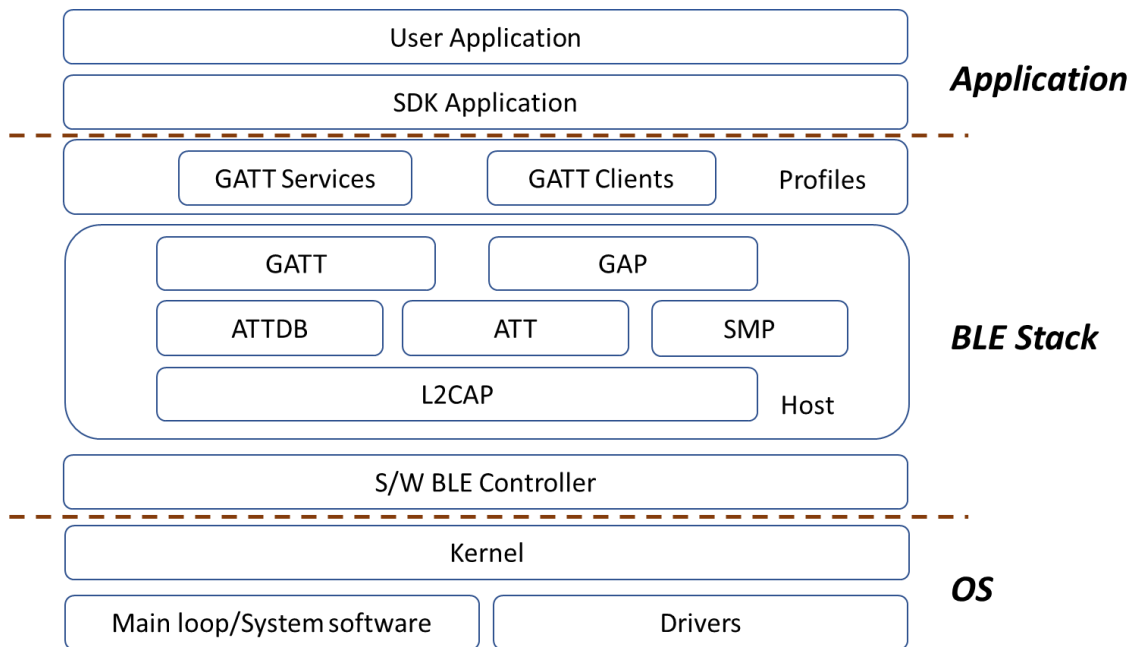


**Figure 6.10 Diagram of the DA14580 software architecture.**

The platform utilizes a small, efficient Real-Time Kernel (RTK) from Riviera Waves which provides most of the services for the BLE stack and applications. The event-driven kernel provides task, message, event, and memory management capabilities. Tasks communicate with each other using message queues and event queues, and the relevant event handler will be invoked when an event is triggered.

The SDK has complete BLE stack support including the sublayers of controller, host, and profiles. The Generic Attributes (GATT) define a hierarchical data structure that is exposed to

connected Bluetooth Low Energy (LE) devices [101]. It is a service framework that defines all procedures for using the Attribute Protocol (ATT) and describes in detail about data and profile exchange. The GATT profile has one or more services composed of characteristics, and a characteristic consists of a UUID, a value, a set of properties of available supported operations, and a set of permissions relating to security. Generic Access Profile(GAP) specifies the usage model of the lower-level radio protocols to allow BLE devices to discover devices, establish connections, manage connections, and exchange data, which focuses on the low-level interactions.

The user application on the top of the stack is responsible for implementing the custom profiles definition based on GATT, their data logic, user interface, and event handlers related to the data streams. The specific design of each part is discussed in the following parts.

### 6.2.2 Custom BLE Services Definition.

In the application, two custom services are created: Control and Sensor as shown in Table 6.4. The Control service is used for receiving the commands from the phone to change operating parameters, and the Sensor service integrates the collected sensor data and transmits to the phone.

**Table 6.4 Custom service definition.**

Custom service	Read/Write	Length	UUID
Control	Write	4 Bytes	0
Sensor	Read/Notify	20 Bytes	1

A command protocol is constructed on both SoC and Android side. The parser on the SoC side will decode the command from the phone and respond. Currently, there are four types of command patterns as illustrated in Table 6.5. The commands are at most 3 bytes long, including the command type from 0x00 ~ 0x03 and the followed option or parameters of 1 or 2 bytes.

The sensor data is stored in a buffer of 20 bytes, and when the buffer is full, it will be put in a packet and transmitted to the phone. Then the data could be accessed from the Sensor service.

**Table 6.5 Command pattern.**

<b>Command Type (code)</b>	<b>Option/Parameter</b>
<b>Stream(0x00)</b>	Start(0x00)   Stop (0x01), 1 Byte
<b>Change_SamplingRate (0x01)</b>	New sampling rate(10ms), 2Bytes
<b>Change_ConnPara(0x02)</b>	New connection interval (ms), 2Bytes
<b>Change_DataScheme(0x03)</b>	New scheme, 1 Byte

### **6.2.3 Device Driver**

Four types of sensors interface with the SoC with different protocols as shown in previous Table 6.2, and drivers are required to access the devices. The driver functions include device configuration, data access, and auxiliary functions like part number reading. The ECG AFE is directly connected to the ADC of the SoC without the need for a driver. Similarly, the voltage on the supercapacitor is measured from an internal ADC channel.

The ADXL362 accelerometer communicates with the SoC through SPI. The device is configured as an 8-bit data output,  $\pm 2g$  range. The PCT2202 temperature sensor and MAX44009 light sensor communicate with the SoC through I<sup>2</sup>C, and the address of them are configured as 0x48 and 0x4A, respectively. Both sensors could be configured as 1 Byte or 2Byte data mode.

### **6.2.4 Data Schemes for Use Cases**

To efficiently transfer the data, we fill the 20 bytes data buffer. In each packet, the data load is 20 bytes. Android does not support MTF more than 20 bytes.

For different use cases, six data schemes are designed. We term *data scheme* to refer the way that data from different sensors are sampled, the quantization depth, and the organization in a packet. The various data schemes are designed to enable efficient data collection in different use cases. For instance, when the system is used as a motion tracker, only the acceleration data is collected and transmitted, and when the system is used as an ECG monitor, only ECG data is

collected. In some other cases, data from all the sensors are collected but could be at a different sampling ratio.

The user could dynamically change the data scheme by sending specific commands to the system. On the SoC side, the application will listen to the incoming commands and parse them. If the command is to request changing data scheme, then the timer handler relevant to the scheme will be invoked and take effect. The details of each scheme are described below.

**Scheme 0** collects data from all sensors including ECG, acceleration, light, temperature, and voltage on the supercapacitor. The temperature is 12 bits long but occupies 2 bytes, and other sensors are 1-byte long. The sampling sequence detail is shown in Table 6.6.

**Table 6.6 Sampling sequence of scheme 0.**

Time slot	Sensor
0	ECG
1	ECG
2	ECG
3	ECG
4	ECG, accel
5	ECG
6	ECG
7	ECG
8	ECG
9	ECG, accel, vol, temp, light

**Scheme 1** also collects data from all sensors. In this scheme, the quantization depth of ECG is 10 bits. The temperature is still 12 bits long and occupies 2 bytes, and other sensors are 1-byte long. The sampling sequence detail is shown in Table 6.7.

**Table 6.7 Sampling sequence of scheme 1.**

Time slot	Sensor
0	ECG
1	ECG
2	ECG
3	ECG, accel
4	ECG
5	ECG
6	ECG
7	ECG, accel, vol, temp, light, ECG-LSB

**Scheme 2** is used as a motion and environment profiler which functions like the EHDC discussed in Section 3.3. It collects all sensor data except the ECG. The light, temperature, and voltage are all configured as 12-bits long to have better accuracy. The sampling sequence detail is shown in Table 6.8.

**Table 6.8 Sampling sequence of scheme 2.**

Time slot	Sensor
0	accel
1	accel, vol
2	accel
3	accel, vol, temp, light

**Scheme 3** is used as a motion tracker which only collects the three-axis acceleration data.

**Scheme 4** is used as an ECG monitor which only collects ECG data with the quantization depth of 10 bits. The sampling sequences are omitted for Scheme 3 and 4.

**Scheme 5** collects data from ECG, acceleration, and voltage. This scheme is used for systems without the sensing board, or when the light and temperature information is not of interest. The sampling sequence detail is shown in Table 6.9.

**Table 6.9 Sampling sequence of scheme 5.**

Time slot	Sensor
0	ECG
1	ECG
2	ECG, accel
3	ECG
4	ECG
5	ECG, accel
6	ECG
7	ECG
8	ECG, accel
9	ECG, vol

### **6.3 Android Application Development**

The primary targets of the application on the phone side include:

- a) Communicate with the sensor system through BLE. The phone sends commands to the sensor system for dynamic configuration and receives the collected sensor data.
- b) User interface. The phone has a Graphic User Interface (GUI) for user input and real-time display of the sensor data.
- c) Dynamic power management and energy prediction algorithms implementation. The energy prediction algorithm proposed in 4.2 and the online DPM scheduling algorithm in 5.5 are implemented on the phone in Java.
- d) Data storage, processing, and cloud service. The sensor data could be stored locally or uploaded into a remote cloud server for further processing. The phone side application is responsible for storage and cloud interface management.

The Android application is developed in Android Studio and tested on a Samsung smartphone with Android 6.0 version. An overview of the application.

**Table 6.10 An overview of the Android application**

<b>Item</b>	<b>Number</b>
Packages	6
Classes	25
Interfaces	2
Application size	23.9MB

### **6.3.1 User Interface**

The GUI is the central part of the application which is used for receiving user input for system connection and configuration, and for sensor data display. A screenshot of the application when it is running is displayed in Figure 6.11. The user could configure the system parameters including data schemes, sampling rate, connection parameters, and power management option. The sensor data of ECG, acceleration, the voltage on the supercapacitor, temperature, and light intensity are displayed in real-time. The androidplot library [102] is used to plot the real-time data series. As shown in the figure, the system is running with scheme 1, with the ECG sampling rate of 50Hz and connection interval of 80ms. The ECG waveform is clearly presented with 50 Hz and 10 bits long. The acceleration data in the second figure is sampled at 25Hz. The voltage on the supercapacitor, light, and temperature are displayed in the following three plots with lower sampling rates.

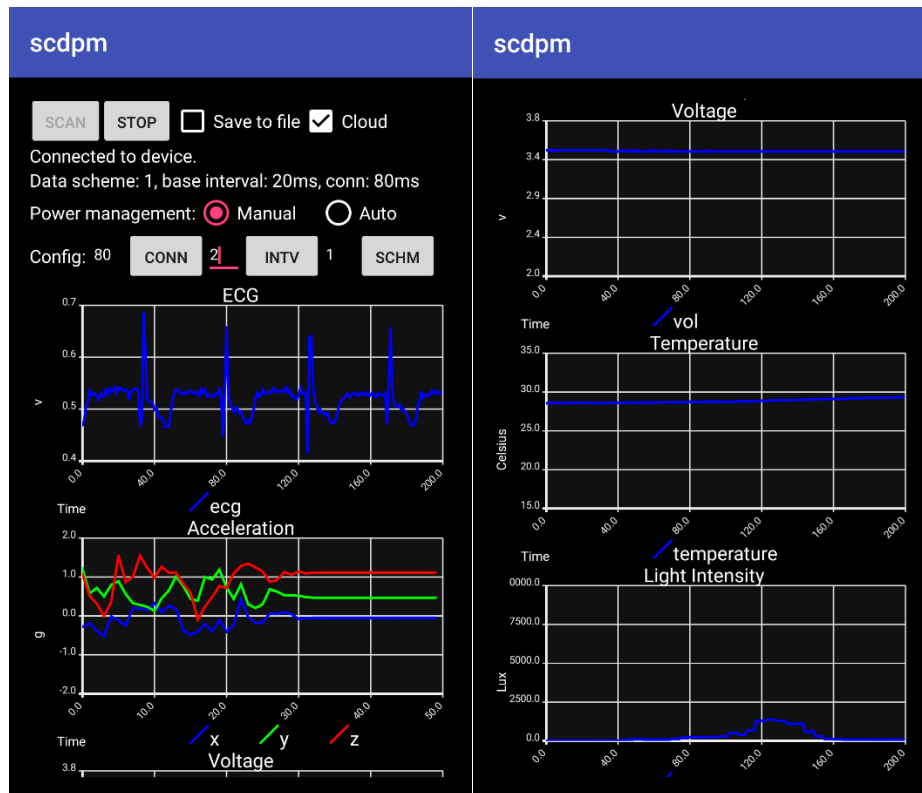


**Figure 6.11 Screenshot of the Android application running. The user could configure the system parameters including data schemes, sampling rate, connection parameters, and power management option. The sensor data of ECG, acceleration, the voltage on the supercapacitor, temperature and light intensity are displayed in real-time.**

### 6.3.2 Communication

A Communication class is designed for managing the BLE connection with the system, and data exchange. Callback functions are designed to receive the data packets from the sensor system and to send commands the system.

### 6.3.3 Context Manager

Besides the context information from the SCDPM platform, the smartphone also provides useful context which could improve the energy harvesting prediction as discussed in Section 4.2. In this work, we limit the context discussion to the three types: weather forecast, calendar events, and GPS.

**Weather forecast.** Assuming the smartphone has an internet connection, the weather forecast could be accessed conveniently. In this work, we employ the free weather forecast service from AccuWeather[103]. Specifically, we use their locations APIs to detect the user’s place and utilize the forecast APIs to acquire the weather forecast information. The forecast has different horizons, from hours to days, and we mainly use the hourly data.

The forecast API returns data in JSON format containing a timestamp, temperature, and weather icon. A typical weather result is shown in Figure 6.12. The weather icon is employed to estimate the sunlight intensity for outdoor solar energy harvesting. There are as many as 44 weather icons which could provide an accurate estimation of the sunlight intensity. Temperature could be utilized to predict thermoelectric energy harvesting. The Android application processes such weather data to extract useful information then push into the prediction model.

```
[
  {
    "DateTime": "2018-02-17T04:00:00+08:00",
    "EpochDateTime": 1518811200,
    "WeatherIcon": 34,
    "IconPhrase": "Mostly clear",
    "IsDaylight": false,
    "Temperature": {
      "Value": 23,
      "Unit": "F",
      "UnitType": 18
    },
    "PrecipitationProbability": 0,
    "MobileLink": //omitted
    "Link": //omitted
  },
  ...
]
```

**Figure 6.12 An example of the weather forecast data in JSON format.**

Currently, we utilize the hour number, temperature, and weather icon as “useful information” for the prediction model. For example, the result of the 12 hours forecast for Charlottesville, VA, from 3 pm to 2 am is listed below. The weather icon code 2 is for “most sunny”, 1 for “sunny”,

and 33 for “clear”. Technically, we only need to predict the daytime weather when the light intensity is sufficient.

**Table 6.11 A weather forecast result example.**

<b>Time</b>	<b>3pm</b>	<b>4pm</b>	<b>5pm</b>	<b>6pm</b>	<b>7pm</b>	<b>8pm</b>	<b>9pm</b>	<b>10pm</b>	<b>11pm</b>	<b>12am</b>	<b>1am</b>	<b>2am</b>
Icon	2	2	2	2	2	1	33	33	33	33	33	33
Temperature (°F)	80	81	80	79	77	75	71	69	67	65	64	63

**Calendar.** Calendar events could be used to predict the user’s behavior especially for predicting indoor or outdoor environment, and the specific indoor location. With the permission of accessing the user’s calendar, a list of future calendar events could be acquired as a `CalendarContract.Instances` [104]. From the instance, we could get the related information of the event including the place, description, time start/end, and duration. The information related to the place and time is utilized by the prediction model.

Here we maintain an enumerable places list and assume that we could directly extract the place name from an event description. For instance, “Gym”, “UVa Hospital”, “Rice Hall 304”, “Home”, or others. Extracting such information from a complex sentence may require natural language processing related methods, and they are out of the scope of this work. As discussed before, a light profile is also stored for each place.

**GPS.** The GPS provides information about the place, and the moving speed of the user as well. The place information could be used with the calendar information to decide the indoor/outdoor situation and places. The GPS information processing is not fully implemented, but the method of getting the raw GPS information is implemented.

### **6.3.4 Energy Harvesting Prediction and DPM Scheduling**

The DPM algorithm is discussed in the previous section. Primarily, the online version with a supercapacitor capacity limit is employed. In the application, the time slot is selected to be the 30s. In each time slot, the energy prediction will be updated and then execute the scheduling algorithm.

After calculating the operating parameters including the sampling rate and connection interval, the phone sends the new configuration command to the SCDPM system to be reconfigured.

### **6.3.5 Local and Cloud Data Storage**

The sensor data could be stored locally or uploaded to a remote database using cloud services. When the data is stored locally, the data format is CSV which is more accessible for processing. Every 1 hour, a new folder with the name of the UNIX timestamp will be created, and the data files for each sensor is created as well.

. The data could be uploaded to a database in a remote cloud server for better performance. In this project, the InfluxDB database from InfluxData is utilized for storage, and Amazon AWS cloud service is selected. InfluxDB is a custom high-performance Time Series Database(TSDB) optimized for time series data storage including IoT sensor data, application instrumentation, and real-time analytics. Therefore, it matches well the requirement for real-time multi-sensor data sensing in the BSN area. The InfluxDB provides high performing write and query HTTP APIs which are convenient to interface with other services and platforms. The APIs are utilized by the Android application for uploading the sensor data and utilized by data visualization service to display the data in real time.

The opensource platform Grafana is utilized for data visualization. Grafana works with InfluxDB seamlessly to display the data and execute the query in real time.

The InfluxDB and Grafana services are running on the Amazon server. The sensor data is stored in Influx on the server, and the Grafana panels could be viewed by any devices with granted permission.

The data visualization on the cloud side is shown in Figure 6.13. There are five panels for real-time display of ECG, motion, the voltage on the supercapacitor, light intensity, and temperature. The viewer could zoom in or out of the data series and change the refresh rate of the plot. In addition, custom alerts could be configured for the data series.

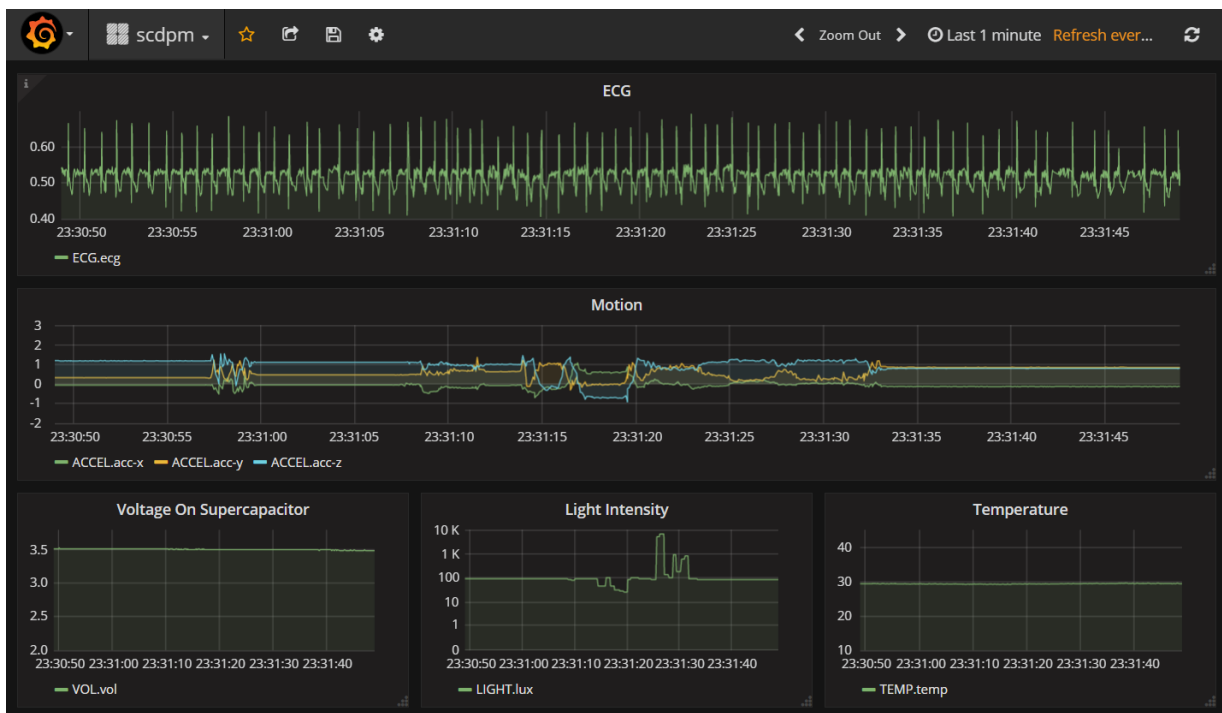


**Figure 6.13 Screenshot of the cloud application. The sensor data of ECG, acceleration, the voltage on the supercapacitor, temperature and light intensity are displayed in real-time.**

**The viewer could change the time range, refresh rate, and zoom in/out.**

## 6.4 Power Consumption Modeling

Accurately model the power consumption of the entire system is essential for dynamic power management. By modeling the power consumption under different operating modes, the schedule could select the appropriate operating mode according to current energy status.

The basic idea of changing the power consumption of the whole system is to adjust the duty cycling of the SoC, in other words, deciding the active period and sleep period. The peak power consumption of the SoC during BLE transmission is around 10mW, and it is around 2mW in active mode without BLE transmission when collecting and processing data and running tasks. Compared with such high-power consumption, it consumes only 6.9 $\mu$ W during sleep mode. Therefore, the overall power consumption could be reduced by changing the duty cycling of the SoC. Other components of the system are using ultralow power electronics and consume around 100 $\mu$ W in total when active. The quiescent current of most of the sensors are pretty low, so they are not duty cycled externally. The power consumptions of the main components in SCDPM are listed in Table 6.12.

**Table 6.12 Power consumption of each component.**

Sensor	Power <sup>1</sup> ( $\mu$ W)
Accelerometer	4.6
ECG	67.0
Light	1.2
Temperature	54.0
SoC (sleep)	6.9
SoC (active)	2640
SoC (BLE transmission)	16500

Note: 1, Some power numbers are calculated from datasheets when cannot be directly measured.

### 6.4.1 Current Consumption Profiling

The SoC has three main operation modes: sleep, active, and active with BLE transmission. The detailed power consumption profile in each mode is studied in SmartSnippet and experimented using an oscilloscope. The SmartSnippet is a software tool from Dialog which can profile the real-time power consumption at a high frequency of 105kHz. Figure 6.14 illustrates the detailed current consumption during operating. When the SoC wakes up from sleep mode, there will be a peak

current for charging decoupling capacitors, and then around  $1\mu\text{A}$  current for memory operations. After the initialization, the SoC will execute tasks consuming around  $0.8\mu\text{A}$ . If a connection event happens in the period, there will be additional current consumption as high as  $5\text{mA}$  for BLE operation as shown by the orange curve. The number of current spikes depends on the number of packets that are transmitted during the connection event. The total length of such an active period with or without BLE transmission depends on the task load. We also measured the current consumption of the whole system using an oscilloscope as shown in Figure 6.15 and the results are similar.

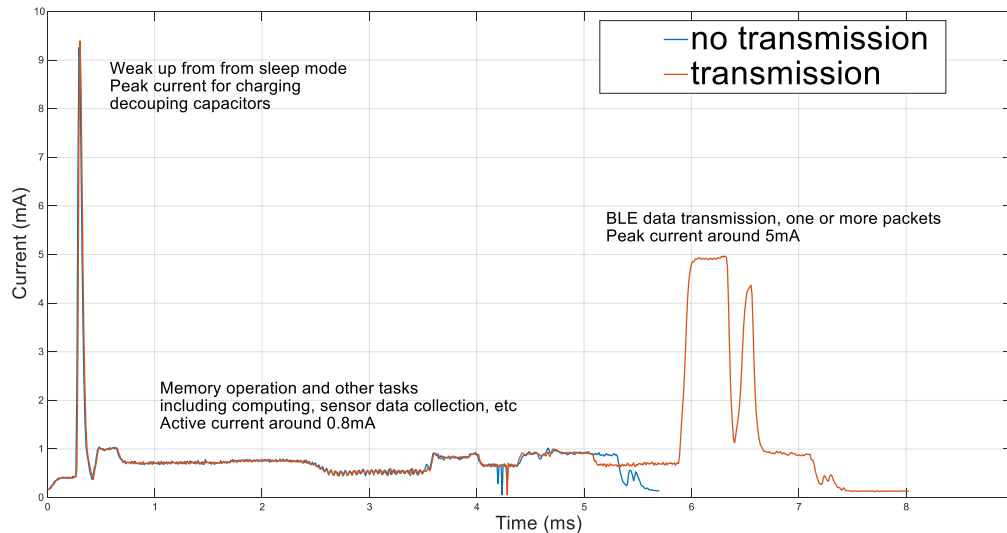


**Figure 6.14** Current consumption profiling using SmartSnippet. The blue curve shows the active mode without BLE transmission and the orange curve with BLE transmission.

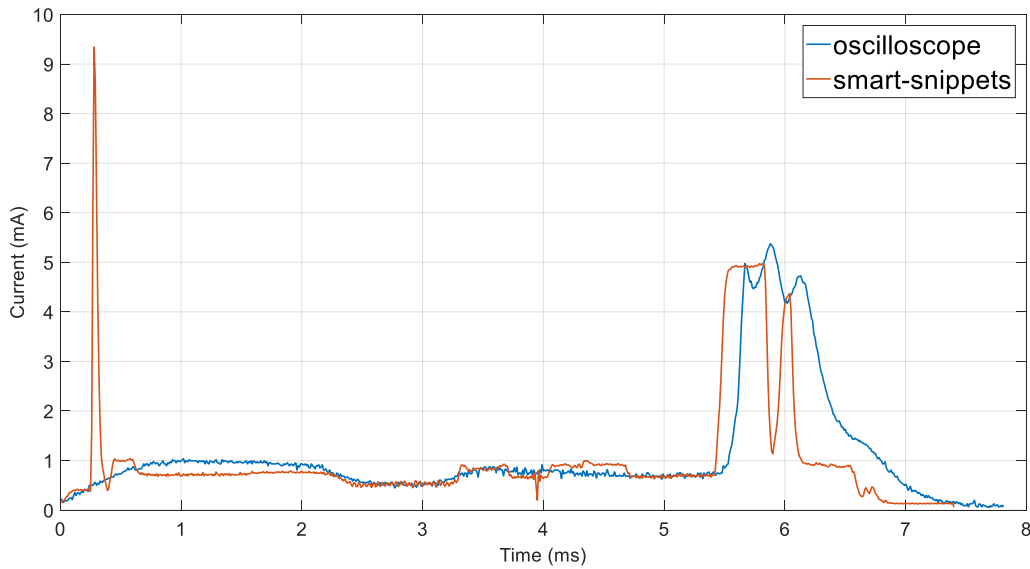


**Figure 6.15 Comparison of current consumption profiling by using SmartSnippet and an oscilloscope.**

The workload fluctuation of the system during operation is modeled as shown in Figure 6.16. Figure 6.17 illustrates the actual power profile while the system is running using an oscilloscope. The SoC will wake up from sleep mode to active mode periodically to sample data from sensors, and the data is stored in a 20 bytes buffer. When the buffer is full, it will be dumped into a data packet, and the packet will be transmitted to the phone during the next BLE connection event. During each connection event, there could be one to up to four packets sent. The radio could transmit data as infrequent as possible to save power, provided that all data be transmitted. If the data cannot be transmitted due to large connection interval for a long time, the SoC will crash due to kernel message queue overflow.

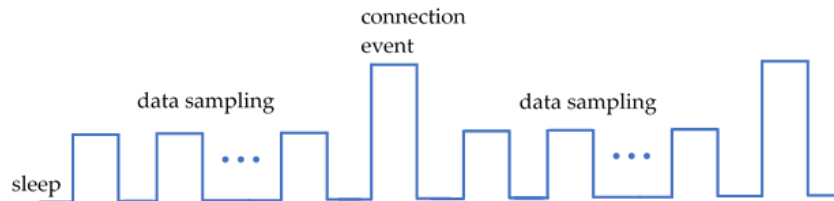


**Figure 6.16 Workload change during normal operations. There are roughly three levels of power consumption: sleep, active, and data transmission.**

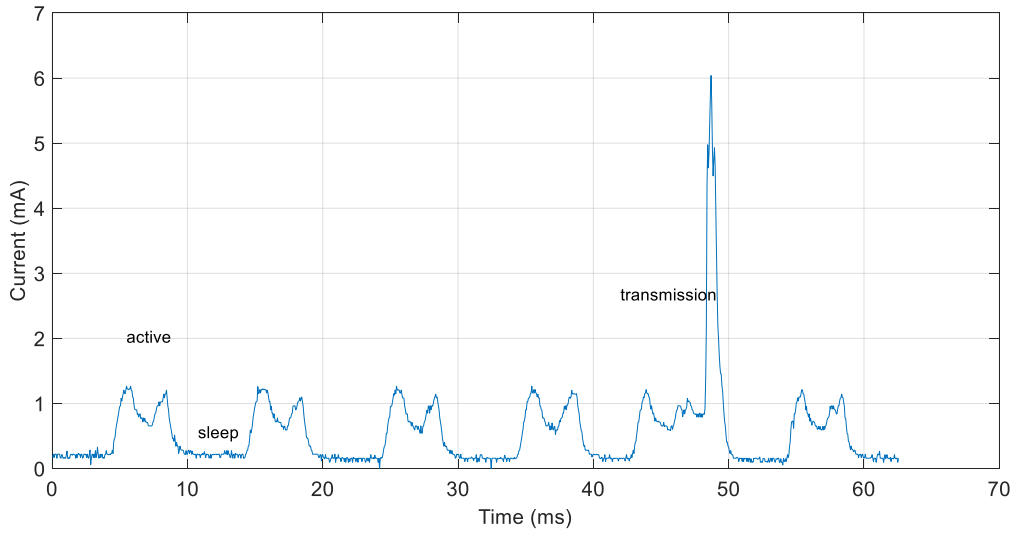


**Figure 6.17 Workload change during operation. The curve was plotted using data collected from an oscilloscope.**

### 6.4.2 Power Consumption Modeling

The primary energy consumption of the SC-DPM consists of sensors and SoC, among which the SoC dominates the total power consumption when active. The SoC power consumption consists of three modes: sleep, active and sampling, and active and transmitting. The energy model could be expressed as below.

$$P = P_{SENSOR} + P_{SoC} \quad (6.1)$$

The  $P_{SoC}$  is decided by the duty cycling of the SoC and the BLE transmission frequency. Since the SoC can only collect data during the active period, the sampling rate of sensors is promotional to the duty cycling and is directly related to  $P_{SoC}$ . The connection interval is decided according to the data rate which relates to the sampling rate as well. The power consumptions of active, active with BLE transmission, and during sleep are denoted as  $P_a$ ,  $P_t$ , and  $P_s$ . The connection interval is defined as  $T_c$ . The period of active and BLE transmission are denoted as  $T_a$ , and  $T_t$ , respectively.  $T_a$  and  $T_t$  depend on the task load of the SoC and the data load. In the application, the timing parameters are measured and could be considered as static although not strictly static. If the sensor

samples are evenly distributed, there should be at most one sample in each active period. In other words, the sensor sampling rate  $f$  is at most the frequency of active operation. The power consumption of the system is:

$$P_{SoC} = \frac{fT_cT_aP_a + T_tP_t + (T_c - T_t - fT_cT_a)P_s}{T_c} \quad (6.2)$$

$$P = P_{SENSOR} + \frac{fT_cT_aP_a + T_tP_t + (T_c - T_t - fT_cT_a)P_s}{T_c} \quad (6.3)$$

The constraint of connection interval  $T_c$  is that it should be short enough to transmit all the sampled data through BLE. According to the Bluetooth specification,  $T_c$  should be in the range of 7.5ms to 4 seconds [48]. But smartphone OS such as Android and iOS have their own constraint, and even different OS versions has different constraints. For Android, here we set:

$$15ms \leq T_c \leq 4s \quad (6.4)$$

The number of packets that can be transmitted during a connection event also depends on the OS, and here assuming during each connection event, there are at most four packets transmitted for the Android systems [105]. The data rate, packet rate, and packet length (in bytes) are denoted as  $D_r$ ,  $K_r$ , and  $L$ , respectively. Assuming the average data length sampled during an active period is  $n$ , then

$$D_r = LK_r = fn \quad (6.5)$$

$$K_r \leq 4 \frac{1}{T_c} \quad (6.6)$$

Therefore:

$$15ms \leq T_c \leq 4 \frac{L}{fn} \quad (6.7)$$

When the sensor sampling rate is higher than  $(T_c - T_t)/(T_c T_a)$  the chip cannot enter sleep mode at all and will stay in active mode. The power will increase along the sampling rate for data transmission.

$$P_{SoC} = \frac{P_a(T_c - T_t) + T_t P_t}{T_c} \quad (6.8)$$

$$P = P_{SENSOR} + \frac{P_a(T_c - T_t) + T_t P_t}{T_c} \quad (6.9)$$

The values of the parameters in the model are measured which are summarized in Table 6.13.

**Table 6.13 Parameters measured or assigned.**

Parameter	Value
$P_{SENSOR}$	126.8 $\mu$ W
$P_a$	2640 $\mu$ W
$P_t$	3960 $\mu$ W
$P_s$	6.9 $\mu$ W
$T_a$	5.7ms
$T_t$	7.3ms
$L$	20
$n$ (scheme 0)	2

Assuming  $T_c = 4 \frac{L}{fn}$ , the relationship between the power consumption and the sample rate is shown in Figure 6.18. The power consumption is under 1mW when the sampling rate is 50Hz. When the sampling rate is higher than 175Hz, the SoC will be active all the time without entering sleep mode. The SCDPM is among the state-of-the-art lowest power consumption systems.

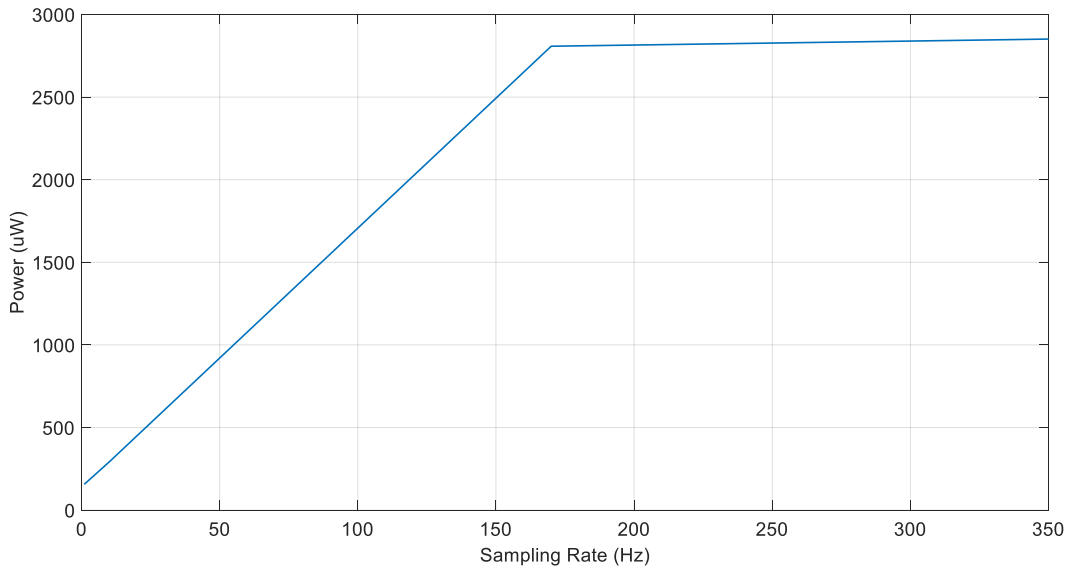


**Figure 6.18 Power Consumption versus sampling rate.**

## 6.5 Summary

This chapter described the design of the custom SCDPM system as a self-powered context-aware DPM sensing platform. Compared with the EHDC platform, this platform targets for health monitoring with ECG, motion, and environment sensing capabilities. While EHDC is mainly for energy harvesting profiling without the ECG capabilities and it is battery-powered since it is based on a Raspberry Pi board. Regarding the size, the SCDPM is much smaller and convenient for wearing.

**Table 6.14 Comparison between EHDC and SCDPM.**

Platform		EHDC	SCDPM
Sensors	Light	√	√
	Temperature	√	√ <sup>4</sup>
	Motion	√	√
	ECG	×	√
Harvesters	TEG	√	√
	Solar	√	√
Controller/SoC		Raspberry Pi 0/2/3	DA14580

<sup>4</sup> EHDC uses two temperature sensors to collect temperature of skin and the ambient air. SCDPM only has one to measure the air temperature.

Energy measurement	√	× <sup>5</sup>
Self-powered	×	√
Dimension <sup>2</sup>	2.7in×2.6in×1.0in	1.30in×0.99in×0.6in
Data storage	Local SD card/cloud <sup>6</sup>	Phone/cloud
Purpose	Profiling	Health monitoring, profiling, DPM
DPM	×	√

We compared our work with other state-of-the-art sensing systems with ECG monitoring functions. Some of the platforms have motion or context sensing as well, as shown in [106]–[110] others are only for ECG. Most of the other platforms have a higher sampling rate of ECG signal for general ECG collection. However, we demonstrate 50Hz is sufficient for vigilant monitoring which is still capable of accurately calculating the R-R interval, and our platform is also capable of higher sampling rates.

Our platform achieves the least power consumption of all. In the “Power ratio” row, we calculated the power consumption of our platform running at the same frequency as each other ones and listed the ratio. From that row, we could see that our platform consumes 3.2%~82.2% of other platforms. The work in [108] is quite different, and they achieved an ultra-low power consumption of 137  $\mu$ W, however, by employing an extremely low duty cycling. The operation period of the system is 12.5 minutes including 0.5 minutes for monitoring, evaluation, data transmission and 12 minutes at a lower energy level hibernation, and the system repeats it periodically. Though it could be considered as “continuous” sampling, it is not vigilant since it may miss many critical events in the incredibly long 12 minutes.

---

<sup>5</sup> The SCDPM measures the battery voltage rather than the energy harvested as in EHDC.

<sup>6</sup> The cloud function is available if there is internet connection. Pi3 with WiFi has to be used.

**Table 6.15 Comparison of low power, wearable, health monitoring systems including ECG.**

	[106]	[107]	[108]	[111]	[109]	[110]	[112]	<b>This Work</b>
Number of ECG leads	2	3	3	3	4	3	2	3
Motion	Yes	Yes	Yes	No	Yes	Yes	No	Yes
Environmental sensing	No	No	Yes	No	Yes	No	No	Yes
ADC (bits)	8	n/a	12	16	24	12	16.5 (14 ENOB)	10
$f_{\text{ECG}}$ (Hz)	300	n/a	200	500	500	750	320	50 <sup>7</sup>
Voltage (V)	3.7	3	3	1.8	3	3.3	3	2.1~3.6
Power ( $\mu$ W)	n/a	12500	137	6500	90000	13400	12000	942 <sup>8</sup>
Power ratio <sup>9</sup>	n/a	n/a	0.822	0.444	0.032	0.220	0.237	1
Communication Protocol	BT	BT	BLE	BLE	BT	BLE	ZigBee Pro	BLE
Cloud Access	Yes	No	No	No	No	Yes	Yes	Yes
Continuous Operation	Yes	Yes	Yes <sup>10</sup>	n/a	Yes	Yes	Yes	Yes
Vigilant Operation	Yes <sup>2</sup>	Yes <sup>2</sup>	No	n/a	Yes <sup>2</sup>	Yes <sup>2</sup>	Yes <sup>2</sup>	Yes
Data Storage	Local/Remote	Local	Remote	Remote	Local/Remote	Local/Remote	Remote	Phone/Remote
Power Source	Battery (48 hrs)	Battery (30 hrs)	TEG (Self-powered)	Battery	Battery (5 hrs)	Battery (96 hrs)	Battery (160 hrs)	Photovoltaic (Self-powered)
Adaptive Sampling/DPM	No	No	No	No	No	No	No	Yes
Dimensions (mm)	90 x 40 x 16	58 x 50 x 10	60 x 32 x n/a	24 x 14 x n/a	30 x 25 x 10	13 x 11 x 5	65 x 34 x n/a	30 x 23 x 25

In terms of dynamically adjust the operation parameters, all others are not capable of this and only run at a fixed sampling rate. Our SCDPM could adjust sensor sampling rates, connection intervals, and data scheme dynamically or manually to adapt the energy availability.

To sum up, this chapter demonstrated our custom SCDPM platform performs better than state-of-the-art sensing systems regarding system power consumption and the capability of dynamic power management and adaptive sensing. The platform is utilized to make vigilant health monitoring in the real-world as discussed in the next chapter.

<sup>7</sup> The system could sample ECG at different frequencies, and the power number here is at 50Hz.

<sup>8</sup> The number includes power consumption of motion, light, voltage, and temperature sensing.

<sup>9</sup> We compared the power consumption when the proposed work runs at the same frequency with each work and computed the ratio.

<sup>10</sup> The continuous operation has an extremely low duty cycling.

# **7 Validation of Context-aware Dynamic Power Management on SCDPM**

As the last section of this work, we presented the results of the SCDPM platform as a validation of the work. Section 7.1 describes the profiles that collected on the human subject in the real world for more than 50 hours in total, and the longest period is around 11 hours. Continuous collecting data on a human subject in the real world could validate that the proposed SCDPM platform performs well on the health and environmental monitoring with low power consumption. The system could be powered in the daytime. In Section 7.2, the details of the ECG and motion data is analyzed. In Section 7.3, the energy harvesting prediction model is discussed. Since there are not similar related work to compare, we calculated the RMSE of the prediction. Section 7.3 discusses the simulation for online DPM scheduling.

## **7.1 Data Collection Using SCDPM.**

We used the SCDPM for long-term continuous data collection in the real-world to validate its functionalities. One human subject wore the SCDPM armband with three ECG electrodes on the chest. All the sessions were using scheme 1 to collect data from all the sensors. The total length is

more than 50 hours, and the longest continuous profile that collected is around 11 hours from 8:35 am to 6:55 pm. We selected sampling rates from 20Hz to 100Hz during the data collection, and the sampling rate was fixed during each session except the last one for validating energy prediction and adaptive sensing.

**Table 7.1 An overview of collected profiles.**

<b>Session</b>	<b>Length (hours)</b>	<b>ECG sampling rate (Hz)</b>	<b>Indoor percent (%)</b>
1 (sunny)	8.73	50	83.46
2 (cloudy)	10.36	33.3	83.26
3 (rainy)	9.11	25	94.88
4 (indoor-1)	0.60	100	100
5 (indoor-2)	0.96	50	100
6 (indoor-3)	1.09	33.3	100
7 (indoor-4)	1.58	25	100
8 (indoor-5)	1.91	20	100
9 (night)	2.27	33.3	89.22
10 (full)	1.09	33.3	6.12
11 (afternoon)	5.22	50	88.51
12 (dynamic)	9.15	dynamic	84.01
<b>Total:</b>	<b>52.07</b>	-	-

In the following sessions, we first described three typical profiles in a hybrid indoor and outdoor environment in different weather conditions, and then profiles collected at home to test the operation time with almost no energy harvesting.

For each profile, we show the voltage on the supercapacitor, light intensity, temperature, and motion using the Teager[56] calculator. We scale the values as shown in the legend to fit all curves in a single figure.

### 7.1.1 Profiles in Various Weather Conditions

The profile collected on a sunny day is presented in Figure 7.1. Since it was sunny in the morning, a relatively high sampling rate was selected as 50Hz. In the morning from 8:16 am to 9:20 am, the subject was walking outdoor, then stayed in the office until noon. The light intensity in the meeting room is around 300~500, which provides little energy and the voltage dropped. The following two spikes around 12:00 pm were due to going outdoor for returning home for lunch by bus, and the low light intensity between the two spikes were on the bus with the duration of around 20 minutes. The subject was at home at 12:30 pm ~ 13:10 pm and the voltage kept dropping. Then two outdoor periods were outdoor from home to the office. Tough these outdoor periods were at noon, it was cloudy at that time, and the light intensity was lower than in the morning. The afternoon periods were most inside the office until going to a gym at 3:40 pm. The motion spike around 5 pm was due to the running, followed by some strength exercises. On the way from the gym to the office at around 4:25 pm, it was showering, and the light intensity was serval hundreds. The system ran until powering down until around 5:00 pm.

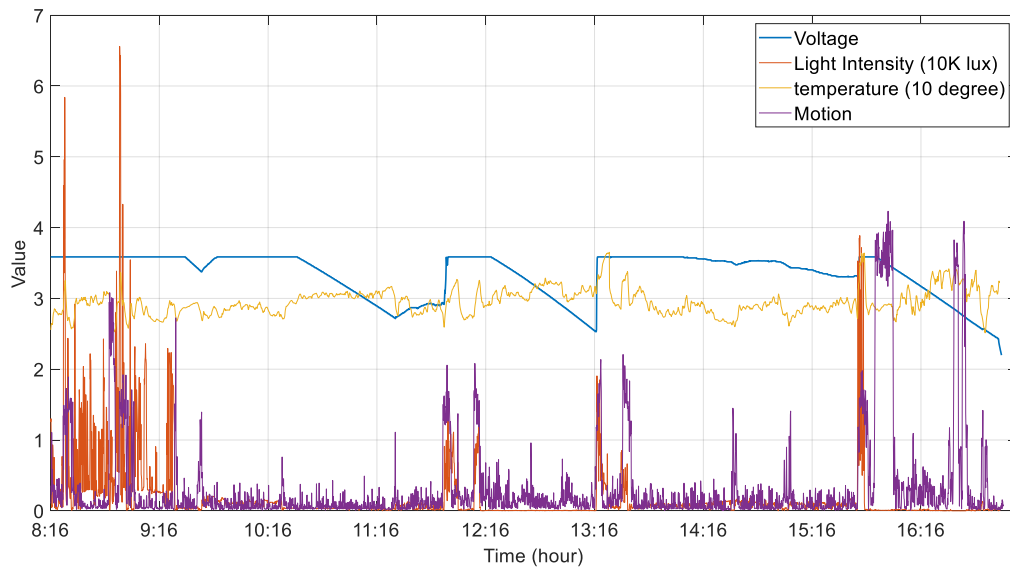


**Figure 7.1 A profile collected on a sunny day.**

The profile collected on a cloudy morning is presented in Figure 7.2. The sampling rate was selected as 33.3Hz since it was cloudy in the morning. The light intensity increased from 9:00 am to 11:00 am due to the weather change, and the supercapacitor was fully charged. Similar to the previous profile, there were two outdoor periods for going out for lunch. In the afternoon, the light intensity was around 2000 lux which kept the supercapacitor fully charged for the entire afternoon. The two spikes around 17:35 pm were due to heading home by bus. The system was powered down at home at around 7 pm.

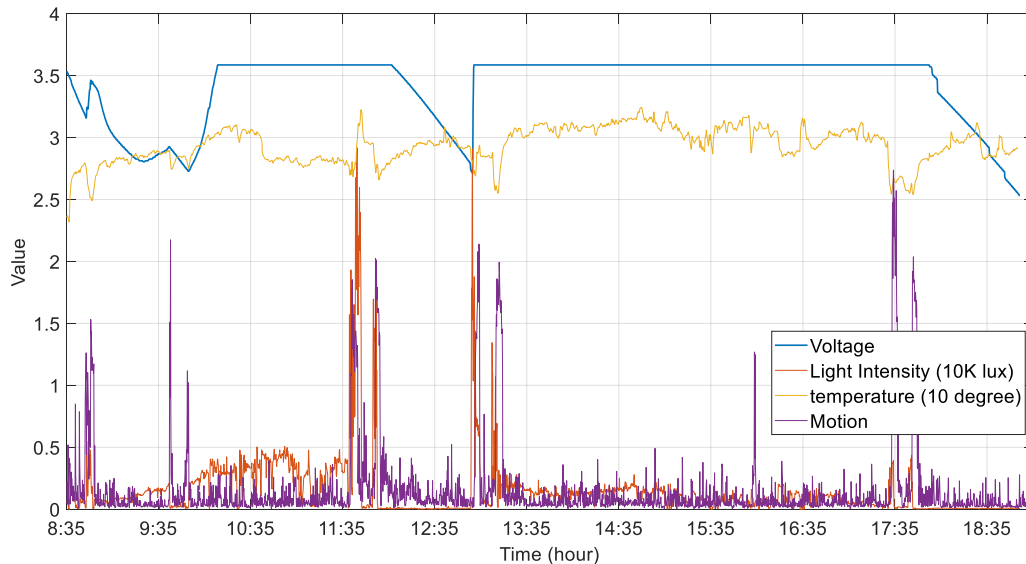


**Figure 7.2 A profile collected on a cloudy day.**

The profile on a rainy day is illustrated in Figure 7.3. Unlike the previous two profiles, the supercapacitor was not fully charged for most of the time. Even outdoor, the light intensity was still less than 5000 lux, and the supercapacitor was charging slowly. Still, there were two outdoor periods for lunchtime, while the light intensity was around 2000 lux~4000 lux. From 3:40 pm to 4:20 pm, the subject went to the gym for running and strength exercises. When going out, the temperature decreased as shown around 10:30 am, 12:30 pm, and 15:40 pm. The system kept running indoor in the office till 17:40 pm.

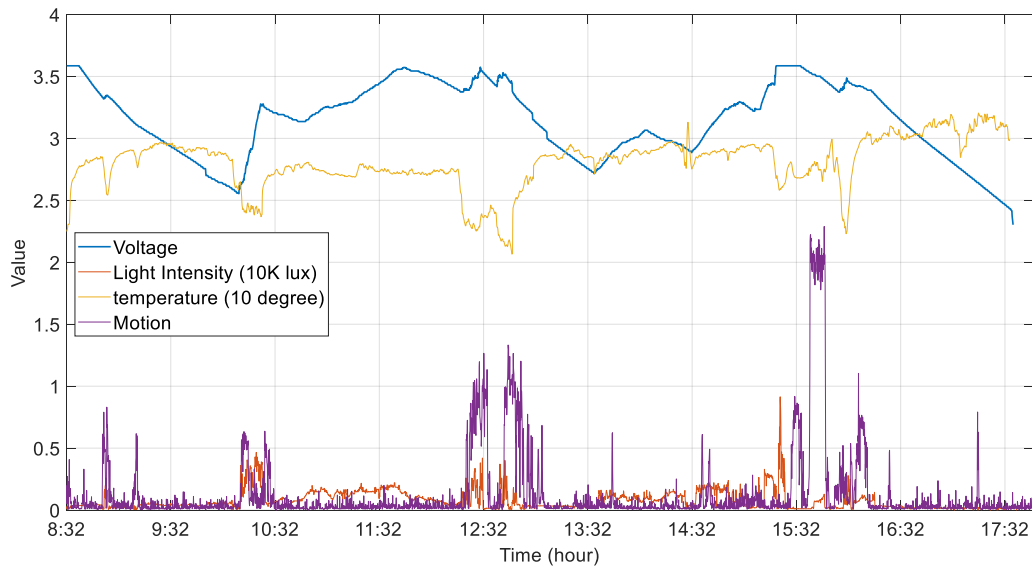


**Figure 7.3 A profile collected on a rainy day.**

### **7.1.2 Profiles in Indoor Environment**

We collected profiles at home as tests of the only indoor environment, also tested the power consumption at different sampling rates. The light intensity is as low as 100 lux in the living room, kitchen, bathroom, .and other rooms, which is usually lower than the office. In addition, the profiles were collected at night, and the light was only from the CFL. In such a dark environment the supercapacitor cannot be charged and kept decreasing until the system is running out of power. Running at other sampling rates were quite similar with longer operation time and thus omitting the plots.

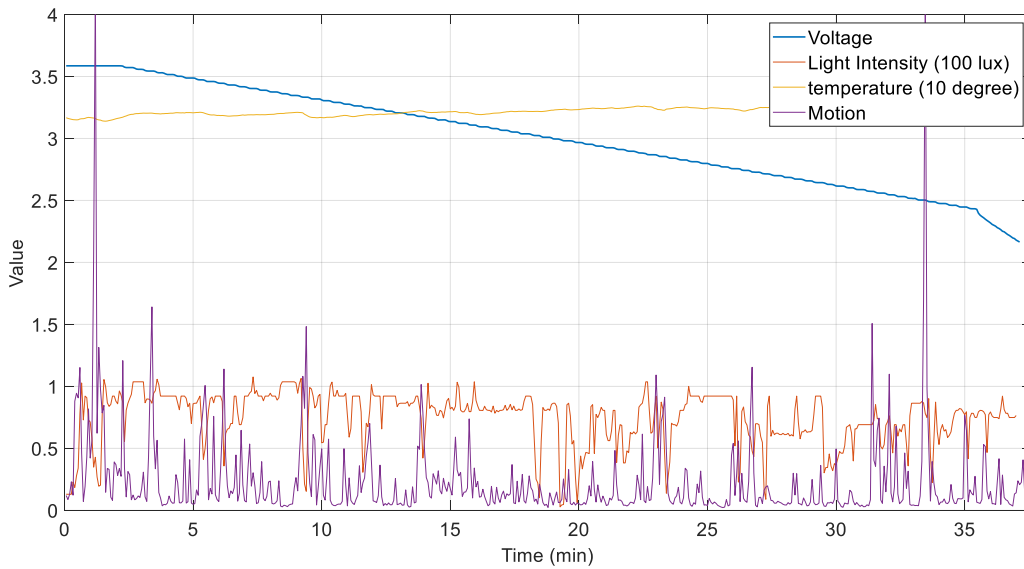


**Figure 7.4 A profile collected at home.**

The voltage versus running time at different sampling frequencies are compared in Figure 7.5.

The voltage on the supercapacitor slowly drops until 2.4V and then suddenly drops to around 2.1V.

This feature is due to the boot converter functions.

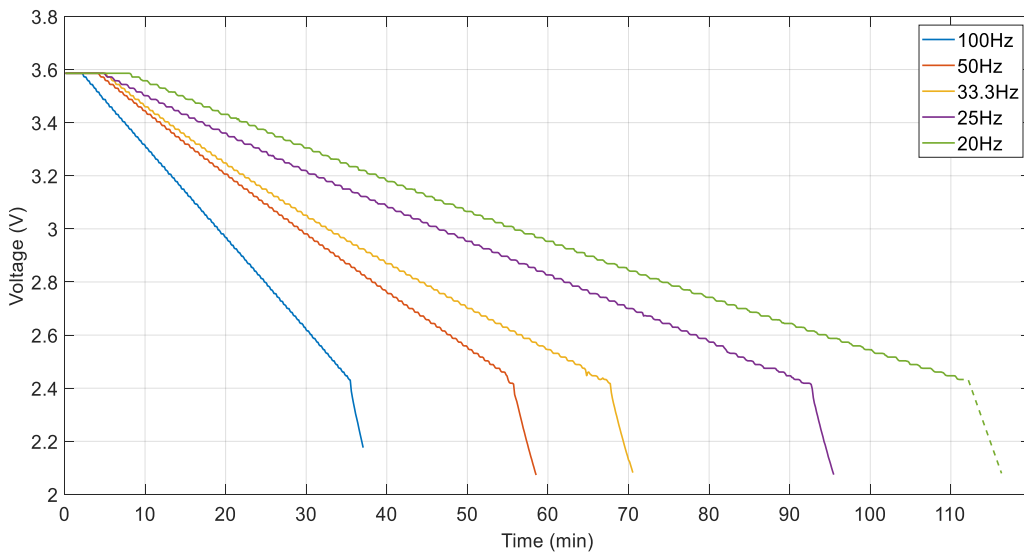


**Figure 7.5 Supercapacitor voltage drop along time at different sampling rates.**

## 7.2 ECG and Motion Details

In addition to the light, temperature, voltage, and Teager, we present the details of the ECG and acceleration collected to prove the function. The in-the-wild ECG monitoring performed well most of the time even during running and exercises.

### 7.2.1 ECG Profile

ECG data of 10 seconds at different sampling frequencies are shown in Figure 7.6. This plot is comparable to Figure 5.12 which shows downsampled versions of ECG signals from the MIT-BIH AF database [97]. Sampling rates below 25Hz lead to the miss of detecting some R peaks as shown in the last two rows.

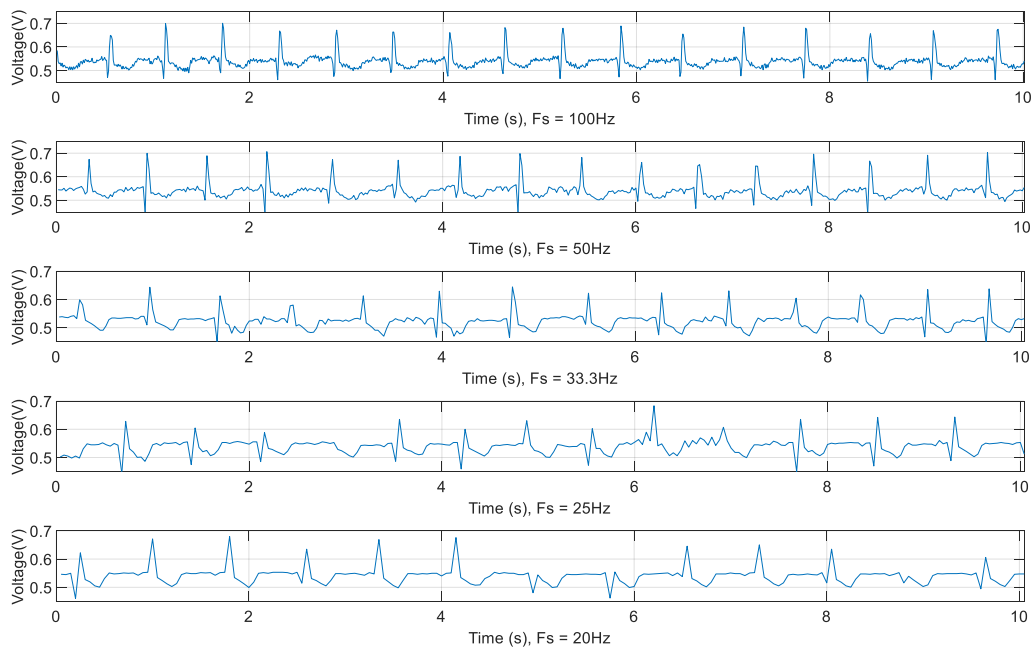


**Figure 7.6 10 seconds ECG signal at different sampling rates.**

The quality of the ECG signal while running is still useful as shown in Figure 7.7. The snippet is from the sunny day profile which collected ECG at 50Hz. During the running, the P-wave and T-wave of the ECG are affected by the running, but the R-peaks are still clear which is frequently

used for health monitoring. For example, the heart rate in beats per minute (BPM) before, during, and after running is displayed in Figure 7.8. The heart rate increased from around 100 to 160 after 2 minutes fast running and kept increasing to 170, then dropped to around 100 again and lowered after rest.

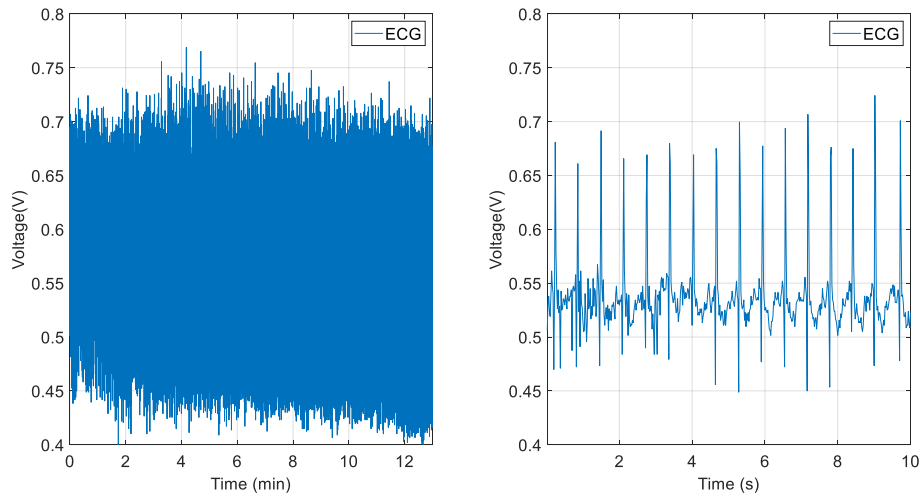


**Figure 7.7 ECG waveform while running.**

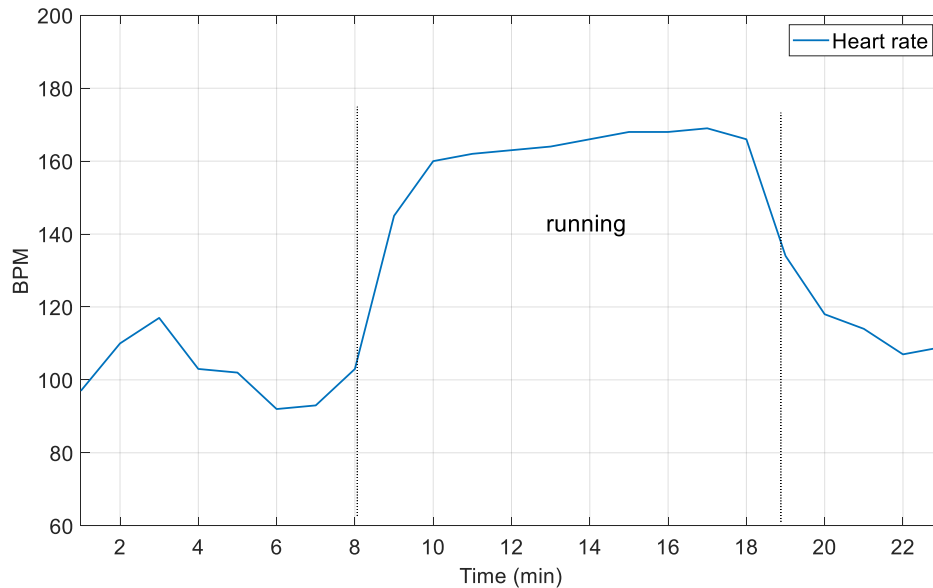


**Figure 7.8 Heat rate (BPM) before, during, and after running calculated from the collected ECG signal.**

## 7.2.2 Motion Profile

The 3-axis acceleration data while running or doing exercise could be employed for motion tracking like step counting, exercise classification. Here we show the acceleration patterns of some activities to demonstrate the potential usage of the SCDPM as a motion tracker, but the specific algorithms are out of the scope of this work. All the profile sessions are from the sunny day profile as shown in Figure 7.1 and were collected at 12.5Hz.

The acceleration pattern while running is shown in Figure 7.9. The left plot shows the overview of a 13-minutes duration, and the right one shows a 10 seconds detail. The acceleration data has significant periodicity, and from the acceleration data, the running pace could be calculated.

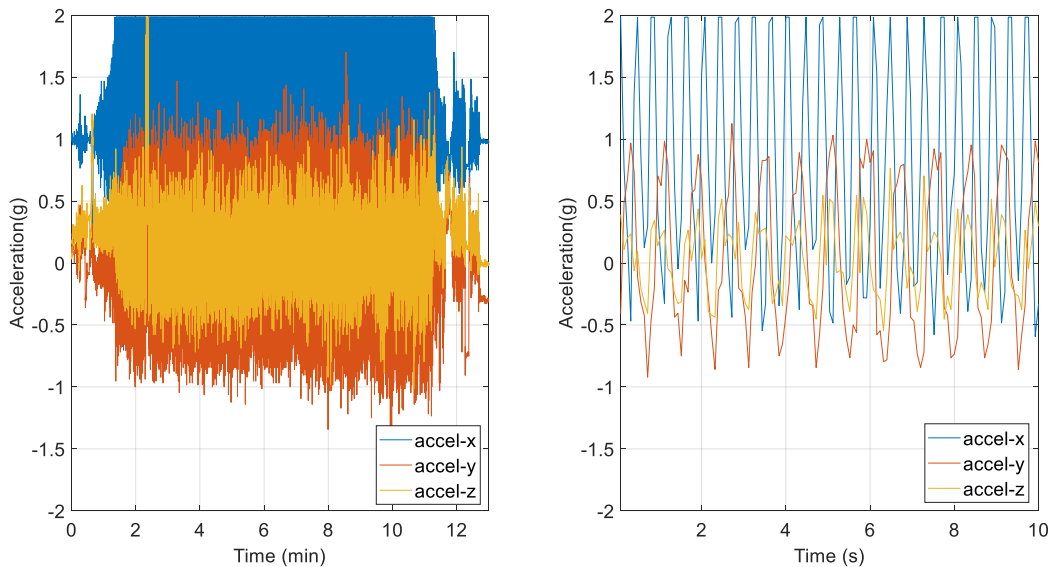


**Figure 7.9 Acceleration during running.**

In addition to the running, doing different exercises has distinct acceleration pattern as well. Here we show two activities including the pulldown and shoulder press. The acceleration during doing pulldown is shown in Figure 7.10, and doing shoulder press is shown in Figure 7.11. The acceleration pattern including the duration, values, shape could be used to classify different activities for monitoring or training.

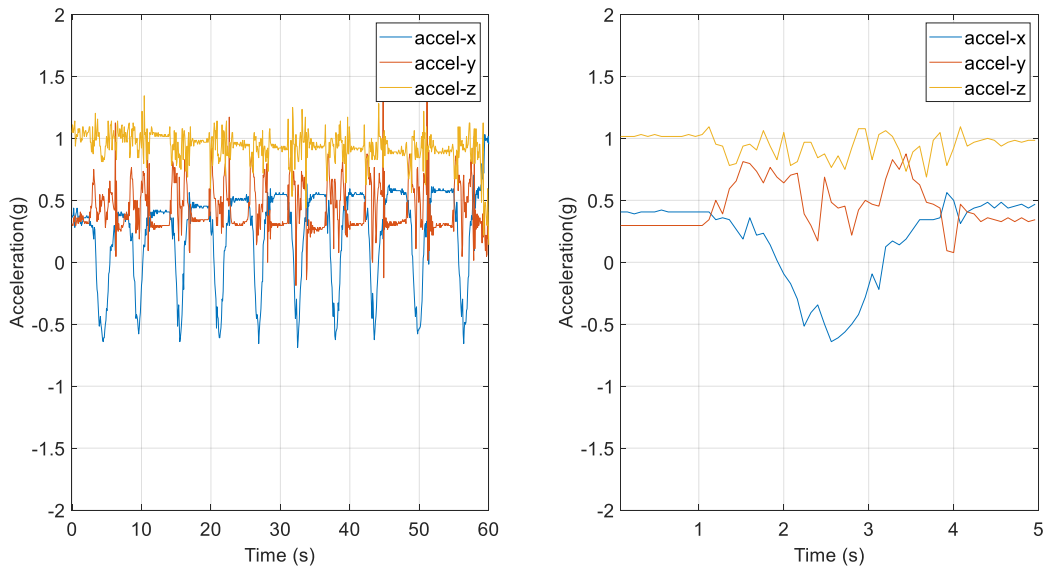


**Figure 7.10 Acceleration during pulldown exercise.**

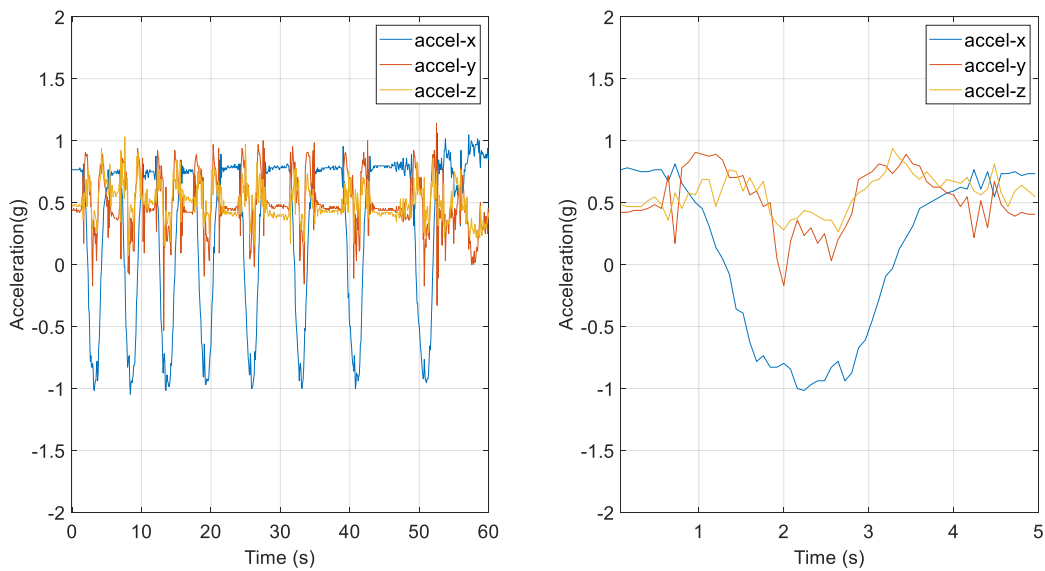


**Figure 7.11 Acceleration during shoulder press exercise.**

### 7.3 Energy Prediction

Unlike EHDC, the SCDPM platform does not have a current monitor, so the harvested power cannot be measured directly, and we assume the solar energy is linearly related to the light intensity as in [64]. The relationship could be calculated with linear regression. As mentioned before, the

TEG power constitutes a very limited amount of the total power, so we only consider the solar energy.

An average profile in the daytime is calculated from the three collected profiles presented before, and we keep it in the model as  $E_i^P$ . Each point represents the average power in a 10 minutes interval. The number of the profiles are quite limited, and it could be improved with more data collection.

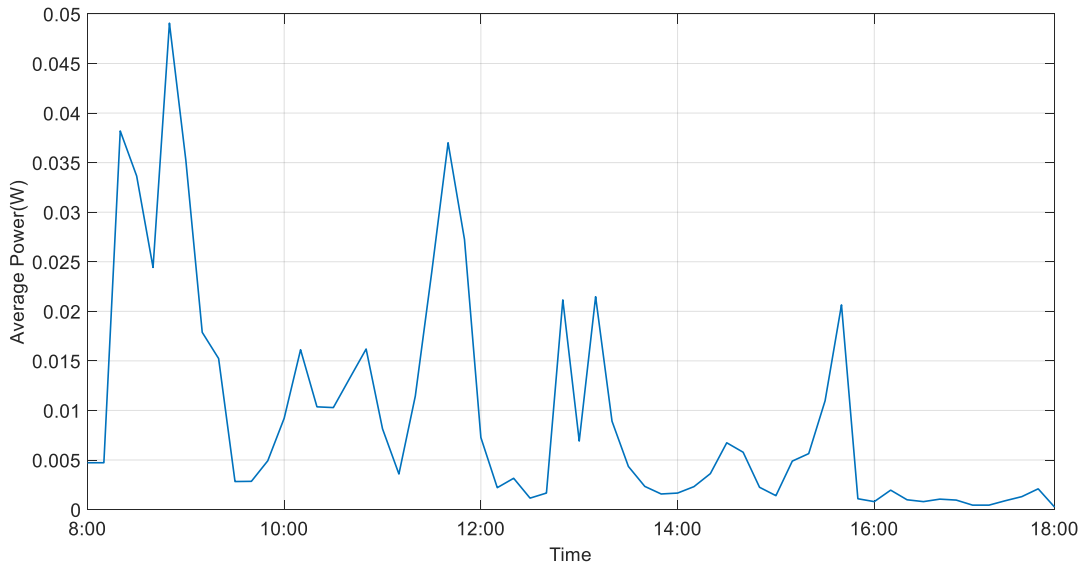


**Figure 7.12 Average power profile in the daytime.**

### 7.3.1 Weather Parameter

Weather parameter regarding the weather icons[113] is discussed. Only the daylight parameters are considered. Theoretically, to acquire the parameters for each weather conditions, long-term experiments are required to record the light intensity data and then make a linear regression for each case. However, this costs much time and are not directly related to the research focus. Therefore, here we calculate the parameters with the data in weather conditions we have, then estimate others. By analyzing the profiles, we use an average of 20K lux as the full light intensity in sunny conditions.

**Table 7.2 Power consumption of each component.**

<b>Weather parameter</b>	<b>Weather Icon (code)</b>
<b>1.0</b>	Sunny(1)
<b>0.95</b>	Mostly Sunny(2)
<b>0.85</b>	Partly Sunny(3), Partly Sunny w/ Showers(14) Partly Sunny w/ T-Storms(17) Partly Sunny w/ Flurries(21)
<b>0.75</b>	Intermittent Clouds(4)
<b>0.60</b>	Hazy Sunshine(5)
<b>0.30</b>	Mostly Cloudy(6) Mostly Cloudy w/ Showers(13) Mostly Cloudy w/ T-Storms(16) Mostly Cloudy w/ Flurries(20) Mostly Cloudy w/ Snow(21)
<b>0.12</b>	Cloudy(7)
<b>0.05</b>	Dreary (Overcast)(8) Fog(11), Rain(18), Flurries(19) , Snow(22)

### **7.3.2 Location Profiles**

The indoor environment is mainly human controlled and thus stable. The four typical locations are summarized in Table 7.3. The measured temperature seems to be affected by the skin since it is attached to the armband, and higher than the actual room temperature. For the office environment, since the seat is by the window, the light intensity is decided by the sun and the orientation of the window. In the early morning, there is a period of time that the solar cells receive direct solar radiation and the light intensity could be at most more than 10 K lux. Since the light is directly from the sun, it is considered as outdoor, and the data is not included in the table. Indirect solar radiation situations are considered as indoor which is about several K lux level but still varies significantly. In the afternoon, the light intensity is reduced to around 800~2000 lux. Except for the “Office”, the light sources of the other three locations are mainly decided by the indoor light and quite stable.

**Table 7.3 Indoor location profiles.**

Location	Light (mean)	Light (std)	Temperature (mean)	Temperature (std)
Home	74.9	8.1	32.2	0.3
Gym	108.9	39.0	28.8	0.85
Office	936.8	323.9	28.3	1.0
Meeting room	342.3	29.1	30.2	0.5

### 7.3.3 Experiment and Results

Here we use a day's profile to present the context-aware prediction. To show the difference between the EWMA based methods as discussed in Section 4.2, we assume there is a calendar and weather information available for the prediction.

The schedule and the weather information of this day are summarized as follows. Here we assume an ideal situation that there is a complete calendar event list from the beginning to the end. However, in the real world there might be only a few calendar events, then the prediction is based more on the history profile.

**Table 7.4 A schedule and weather forecast of a typical day.**

Time	Activity	Location	Weather forecast (icon, Temperature °F)
08:30 ~ 10:30	Work	Office	(1, 68~72)
10:30 ~ 11:30	Meeting	Meeting room	(1, 72~75)
11:30 ~ 11:45	Outdoor for lunch	Outdoor	(1, 75)
11:45 ~ 12:15	Lunch	Home	(1, 75~78)
12:15 ~ 12:30	Return to office	Outdoor	(1, 78)
12:30 ~ 13:30	Work	Office	(1, 78~80)
13:30 ~ 15:00	Meeting	Meeting room	(1, 80~82)
15:00 ~ 16:00	Exercise	Gym	(1, 82)
16:00 ~ 17:00	Office	Office	(1, 83)

In the experiment, we show the context-based medium-term prediction and short-term prediction. At the beginning of a day, the scheduler acquires information including weather and calendar events. Then it makes an initial day-long prediction which is used for the DPM. Since the

light intensity is assumed to be directly related to the solar energy, here we use light intensity prediction to show the results.

The data from the location's profile as shown in previous Table 7.3 is used for prediction as represented by the blue line. A limitation of using calendar events is that the event might not happen or the real time of the event could be different from the calendar. For instance, it was scheduled to be in the gym from 15:00 ~ 16:00, while actually, it happened from 15:10 ~ 15:40. This type of error could be alleviated by the short-term prediction.

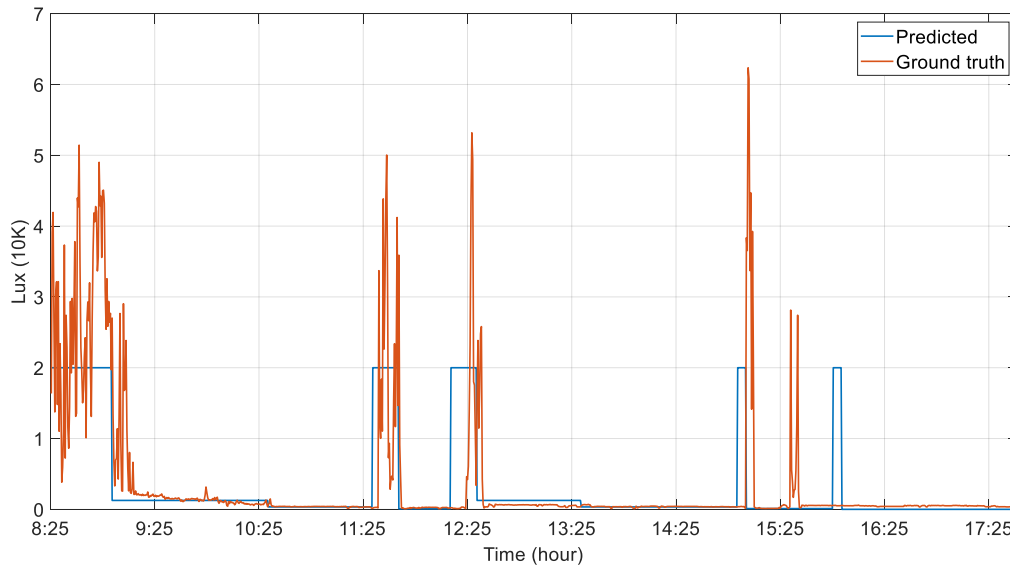


**Figure 7.13 Long-term prediction of light intensity using context information.**

For short-term predictions, we utilize the exponential smoothing method which is one of the most frequently used with high accuracy. The time slot is selected as 30 seconds as mentioned in Chapter 4. The results of the short-term prediction are shown in Figure 7.14. The RMSE of the long-term and short-term prediction is 7.60K and 7.35K, respectively.

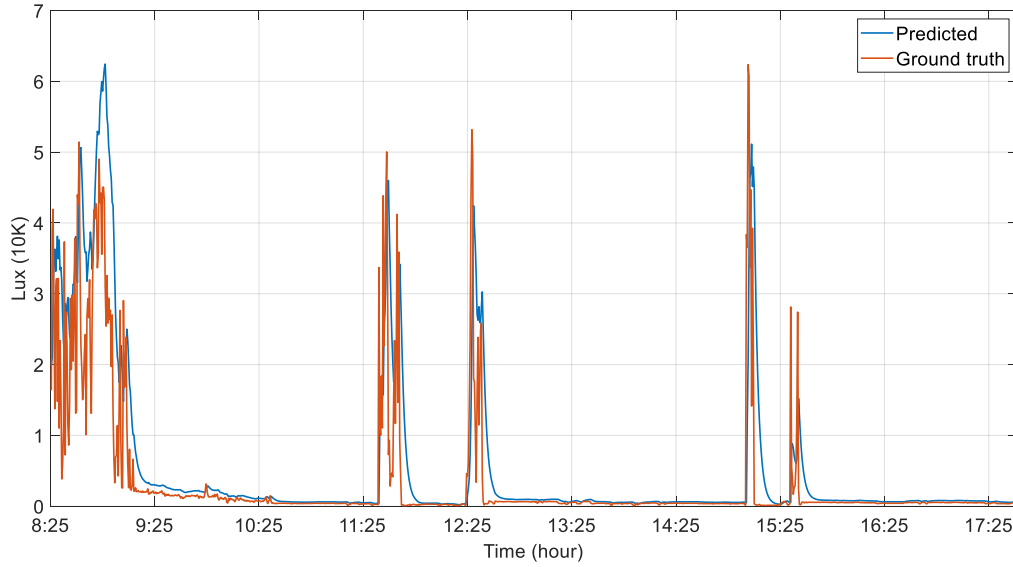


**Figure 7.14 Short-term prediction of light intensity using exponential smoothing.**

## 7.4 Dynamic Power Management on SCDPM

The proposed DPM algorithms are discussed in Section 5. Here we run the algorithms on the collected profiles and test how the power consumption and cost will change. For the cost function, we follow the application-specific equation (5.75) derived in Section 5.6. For the online algorithm, we mainly demonstrate the capability of adaptively changing sampling rates.

In the SCDPM, the operation voltage of the supercapacitor is from 2.15V~3.6V. Thus the equivariant capacity limit of the supercapacitor is

$$C = \frac{1}{2} Cap(V_{Full}^2 - V_{Low}^2) = 4.17J \quad (7.1)$$

### 7.4.1 The Offline Algorithm

The optimal offline solution is discussed first. Here we selected the time slot as 2 minutes. The y-axis is the energy harvested or consumed in the 2 minutes window. We assume the system could be configured to consume any amount of power.

The power consumption of the optimal DPM scheduling is shown by the yellow curve, and the static power consumption that we used for collecting the profile is shown in the orange curve. The optimal solution, if we have a big enough supercapacitor without wasting any energy, is shown by the purple line. The cost of static, dynamic, dynamic without capacity limit is 30.06, 23.82, and 21.30, respectively.

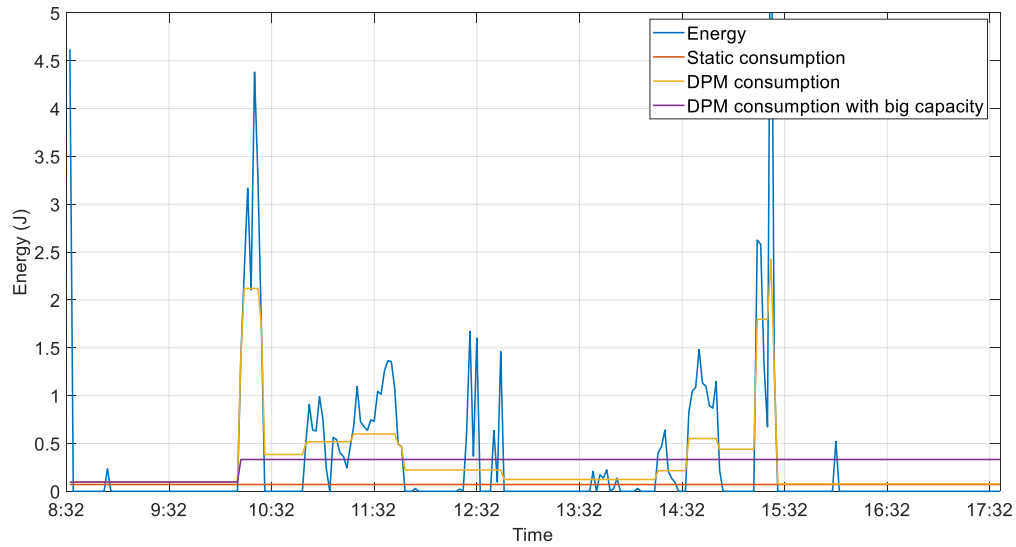


**Figure 7.15 Power management with different policies for the rainy day.**

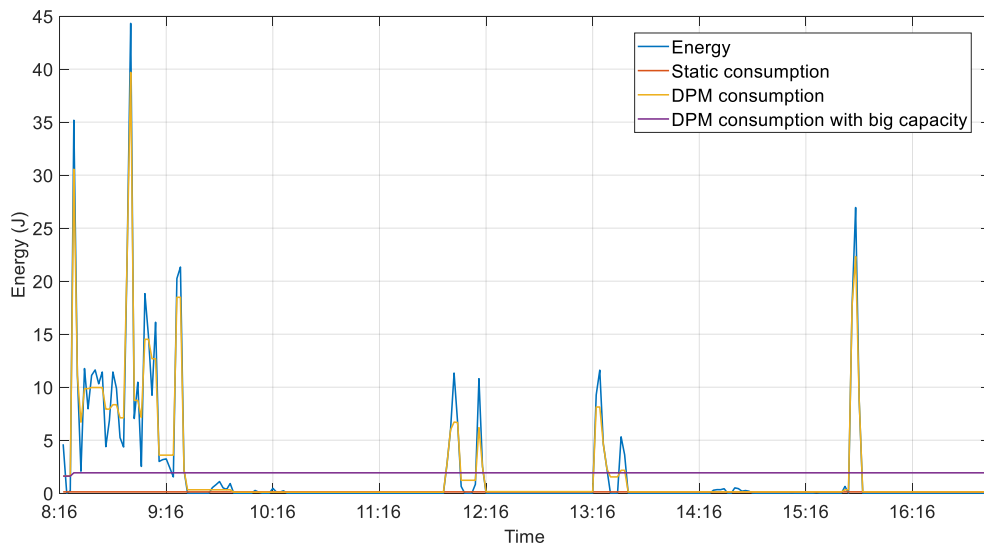


**Figure 7.16 Power management with different policies for the sunny day.**

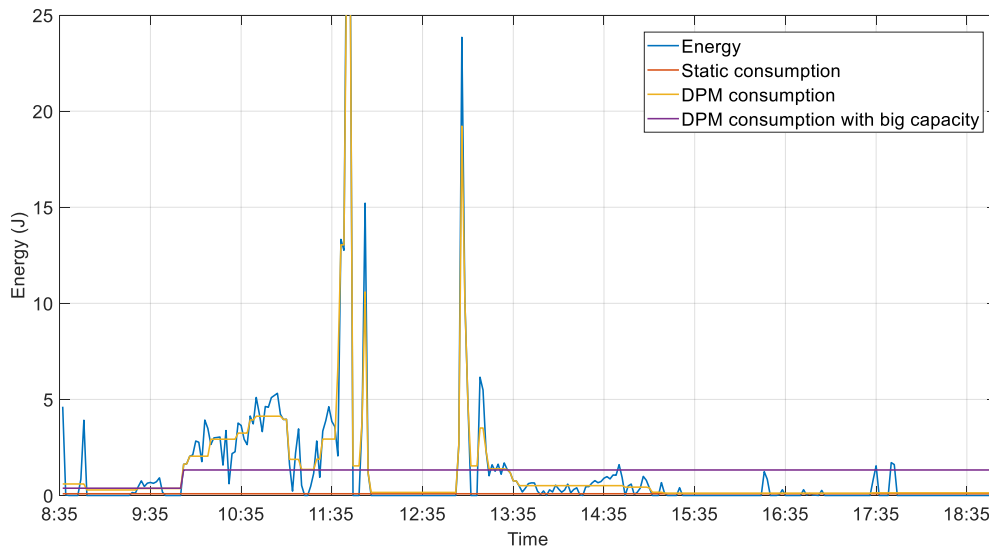


**Figure 7.17 Power management with different policies for the cloudy day.**

Similarly, we plotted the other two profiles and analyzed the DPM performance of them. The results are summarized in Table 7.5. Here we see the demand for high capacity or high power-density supercapacitors. As shown in Section 5, low capacity limits the DPM performance. From the results, based on our current platform supercapacitors with much more capacitance are required to improve the overall power management performance.

**Table 7.5 DPM performance comparison over three profiles.**

Cost	Sunny	Cloudy	Rainy
Static	53.55	40.48	30.06
DPM	45.36	37.69	23.82
DPM without limit	36.29	29.07	21.30
Required capacity(J)	596.62	244.65	23.02

### 7.4.2 The Online Algorithm

The online solution is tested on the profile that mentioned in Section 7.3.3. The SCDPM platform and most of the others cannot have continuous power states, and here we only demonstrate the dynamic adaptive sampling. The scheduler on the phone side could adjust sampling rates in real-time.

The profile and power management results are shown in Figure 7.18. The profile was collected from 8:25 am to 5:39 pm with around 9 hours with dynamic power management. The smartphone is responsible for scheduling the system and sending parameters to the system to adjust the operating parameters. Here we used discrete sampling rates from the list {100Hz, 50Hz, 33.3Hz, 25Hz, 20Hz} to prove that the system could be able to execute dynamic power management according to the predicted energy status.

In the morning the solar energy was sufficient to support the system running at the 100Hz. Between 8:25 am to 9:00 am, there was direct sunlight on the solar cells, as shown by the red curves. Then the light intensity was decreasing to around 1500 lux in the office and around 300 lux in the meeting room. Going home for lunch and returning to the office were the two out periods and the sampling rate was adjusted to 100Hz again. In the afternoon, since there was a long indoor period. The sampling rate was decreased to 25Hz and later to 20Hz. Following are the two short outdoor periods for going to the gym and returning. The system was then running at 33.3Hz till being powered down.

Instead of running at a fixed sampling rate like most of the previous work, adaptively change operating parameters bring a better performance by leveraging the understanding of the energy dynamics.

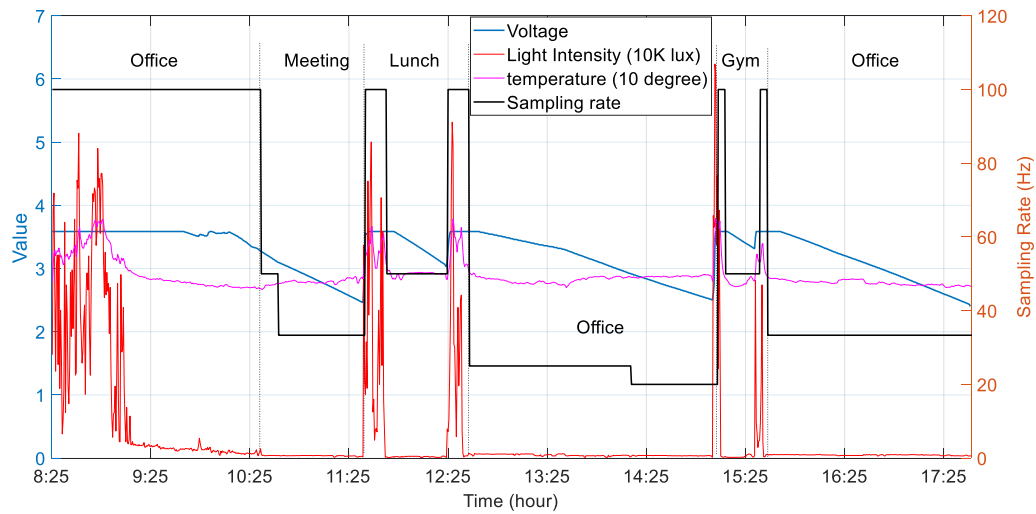


**Figure 7.18 The profile and dynamic power management.**

## 7.5 Summary

In this chapter, we presented experiments and results for the validation of the designed SCDPM platform. The SCDPM was used to collect multiple series of profiles in the real world. The sensor data including ECG, motion, environmental sensors are analyzed and presented. The platform is also utilized to demonstrate the proposed energy prediction and DPM algorithms.

# 8 Closing Remarks

Over the course of this dissertation, we presented energy harvesting profiling and context-aware dynamic power management model to achieve better power management performance of self-powered BSN systems. In addition to the in-lab characterization of energy harvesters, we profiled energy harvesting on the human body in the real world and collected data of environmental factors and human behavior to study the energy harvesting dynamics in depth. The convex optimization model is formalized to solve the fundamental problem of system level power management in energy harvesting systems. The offline solution and online solution with context-based energy harvesting prediction were developed for dynamic power management in real applications to maximize application-specific data quality while preserving continuous self-powered operation.

## 8.1 Contributions and Future Work

The contributions of this dissertation include:

1. Energy profiling for BSN in the real world. The idea of understanding energy harvesting dynamics by profiling it in the real world in addition to the in-lab characterization is innovative at the time of publishing the papers. The Energy Harvesting and Data Collection (EHDC) platform for energy harvesting profiling and modeling was one of the first platforms that implement this idea. The EHDC platform itself could be considered a contribution, as well and the LITE project discussed in Section 3.5 is

actually an example usage of EHDC. The software code for the EHDC is open sourced on [27] for people to use.

2. A context-aware hybrid energy prediction model for both indoor and outdoor environment energy harvesting. This is more like a framework than a model, and we use calendar events and weather forecast as the context information for the prediction. The scope of context and the way to the context information could be extended.
3. A context-aware Dynamic Power Management (DPM) framework for energy harvesting BSNs. A formal model and analysis of the scheduling optimization problem in an energy harvesting system are constructed, and the optimal solution is derived. A case study of AFib detection is intensely studied to prove the validity of the framework.
4. A Self-powered Context-aware DPM (SCDPM) platform for vigilant health monitoring including motion, ECG, and environmental data collection. The SCDPM is an ultralow power platform which performs better than state-of-the-art health monitoring platforms regarding system power consumption and the dynamic power management and adaptive sensing capabilities. The entire system comprises the work of hardware system design, embedded system programming for the sensor node, Android application design on the phone side, and power modeling. The code of the platform is open sourced [28].

Future works required to achieve the perpetual operation of self-powered BSN include:

- Collecting more profiles to improve the accuracy of prediction. The human behavior is complex to model, and the profile-based models could help to understand the behavior and make better predictions. The prediction will be more accurate by exploring more profiles in different conditions.

- A better understanding of the context information. In this work, we use calendar events and weather forecast to help predict energy harvesting. However, the scope of the context and the way to utilize the information is not thoroughly discussed. Future work could extend the idea of context-aware prediction.
- Ultralow power SoC, radio, protocols, sensors, and better energy harvesters. In this work, though the energy is from both solar and thermoelectric, the thermoelectric energy is too small compared to the solar energy. With higher efficiency TEGs, the thermoelectric energy could be complementary to the solar energy and achieve more harvested energy.
- Human behavior related modeling. For instance, extending indoor/outdoor prediction considering human behavior. Explore more context information especially related to the human behavior which could help to improve the energy harvesting prediction.
- More and further case studies in BSN area to explore the relationship between power consumption and application-specific utility. We use the AFib, which is typical heart disease, to demonstrate the application-specific performance could be more helpful. Other medical applications could be studied to extend the scope.
- Improvement of the wearability of the sensing and energy harvesting system which enable the long-term health monitoring in the real world.

## 8.2 Publications

The publications during the Ph.D. study:

**D. Fan**, L. L. Ruiz, and J. Lach, “Application-driven dynamic power management for self-powered vigilant monitoring,” in 2018 IEEE 15th International Conference on Wearable and Implantable Body Sensor Networks (BSN), 2018

L. L. Ruiz, M. Ridder, **D. Fan**, J. Gong, J. Lach, and J. Strohmaier, “SCAVM: A self-powered cardiac and activity vigilant monitoring system,” in 2017 IEEE Biomedical Circuits and Systems Conference (BioCAS), 2017

**D. Fan**, L. Lopez Ruiz, J. Gong, and J. Lach, “EHDC: An Energy Harvesting Modeling and Profiling Platform for Body Sensor Networks,” IEEE J. Biomed. Heal. Informatics, vol. 2194, no. c, 2017.

**D. Fan**, L. L. Ruiz, J. Gong, and J. Lach, “Profiling, modeling, and predicting energy harvesting for self-powered body sensor platforms,” in 2016 IEEE 13th International Conference on Wearable and Implantable Body Sensor Networks (BSN), 2016

**D. Fan**, J. Gong, B. Ghaemmaghami, A. Zhang, J. Lach, and D. B. Peden, “Characterizing and Calibrating Low-Cost Wearable Ozone Sensors in Dynamic Environments,” in 2017 IEEE/ACM International Conference on Connected Health: Applications, Systems and Engineering Technologies (CHASE), 2017

**D. Fan**, J. Gong, and J. Lach, “Eating gestures detection by tracking finger motion,” in 2016 IEEE Wireless Health (WH), 2016

J. Gong, K. M. Rose, I. A. Emi, J. P. Specht, Enamul Hoque, **D. Fan**, S. R. Dandu, R. F. Dickerson, Y. Perkhounkova, J. Lach, J. A. Stankovic “Home Wireless Sensing System for Monitoring Nighttime Agitation and Incontinence in Patients with Alzheimer’s Disease,” in 2015 IEEE Wireless Health (WH), 2015

# Appendix A. Other Completed Research Projects

In addition to the work that directly related to the dissertation, there are other works in the BSN area that I accomplished during the Ph.D. research.

## A.1 Data Aggregator Design for Custom Ultra-Low Power Radio

Wireless communication consumes a significant portion of the power profile. Therefore custom protocols are utilized to achieve better power performance in some specific applications. Ultra-Wide Band (UWB) radio[50] could be used in short range, and it consumes much less power than other radio like Bluetooth or Bluetooth Low Energy (BLE). In the project, a 4.18uW UWB transmitter [30] is used for communication from a self-powered sensor node to a data aggregator. Unlike using Bluetooth protocol which end devices could directly communicate with the sensor nodes, a data aggregator is required to process the custom UWB signal and then transfer to an end device like a phone. The data aggregator is also responsible for data processing, data visualization, and cloud computing interface.

In this collaborative project, firstly, I co-designed the custom data aggregator integrating an IOIO board, an FPGA board, and a radio board, and validated the functionality. Second, I designed and implemented Java and Android application for data communication, visualization, and cloud

computing interface. Third, I designed a repetition code with context information to reduce communication errors.

## **A.2 Wearable Ozone Sensors Calibration in Dynamic Environments**

Air quality has been investigated in recent years due to its high relevance to public health. To assist persons with asthma, wearable devices that enable alerts of potential asthma attacks caused by high ozone concentration exposure could become a life-saving technology. We have developed hardware sensing platforms with low-cost ozone sensors, calibrated sensors in an ozone chamber in NCU and proposed algorithms to calibrate ozone sensors regarding dynamic environmental context, especially temperature and relative humidity (RH). The algorithms integrated characteristics of the ozone sensors under influences of RH and temperature and optimized the trade-off between calibration complexity and quality of the measurement.

In this collaborative project, I designed the first version sensor daughter board working with a Shimmer 2 node, calibrated ozone sensors in the ozone chamber several times, and proposed the algorithms. The work is published in CHASE 2017 [114].

## **A.3 Eating Gestures Detection by Tracking Finger Motion**

Individuals' eating habits are growing to be a major concern of healthcare researchers since unhealthy eating habits such as irregular eating schedule, speed eating, are related to various diseases such as obesity, diabetes, and cardiovascular diseases. Monitoring people's eating behavior provides opportunities to give feedback and suggestions towards healthy eating habits. The motivation of this project is to explore the potential of detecting eating gestures by tracking finger motion. Seven state-of-the-art learning methods are tested to make binary (eating/non-eating) or multiclass (seven classes) classification. Accelerometer and gyroscope datasets are tested separately and compared. The results show that for finger motion data, K-Nearest Neighbor (KNN)

performs best in binary classification, which performs better than on wrist motion dataset. The results indicate that finger motion is a useful indicator for classifying eating and non-eating behaviors. The work has been published in [115].

#### **A.4 Nighttime Agitation and Incontinence Monitoring**

Patients with Alzheimer's Disease frequently experience urinary incontinence, disturbed sleep, and nighttime agitation. Although anecdotal evidence shows that there is a relationship between these three phenomena, there is a lack of systematic evidence. In this project, we explored the relationships among the times of occurrence of nighttime agitation, sleep quality, and urinary incontinence by using innovative and non-invasive sensing technology.

In this collaborated project, I deployed hardware platforms in three patients' homes, processed sensor data and proposed algorithms for agitation detection and correlation inference. The work has been published [6].

# Bibliography

- [1] B. H. Calhoun *et al.*, “Body sensor networks: A holistic approach from silicon to users,” *Proc. IEEE*, vol. 100, no. 1, pp. 91–106, 2012.
- [2] C. Poon, B. Lo, M. Yuce, A. Alomainy, and Y. Hao, “Body Sensor Networks: In the Era of Big Data and Beyond,” *IEEE Rev. Biomed. Eng.*, vol. 3333, no. 1, pp. 1–1, 2015.
- [3] S. C. Mukhopadhyay, “Wearable Sensors for Human Activity Monitoring: A Review,” *IEEE Sens. J.*, vol. 15, no. 3, pp. 1321–1330, 2015.
- [4] M. A. Hanson *et al.*, “Body Area Sensor Networks: Challenges and Opportunities,” *Computer (Long. Beach. Calif.)*, vol. 42, no. 1, pp. 58–65, 2009.
- [5] L. Song, Y. Wang, J. J. Yang, and J. Li, “Health sensing by wearable sensors and mobile phones: A survey,” *2014 IEEE 16th Int. Conf. e-Health Networking, Appl. Serv. Heal. 2014*, pp. 453–459, 2015.
- [6] J. Gong *et al.*, “Home Wireless Sensing System for Monitoring Nighttime Agitation and Incontinence in Patients with Alzheimer ’ s Disease,” *Wirel. Heal. Conf.*, 2015.
- [7] T. Falck, J. Espina, J. P. Ebert, and D. Dietterle, “BASUMA - The sixth sense for chronically III patients,” *Proc. - BSN 2006 Int. Work. Wearable Implant. Body Sens. Networks*, vol. 2006, pp. 57–60, 2006.
- [8] D. Popescu and G. Stamatescu, “Cell - based Sensor Network for Complex Monitoring at Home of Patients with Chronic D iseases,” pp. 1–6, 2013.
- [9] J. Dieffenderfer *et al.*, “Low Power Wearable Systems for Continuous Monitoring of Environment and Health for Chronic Respiratory Disease,” *IEEE J. Biomed. Heal. Informatics*, vol. 20, no. 5, pp. 1–1, 2016.
- [10] M. G??rs, M. Albert, K. Schwedhelm, C. Herrmann, and K. Schilling, “Design of an Advanced Telemedicine System for Remote Supervision,” *IEEE Syst. J.*, vol. 10, no. 3, pp. 1089–1097, 2016.
- [11] A. Q. Javaid, N. F. Fesmire, M. A. Weitnauer, and O. T. Inan, “Towards robust estimation of systolic time intervals using head-to-foot and dorso-ventral components of sternal acceleration signals,” *2015 IEEE 12th Int. Conf. Wearable Implant. Body Sens. Networks, BSN 2015*, 2015.
- [12] A. Kansal, J. Hsu, S. Zahedi, and M. B. Srivastava, “Power management in energy

- harvesting sensor networks,” *ACM Trans. Embed. Comput. Syst.*, vol. 6, no. 4, p. 32–es, 2007.
- [13] J. Lu, S. Liu, Q. Wu, and Q. Qiu, “Accurate modeling and prediction of energy availability in energy harvesting real-time embedded systems,” *Green Comput. Conf. 2010 Int.*, 2010.
- [14] W. K. G. Seah, Z. A. Eu, and H.-P. Tan, “Wireless sensor networks powered by ambient energy harvesting (WSN-HEAP) - Survey and challenges,” in *2009 1st International Conference on Wireless Communication, Vehicular Technology, Information Theory and Aerospace & Electronic Systems Technology*, 2009, pp. 1–5.
- [15] P. Lee, Z. A. Eu, M. Han, and H.-P. Tan, “Empirical modeling of a solar-powered energy harvesting wireless sensor node for time-slotted operation,” *2011 IEEE Wirel. Commun. Netw. Conf.*, pp. 179–184, 2011.
- [16] M. Hassan and A. Bermak, “Solar harvested energy prediction algorithm for wireless sensors,” *Proc. 4th Asia Symp. Qual. Electron. Des. ASQED 2012*, pp. 178–181, 2012.
- [17] C. Petrioli and D. Spenza, “Pro-Energy: a novel energy prediction model for solar and wind energy harvesting Wireless Sensor Networks,” pp. 75–83, 2012.
- [18] Y. K. Tan and S. K. Panda, “Energy Harvesting from Hybrid Indoor Ambient Light and Thermal Energy Sources for Enhanced Performance of Wireless Sensor Nodes,” *Ind. Electron. IEEE Trans.*, vol. 58, no. 9, pp. 4424–4435, 2011.
- [19] C. Alippi and C. Galperti, “An Adaptive System for Optimal Solar Energy Harvesting in Wireless Sensor Network Nodes,” *IEEE Trans. Circuits Syst. I Regul. Pap.*, vol. 55, no. 6, pp. 1742–1750, 2008.
- [20] A. Chirap, V. Popa, E. Coca, and D. A. Potorac, “A study on light energy harvesting from indoor environment The autonomous sensor nodes,” pp. 127–131, 2014.
- [21] A. S. Teran *et al.*, “AlGaAs Photovoltaics for Indoor Energy Harvesting in mm-Scale Wireless Sensor Nodes,” vol. 62, no. 7, pp. 2170–2175, 2015.
- [22] S. Bader and B. Oelmann, “Enabling battery-less wireless sensor operation using solar energy harvesting at locations with limited solar radiation,” *Proc. - 4th Int. Conf. Sens. Technol. Appl. SENSORCOMM 2010*, pp. 602–608, 2010.
- [23] V. Raghunathan, A. Kansal, J. Hsu, J. Friedman, and M. Srivastava, “Design considerations for solar energy harvesting wireless embedded systems,” *IPSN 2005. Fourth Int. Symp. Inf. Process. Sens. Networks, 2005.*, pp. 457–462, 2005.
- [24] K. Kadirvel *et al.*, “A 330nA energy-harvesting charger with battery management for solar and thermoelectric energy harvesting,” *Dig. Tech. Pap. - IEEE Int. Solid-State Circuits Conf.*, vol. 55, pp. 106–107, 2012.
- [25] L. Wang *et al.*, “AdaptSens: An adaptive data collection and storage service for solar-

- powered sensor networks,” *Proc. - Real-Time Syst. Symp.*, pp. 303–312, 2009.
- [26] J. Kim and C. Kim, “A regulated charge pump with low-power integrated optimum power point tracking algorithm for indoor solar energy harvesting,” *Proc. Asia South Pacific Des. Autom. Conf. ASP-DAC*, vol. 58, no. 12, pp. 107–108, 2013.
- [27] Dawei Fan, “EHDC code.” [Online]. Available: <https://github.com/fandw06/Energy-harvesting-and-data-collection-platform>. [Accessed: 10-Jul-2018].
- [28] Dawei Fan, “SCDPM code.” [Online]. Available: <https://github.com/fandw06/scdpm-cpp>. [Accessed: 10-Jul-2018].
- [29] Y. Zhang *et al.*, “A batteryless 19  $\mu$ W MICS/ISM-band energy harvesting body sensor node SoC for ExG applications,” *IEEE J. Solid-State Circuits*, vol. 48, no. 1, pp. 199–213, 2013.
- [30] A. Roy *et al.*, “A 6.45 Self-Powered SoC With Integrated Energy-Harvesting Power Management and ULP Asymmetric Radios for Portable Biomedical Systems,” *IEEE Trans. Biomed. Circuits Syst.*, vol. 9, no. 6, pp. 862–874, 2015.
- [31] A. Rahman *et al.*, “Reliability studies of a 22nm SoC platform technology featuring 3-D tri-gate, optimized for ultra low power, high performance and high density application,” *IEEE Int. Reliab. Phys. Symp. Proc.*, pp. 1–6, 2013.
- [32] R. Braojos *et al.*, “Nano-engineered Architectures for Ultra-low Power Wireless Body Sensor Nodes,” *Proc. Elev. IEEE/ACM/IFIP Int. Conf. Hardware/Software Codesign Syst. Synth.*, p. 23:1--23:10, 2016.
- [33] Y. Lu and T. J. Kazmierski, “An Ultra-Low-Power Variable-Accuracy Bit-serial FFT Butterfly Processing Element for IoT Sensors,” 2016.
- [34] R. W. T. Ng, A. Laurent, and S. B. Chiang, “Ultra low power SOC for portable health monitoring platforms,” *2011 Int. Symp. Integr. Circuits, ISIC 2011*, pp. 293–296, 2011.
- [35] K. Chikkadi, M. Muoth, C. Roman, M. Haluska, and C. Hierold, “Advances in NO<sub>2</sub> sensing with individual single-walled carbon nanotube transistors,” *Beilstein J. Nanotechnol.*, vol. 5, no. 2, pp. 2179–2191, 2014.
- [36] A. Yelkenci, O. Z. Batur, and B. Sarioglu, “Ultra Low Power All-Digital CMOS Sensor Read Out Circuit for Optically Powered Biomedical Systems,” pp. 1766–1770, 2016.
- [37] W. Zeng, A. Arora, and K. Srinivasan, “Low power counting via collaborative wireless communications,” *Proc. 12th Int. Conf. Inf. Process. Sens. networks - IPSN '13*, p. 43, 2013.
- [38] K. Lendvai, A. Milankovich, S. Imre, and S. Szabo, “Optimized Packet Size for Energy Efficient Delay- Tolerant Sensor Networks with FEC ,” *12th Int. Conf. Telecommun. (CONTEL '13)*, pp. 87–93, 2013.
- [39] A. N. Abdulfattah, C. C. Tsimenidis, and A. Yakovlev, “Subthreshold-based m -sequence

- code generator for ultra low-power body sensor nodes,” pp. 189–195, 2016.
- [40] M. H. D. Z. Mahfouz, A. Meijerink, and M. J. Bentum, “Optimum Design Parameters for Ultra-Low-Power RF Transceivers in Wireless Sensor Networks,” 2016.
- [41] A. C. W. Wong *et al.*, “A 1 V wireless transceiver for an ultra-low-power SoC for biotelemetry applications,” *IEEE J. Solid-State Circuits*, vol. 43, no. 7, pp. 1511–1521, 2008.
- [42] C. Bernier *et al.*, “An ultra low power SoC for 2.4GHz IEEE802.15.4 wireless communications,” *ESSCIRC 2008 - Proc. 34th Eur. Solid-State Circuits Conf.*, pp. 426–429, 2008.
- [43] D. L. L. Donoho, “Compressed sensing,” *IEEE Trans. Inf. Theory*, vol. 52, no. 4, pp. 1289–1306, 2006.
- [44] D. Craven, B. McGinley, L. Kilmartin, M. Glavin, and E. Jones, “Compressed Sensing for Bioelectric Signals: A Review.,” *IEEE J. Biomed. Heal. Informatics*, vol. 2194, no. c, pp. 529–540, 2014.
- [45] L. Xu, X. Hao, N. D. Lane, X. Liu, and T. Moscibroda, “Cost-Aware Compressive Sensing for Networked Sensing Systems,” pp. 130–141.
- [46] J. L-, “Development and Prospect of Compressive Sensing,” no. 7, 2011.
- [47] H. Mamaghanian, S. Member, N. Khaled, D. Atienza, P. Vandergheynst, and S. Member, “Compressed Sensing for Real-Time Energy-Aware ECG Compression on Wireless Body Sensor Nodes,” *IEEE Trans. Biomed. Eng.*, vol. 58, no. 9, pp. 1–10, 2011.
- [48] B. A. Miller, “Bluetooth Technology,” *Handbook of Computer Networks*, 2011. [Online]. Available: <https://www.bluetooth.com/>.
- [49] “zigbee alliance.” [Online]. Available: <http://www.zigbee.org/>.
- [50] F. Sabath, E. L. Mokole, and S.-P. E. (11th : 2012 : T. Conference on Ultra-Wideband, *Ultra-wideband short-pulse electromagnetics 10* . .
- [51] V. Leonov, T. Torfs, P. Fiorini, and C. Van Hoof, “Thermoelectric converters of human warmth for self-powered wireless sensor nodes,” *IEEE Sens. J.*, vol. 7, no. 5, pp. 650–656, 2007.
- [52] D. Fan, L. Lopez Ruiz, J. Gong, and J. Lach, “EHDC: An Energy Harvesting Modeling and Profiling Platform for Body Sensor Networks,” *IEEE J. Biomed. Heal. Informatics*, vol. 2194, no. c, 2017.
- [53] H. Bishop, P. Wang, D. Fan, J. Lach, and B. Calhoun, “Lighting IoT Test Environment (LITE) Platform: Evaluating Light-Powered, Energy Harvesting Embedded Systems,” in *2018 IEEE Global IoT Summit’18*, 2018.

- [54] C. Viehweger, M. Baldauf, T. Keutel, and O. Kanoun, “Energy profile analysis by simulation for the design of energy harvesting systems,” in *International Multi-Conference on Systems, Signals & Devices*, 2012, pp. 1–3.
- [55] V. Leonov, “Thermoelectric Energy Harvesting of Human Body Heat for Wearable Sensors,” *IEEE Sens. J.*, vol. 13, no. 6, pp. 2284–2291, Jun. 2013.
- [56] J. F. Kaiser, “Some useful properties of Teager’s energy operators,” in *IEEE International Conference on Acoustics Speech and Signal Processing*, 1993, pp. 149–152 vol.3.
- [57] IXYS, “IXOLAR High Efficiency SolarMD.” [Online]. Available: [http://ixapps.ixys.com/datasheet/slmd121h041\\_nov16.pdf](http://ixapps.ixys.com/datasheet/slmd121h041_nov16.pdf). [Accessed: 01-Jul-2018].
- [58] A. Kansal, J. Hsu, S. Zahedi, and M. B. Srivastava, “Power management in energy harvesting sensor networks,” *ACM Trans. Embed. Comput. Syst.*, vol. 6, no. 4, p. 32–es, Sep. 2007.
- [59] D. Fan, L. L. Ruiz, J. Gong, and J. Lach, “Profiling, modeling, and predicting energy harvesting for self-powered body sensor platforms,” in *2016 IEEE 13th International Conference on Wearable and Implantable Body Sensor Networks (BSN)*, 2016, pp. 402–407.
- [60] P. J. Brockwell and R. A. Davis, *Introduction to time series and forecasting*. .
- [61] Z. Jiang, X. Jin, and Y. Zhang, “A Weather-Condition Prediction Algorithm for Solar-Powered Wireless Sensor Nodes,” in *2010 International Conference on Computational Intelligence and Software Engineering*, 2010, pp. 1–4.
- [62] J. R. Piorno, C. Bergonzini, D. Atienza, and T. S. Rosing, “Prediction and management in energy harvested wireless sensor nodes,” *Proc. 2009 1st Int. Conf. Wirel. Commun. Veh. Technol. Inf. Theory Aerosp. Electron. Syst. Technol. Wirel. VITAE 2009*, pp. 6–10, 2009.
- [63] D. R. Cox, “Prediction by Exponentially Weighted Moving Averages and Related Methods,” *Journal of the Royal Statistical Society. Series B (Methodological)*, vol. 23. WileyRoyal Statistical Society, pp. 414–422, 1961.
- [64] N. Sharma, J. Gummeson, D. Irwin, and P. Shenoy, “Cloudy Computing: Leveraging Weather Forecasts in Energy Harvesting Sensor Systems,” in *2010 7th Annual IEEE Communications Society Conference on Sensor, Mesh and Ad Hoc Communications and Networks (SECON)*, 2010, pp. 1–9.
- [65] L. Benini, A. Bogliolo, and G. De Micheli, “A Survey of Design Techniques for System-Level Dynamic Power Management,” *IEEE Trans. VLSI Syst.*, vol. 8, no. 3, pp. 299–316, 2000.
- [66] C. Isci, G. Contreras, and M. Martonosi, “Live, runtime phase monitoring and prediction on real systems with application to dynamic power management,” *Proc. Annu. Int. Symp. Microarchitecture, MICRO*, pp. 359–370, 2006.

- [67] E. Y. Chung, L. Benini, A. Bogliolo, and G. De Micheli, “Dynamic power management for nonstationary service requests,” *Des. Autom. Test Eur. Most Influ. Pap. 10 Years Date*, vol. 51, no. 11, pp. 195–206, 2008.
- [68] R. J. Minerick, V. W. Freeh, and P. M. Kogge, “Dynamic Power Management using Feedback \*,” *Power*.
- [69] L. B. and G. D. M. E.-Y. Chung, “Dynamic power management using adaptive learning tree,” *ICCAD '99 Proc. 1999 IEEE/ACM Int. Conf. Comput. Des.*, pp. 274–279, 1999.
- [70] Q. Qiu, Q. Wu, and M. Pedram, “Dynamic power management of complex systems using generalized stochastic Petri nets,” *Proc. 37th Conf. Des. Autom. - DAC'00*, pp. 352–356, 2000.
- [71] G. Dhiman and T. S. Rosing, “Dynamic power management using machine learning,” *Proc. 2006 IEEE/ACM Int. Conf. Comput. Des. - ICCAD '06*, p. 747, 2006.
- [72] S. Irani, S. Shukla, and R. Gupta, “Online strategies for dynamic power management in systems with multiple power-saving states,” *ACM Trans. Embed. Comput. Syst.*, vol. 2, no. 3, pp. 325–346, 2003.
- [73] L. Benini, A. Bogliolo, A. Paleologo, and G. De Micheli, “Policy optimization for dynamic power management,” *IEEE Trans. Comput. Des. Integr. Circuits Syst.*, vol. 18, no. 6, pp. 813–833, 1999.
- [74] L. Benini, G. Castelli, A. Macii, and R. Scarsi, “Battery-driven dynamic power management,” *IEEE Des. Test Comput.*, vol. 18, no. 2, pp. 53–60, 2001.
- [75] T. Simunic, L. Benini, P. Glynn, and G. De Michelli, “Dynamic power management for portable systems,” *MobiCo*, pp. 11–19, 2000.
- [76] M. Pedram, “Power Optimization and Management in Embedded Systems 1,” *Proc. 2001 Asia South Pacific Des. ...*, pp. 239–244, 2001.
- [77] Z. Ren, B. H. Krogh, and R. Marculescu, “Hierarchical adaptive dynamic power management,” *IEEE Trans. Comput.*, vol. 54, no. 4, pp. 409–420, 2005.
- [78] H. Okamura, S. Miyata, and T. Dohi, “A Markov Decision Process Approach to Dynamic Power Management in a Cluster System,” *IEEE Access*, vol. 3, pp. 3039–3047, 2015.
- [79] Y. Shao, C. Li, W. Dong, and Y. Liu, “Energy-Aware Dynamic Resource Allocation on Hadoop YARN Cluster,” in *2016 IEEE 18th International Conference on High Performance Computing and Communications; IEEE 14th International Conference on Smart City; IEEE 2nd International Conference on Data Science and Systems (HPCC/SmartCity/DSS)*, 2016, pp. 364–371.
- [80] Q. Wu *et al.*, “Dynamo: Facebook’s Data Center-Wide Power Management System,” in *2016 ACM/IEEE 43rd Annual International Symposium on Computer Architecture (ISCA)*,

2016, pp. 469–480.

- [81] S. J. Moura, H. K. Fathy, D. S. Callaway, and J. L. Stein, “A Stochastic Optimal Control Approach for Power Management in Plug-In Hybrid Electric Vehicles,” *IEEE Trans. Control Syst. Technol.*, vol. 19, no. 3, pp. 545–555, 2011.
- [82] W. Dargie, “Dynamic power management in wireless sensor networks: State-of-the-art,” *IEEE Sens. J.*, vol. 12, no. 5, pp. 1518–1528, 2012.
- [83] A. Sinha and A. Chandrakasan, “Dynamic power management in wireless sensor networks,” *IEEE Des. Test Comput.*, vol. 18, no. 2, pp. 62–74, 2001.
- [84] V. Raghunathan, C. Schurgers, S. P. S. Park, and M. B. Srivastava, “Energy-aware wireless microsensor networks,” *IEEE Signal Process. Mag.*, vol. 19, no. 2, pp. 40–50, 2002.
- [85] B. Srbinovski, M. Magno, B. O’Flynn, V. Pakrashi, and E. Popovici, “Energy aware adaptive sampling algorithm for energy harvesting wireless sensor networks,” *2015 IEEE Sensors Appl. Symp.*, no. 12, pp. 1–6, 2015.
- [86] D. Fan, L. L. Ruiz, and J. Lach, “Application-driven dynamic power management for self-powered vigilant monitoring,” in *2018 IEEE 15th International Conference on Wearable and Implantable Body Sensor Networks (BSN)*, 2018, pp. 210–213.
- [87] S. P. Boyd and L. Vandenberghe, *Convex optimization*. Cambridge University Press, 2004.
- [88] P. A. Wolf, R. D. Abbott, and W. B. Kannel, “Atrial Fibrillation as an Independent Risk Factor for Stroke: The Framingham Study.”
- [89] N. Larburu, T. Lopetegi, and I. Romero, “Comparative Study of Algorithms for Atrial Fibrillation Detection Body Area Networks , IMEC , Eindhoven , the Netherlands,” pp. 265–268, 2011.
- [90] B. Logan and J. Healey, “Robust Detection of Atrial Fibrillation for a Long Term Telemonitoring System,” pp. 619–622, 2005.
- [91] J. Lian, L. Wang, and D. Muessig, “A Simple Method to Detect Atrial Fibrillation Using RR Intervals,” *AJC*, vol. 107, no. 10, pp. 1494–1497, 2011.
- [92] K. Tateno and L. Glass, “Automatic detection of atrial fibrillation using the coefficient of variation and density histograms of RR and  $\Delta$ RR intervals,” *Med. Biol. Eng. Comput.*, 2001.
- [93] W. Zong, G. B. Moody, and D. Jiang, “A robust open-source algorithm to detect onset and duration of QRS complexes,” *Computing in Cardiology*. 2003.
- [94] I. Processing *et al.*, “Continuous wavelet transform modulus maxima analysis of the electrocardiogram: beat characterisation and beat-to-beat measurement,” vol. 3, no. 1, pp. 19–42, 2005.

- [95] M. Sokolova, N. Japkowicz, and S. Szpakowicz, “Beyond Accuracy, F-Score and ROC: A Family of Discriminant Measures for Performance Evaluation,” Springer, Berlin, Heidelberg, 2006, pp. 1015–1021.
- [96] T. Fawcett, “An introduction to ROC analysis,” *Pattern Recognit. Lett.*, vol. 27, no. 8, pp. 861–874, Jun. 2006.
- [97] G. B. Moody and R. G. Mark, “A New Method For Detecting Atrial Fibrillation Using RR Intervals,” in *Proceedings of Computers in Cardiology*, 1983.
- [98] A. L. Goldberger *et al.*, “PhysioBank, PhysioToolkit, and PhysioNet : Components of a New Research Resource for Complex Physiologic Signals,” *Circulation*, 2000.
- [99] I. Silva and G. B. Moody, “An Open-source Toolbox for Analysing and Processing PhysioNet Databases in MATLAB and Octave,” *J. Open Res. Softw.*, 2014.
- [100] J.-H. Choi and V. Loftness, “Investigation of human body skin temperatures as a bio-signal to indicate overall thermal sensations,” 2012.
- [101] “GATT Overview | Bluetooth Technology Website.” [Online]. Available: <https://www.bluetooth.com/specifications/gatt/generic-attributes-overview>. [Accessed: 26-Jun-2018].
- [102] “Androidplot.” [Online]. Available: <http://androidplot.com/>. [Accessed: 28-Jun-2018].
- [103] AccuWeather, “AccuWeather APIs.” [Online]. Available: <https://developer.accuweather.com/>. [Accessed: 04-Jul-2018].
- [104] Android, “CalendarContract.Instances | Android Developers.” [Online]. Available: <https://developer.android.com/reference/android/provider/CalendarContract.Instances>. [Accessed: 04-Jul-2018].
- [105] “Maximizing BLE Throughput on iOS and Android.” [Online]. Available: <https://punchthrough.com/blog/posts/maximizing-ble-throughput-on-ios-and-android>.
- [106] Alive Technologies, “Alive Bluetooth Heart & Activity Monitor.” [Online]. Available: <https://www.alivetec.com/pages/alive-bluetooth-heart-activity-monitor>.
- [107] F. Miao, Y. Cheng, Y. He, Q. He, and Y. Li, “A Wearable Context-Aware ECG Monitoring System Integrated with Built-in Kinematic Sensors of the Smartphone,” *Sensors*, vol. 15, no. 5, pp. 11465–11484, May 2015.
- [108] A. Tobola *et al.*, “Self-Powered Multiparameter Health Sensor,” *IEEE J. Biomed. Heal. Informatics*, vol. 22, no. 1, pp. 15–22, Jan. 2018.
- [109] M. Caldara *et al.*, “Wearable sensor system for multi-lead ECG measurement,” in *2017 IEEE 14th International Conference on Wearable and Implantable Body Sensor Networks (BSN)*, 2017, pp. 137–140.

- [110] S. P. Preejith, R. Dhinesh, J. Joseph, and M. Sivaprakasam, "Wearable ECG platform for continuous cardiac monitoring," in *2016 38th Annual International Conference of the IEEE Engineering in Medicine and Biology Society (EMBC)*, 2016, pp. 623–626.
- [111] J. Zhang, S.-C. Chan, H. Li, H.-C. Wu, J. Wu, and L. Wang, "A flexible and miniaturized wireless ECG recording system with metal-skin contacts input for wearable personalized healthcare," in *2016 IEEE International Conference on Digital Signal Processing (DSP)*, 2016, pp. 318–321.
- [112] E. Spano, S. Di Pascoli, and G. Iannaccone, "Low-Power Wearable ECG Monitoring System for Multiple-Patient Remote Monitoring," *IEEE Sens. J.*, vol. 16, no. 13, pp. 5452–5462, Jul. 2016.
- [113] "AccuWeather APIs | Weather Icons." [Online]. Available: <https://developer.accuweather.com/weather-icons>. [Accessed: 05-Jul-2018].
- [114] D. Fan, J. Gong, B. Ghaemmaghami, A. Zhang, J. Lach, and D. B. Peden, "Characterizing and Calibrating Low-Cost Wearable Ozone Sensors in Dynamic Environments," in *2017 IEEE/ACM International Conference on Connected Health: Applications, Systems and Engineering Technologies (CHASE)*, 2017, pp. 300–301.
- [115] D. Fan, J. Gong, and J. Lach, "Eating gestures detection by tracking finger motion," in *2016 IEEE Wireless Health (WH)*, 2016, pp. 1–6.